GA–C28668

MODULAR FABRICATION AND CHARACTERIZATION OF COMPLEX SILICON CARBIDE COMPOSITE STRUCTURES

Advanced Reactor Technologies (ART) Research Final Report (Feb 2015 – May 2017)

by
H. Khalifa

Prepared for the U.S. Department of Energy
under Grant No. DE-NE0008323

DISCLAIMER

This report was prepared as an account of work sponsored by an agency of the United States Government. Neither the United States Government nor any agency thereof, nor any of their employees, makes any warranty, express or implied, or assumes any legal liability or responsibility for the accuracy, completeness, or usefulness of any information, apparatus, product, or process disclosed, or represents that its use would not infringe privately owned rights. Reference herein to any specific commercial product, process, or service by trade name, trademark, manufacturer, or otherwise, does not necessarily constitute or imply its endorsement, recommendation, or favoring by the United States Government or any agency thereof. The views and opinions of authors expressed herein do not necessarily state or reflect those of the United States Government or any agency thereof.

GENERAL ATOMICS PROJECT 30438

AUGUST 2017

GENERAL ATOMICS

Contents

DISCLAIMER 0
AUGUST 2017 0
1. Executive Summary 7
2. Summary of Accomplishments 8
3. Project Activities 9
4. Products Developed/Technology Transfer 60
5. Computer Modelling 61
6. Participants and Other Collaborating Organizations 65
References 66
Appendix A – Specimen Fabrication History 67
Appendix B – Large Data Set Composite Flexural Strength 84
Appendix C – Large Data Set Butt Joint Strength 85
Appendix D – ANS 2016 Poster 86
Appendix E – ICACC 2017 Presentation 87
Appendix F – ICACC 2017 Composite Heat Treatment Effects 105
Appendix G – ICACC 2017 Impact Testing 121

List of Figures

Figure 1. Examples of complex SiC-SiC composite basal fuel rod support (a), spacer grid (b), and joined, multi-layered vent manifold (c) structures fabricated during this project. 7
Figure 2. FE simulation in LS-DYNA showing comparable induced damage to experimental impact test of SiC-SiC composite .....
Figure 3. Schematic of EM2 advanced reactor showing core, tri-bundle assembly, and miniature hexagonal fuel bundle assembly with blue denoting target basal fuel rod support structure, green indicating spacer grid structure, and red indicating joined multi-layervent manifold SiC-SiC structures which were design objectives for this project 10
Figure 4.The interphase type and thickness results in different composite microstructures due to reaction of the oxide sintering aids with PyC. SEM images of fibers within different TEP composites show (a) fully reacted PyC interphase and coarsening of fiber stru cture interphase, (b) a thin but well preserved interphase, and (c) a fully preserved PyC interphase resulting from a thick interphase coating. 12
Figure 5.Cross-sectional SEM image of 9 ply, 3 mm thick TEP SiC-SiC composites showing uniform plies distribution and very low void fraction (left). Edge views of TEP SiC-SiC plates made to various thickness (right) .....
Figure 6. Representative flexural stress vs strain curves for SiC-SiC composite fabricated by TEP (blue) and CVI (red) processing methods .....
Figure 7. Four point flexural beam test set-up for 25 x 3 x 1 mm TEP SiC-SiC composite specimen following composite fracture (a), Low magnification cross-sectional SEM image of crack deflection in tested specimen (b), SEM image of fiber pull-out on fracture surface (c) and high magnification SEM image showing fiber and matrix fracture surface (d) .....
Figure 8. Examples of TEP SiC-SiC multihole plates with 10 mm (left) and 20 mm (right) center to center spacing. .....
Figure 9. Examples of monolithic (left) and composite (middle) 7 hole plate TEP plates in as-fabricated state, and following sectioning into hexagonal structure (right) 16
Figure 10. XCT images of basal fuel rod support structure showing (a) 3D volume of entire part, (b) axial plane view at mid height showing different hole arrays and SiC fabric arrangement, and (c) cross sectional plane view including thickness analysis color map 16
Figure 11. Test set-up for DIC instrumented closed hole tension with overall set-up (left) specimen gripping and alignment (upper right), and DIC-produced strain field (lower right) 17
Figure 12. Summary of closed hole tension testing on 4 and 14 mm edge to edge hole spacing composite coupons. Strain is localized, composite behavior is retained, and strength is similar independent of hole spacing. 18
Figure 13. Vickers hardness profiles between adjacent hole features in composiet plates with 4 mm (red) and 14 mm (blue) hole spacing .....
Figure 14. XCT analysis of TEP SiC-SiC curved plate with (a) the complete 3D volume of the part, (b) the cylinder fit to the curved surface via 10,000 point match, and (c) a mid-plane slice of the part taken from a volume created by unrolling the curved part base d on the cylinder fit. The mid-plane slice shows a single fabric ply across the entire plane, which indicates that the ply is parallel to the specimen surface. 19

Figure 15. TEP SiC-SiC composites in various geometries: (a) LWR hexagonal strip, no fillet (b) EM2, no fillet, (c) EM2, 3 mm fillet and (d) 5 EM2 strips with 3 mm fillet arranged but unbonded in hexagonal cellular array configuration 20
Figure 16. Comparison of composite microstructure in (a) a planar composite processed at standard TEP process pressure, and (b) a hexagonal strip composite specimen processed at 20% of standard pressure. 21
Figure 17. Micorhardness data comparing planar composite (orange) and curved "potato chip" composite (blue) specimens. 22
Figure 18. Microhardness data from different regions of a hexagonal strip structures with 3 mm fillet radius. Colors in hardness profiles indicate the three geometric regions identified in the XCT image at right. 22
Figure 19. Schematic of bladder rig test configuration for potato chip specimen .....
Figure 20. Hydraulic bladder flexure test for a planar specimen showing (a) a sample following testing to failure, (b) pressure and strain in the x-direction (c) DIC and AE data, and (d) pressure and strain in the y-direction. 24
Figure 21. Details of bladder testing on curved specimen including FEM of stress distribution in x-direction (a) and y-direction (b), as well as DIC strain map in x-direction (c) and y-direction (d). 25
Figure 22. Drop weight impact test (DWIT) apparatus.....
Figure 23. Impact test results for 3mm thick TEP SiC-SiC showing same specimen after 2cm drop (a), 4cm drop (b), impact energy after 2 cm drop (c) and impact energy after 4 cm drop (d). 28
Figure 24. Images of specimen CS-BD-C-13537-58-1 (a) before test, and (b) after indicating visible damage from repeated drop test including details of hairline crack extension..... 29
Figure 25. Typical impact force and absorbed energy time history plot during a drop weight impact test. The absorbed energy indicates there are energy loss during the impact event 30
Figure 26. Specimen CS-BD-C-13537-58-1 impact force time history and absorbed energy plot during a drop weight impact test. (a) Impact force time history, (b) energy time history, and (c) energy absorbed by specimen. The drop heights are increased from 20 mm to 120 mm with a 20 mm step. Gradually increasing absorbed energy indicates damage accumulation during the repeated impact events. 30
Figure 27. Sample CS-BD-C-13537-58-1 impulse excitation test data after drop weight impact test. The frequency of the first flexural vibration mode and the first torsional vibration mode are plotted against the drop height. The deviation of vibration frequencies indicates a gradually increasing damage induced by repeated impact events..... 31
Figure 28. Sample CS-5H-MM-13537-62-1 pictures (a) before test, and (b)-(d) visible damages after repeated drop test. The specimen cracked after 4 repeated drop tests. In (b) radial cracks formed at the center hole directly under the impact site, both the front and the back layer are cracked in a similar pattern; (c) crack propagation along the fiber direction in the underlying fabric layer; and (d) around one of the outer holes, a smaller crack developed along a consolidation defect. 31
Figure 29. Sample CS-5H-MM-13537-62-1 impact force time history and absorbed energy plot during a drop weight impact test. (a) Impact force time history, (b) energy time history, and (c) energy absorbed by specimen. The drop heights are 20 mm repeated three times, and then a 40 mm drop test. The absorbed energy plot (c) indicates slight increase in absorbed energy following the second impact, and a much more pronounced energy absorption following the 40 mm impact indicative of more widespread induced damage. 32

Figure 30. Sample CS-5H-MM-13537-62-1 Impact force and energy time history plots indicate the damage accumulation, propagation, and the final cracking during a repeated impact events.(a)-(c) are for three repeated 20 mm drop; and (d) is the final 40 mm drop, when large scale cracking was observed.....32
Figure 31. Sample CS-5H-MM-13537-62-1 impulse excitation test data after drop weight impact test. The frequency of the first flexural vibration mode and the first torsional vibration mode are plotted against the drop height. The deviation of vibration frequencies corroborate the gradually increasing damage induced by the repeated impact events. 33
Figure 32 DSC and TGA curves of TEP SiC joint precursor in flowing argon atmosphere.....35
Figure 33 XCT images of selected sandwich joint specimens showing the microstructure of the joint layer 36
Figure 34 SEM images of various TEP joint cross-sections .....
Figure 35 DNS stress-displacement curves for different TEP joints 38
Figure 36 Optical microscope images of notched GA-TEP3-T3-P2 specimen before and after DNS test...38
Figure 37 Average flexure strength of as-fabricated and heat treated TEP SiC composites. Each bar represents the average of 7 to 10 tests. Error bars indicate +/- 1 standard deviation 39
Figure 38 Representative stress extension curves of as fabricated and heat treated TEP SiC-SiC composites 39
Figure 39 Fracture surface SEM images of as fabricated and heat treated TEP SiC-SiC composites 40
Figure 40 Microstructure of TEP3 joints with one-step and two-step sintering profiles 41
Figure 41 . Back scattered SEM images of two joints with different thickness and its effects on crack propagation into the substrate 42
Figure 42 Optical microscopy images of specimens following DNS test, showing the fracture pattern. The green arrow indicates the shear direction 43
Figure 43 SEM and low magnification TEM image of specimen 13424-80. The entire field of view in the TEM image is joint material.....44
Figure 44 TEM images and selected area diffraction patterns (d and e) of specimen 13424-80. The colored boxes in (1) and (2) indicate the regions where higher magnification images and SAED were taken. 45
Figure 45 Back-scattered electron SEM images of joint 13453-23 and 27.....45
Figure 46 TEM images and SAED patterns of specimen 13453-27. Green arrows indicate joint interface, blue arrows indicate pores, and colored boxes indicate areas of interest SAED and high magnification images. 46
Figure 47 (a): Schematic of the hermeticity test rig and (b): a photograph of a joint specimen mounted on a metal flange.....47
Figure 48 SEM images showing microstructure of hermeticity samples 47
Figure 49 Optical microscopy images shown specimen 13453-42L before (1), and after (2) DNS test. Green arrow indicates the shear direction. 49
Figure 50 Optical microscopy images shown specimen 13453-47L before (1); and after (2), (3) DNS test. Green arrow indicates the shear direction 49
Figure 51 Optical microscopy images shown specimen from 13453-56L before (1), and after (2) DNS test. Green arrow indicates the shear direction and the black errors indicate the main failure crack.....50
Figure 52 Optical microscopy images showing specimen from 13453-59L: (1) before test, and (2), the two fracture surfaces. Green arrow indicates the shear direction 50

Figure 53. Image of joined multi-layer SiC-SiC composite vent manifold structure (a), Semi-transparent X-ray computed tomography (XCT) volume of the multi-layer vent manifold assembly showing internal channel network (b), with XCT slices of the middle layer of pie-shaped composite pieces that define the asterisk-shaped vent channels (c), cross sectional view indicated line I showing 4 coolant channels and the central fission gas channel in that plane (d), cross-sectional view indicated by line II, showing 3 fuel rod insertion points interconnected by fission gas channel (e), and rendering of miniature EM^2 hexagonal fuel bundle assembly showing vent manifold positioning in red (f). 52
Figure 54. XCT slices showing the cross section of the different edge-to-edge joint geometries. Butt (a) and corrugated (b) joints show well mated interfaces, while tongue and groove (c) shows large regions along the interface where no joint material is present (black). 53
Figure 55. Summary of average joint strength for different joint geometries and process variations. Error bars are +/- one standard deviation. 53
Figure 56. Optical microscopy shows tongue and groove specimen cross section (a), and side view (b) following flexural testing. 54
Figure 57. Optical micrograph comparing fracture surfaces following flexural testing of single and dual step sintered joints. The dual step sintering results in more uniform reaction across the joint, which results in high bond strengths. .....
Figure 58. Weibull plot for flexural strength of CVD SiC butt joints. 55
Figure 59. Optical micrograph of fracture in specimen BJ-LS-2 showing significant substrate fracture along entire surface. 56
Figure 60. Low magnification image of fracture surface in TEP composite butt joint specimen (a), and high magnification image showing smooth, unreacted gray regions of matrix, adjacent to white, oxide rich regions where joint material has accumulated within fibrous regions. 57
Figure 61. X-ray computed tomography (XCT) volume of edge-joined, multi-component vent manifold assembly, GA-JMCCS-D4 (a), with semi-transparent XCT volume showing internal vent channel structure (b), cross-sectional view indicated by line I showing two fuel rod insertion points interconnected by the fission gas channel (c), cross-sectional view indicated by line II, showing four coolant channels and two central fission gas channels (d), and 2-D XCT slice showing alignment of the four components and defect free join seam (e) .....
Figure 62. Schematic representation of how the components successfully produced as part of this project can be deployed to produce a miniature EM^2 tri-bundle assembly. 60
Figure 63. Results of TEP consolidation FEM. Temperature (left) and hoop stress (right) maps of a monolithic TEP disk with 2 holes at end of high temperature processing. 62
Figure 64. Calculated FEM results of hexagonal strip consolidation showing von Mises stresses (a) and resultant pressure on the specimen surface (b) for top and bottom faces of specimen.....63
Figure 65 FE simulation of the radial damage from a 40 mm drop test. LS-DYNA MAT110 material and solid element are used to build the disk. In (a) 0, 45, and 90 degree radial cracks are predicted by the model, which are similar to the cracks observed in the experiment, as shown in (c) the impact surface and (d) the free surface of the disk after burst test......63
Figure 66.Impact force and energy simulation result of a 20 mm drop test from the FE model (a) the contact force and (b) the kinetic energy of the impactor are similar to the experimental result shown in (c). The shoulder in the force plot is associated with the damage developed in the specimen. 64

Figure 67 Layered shell element is implemented to model a 5-layer TEP-SiC composite. The disk sample is constructed by 5 layers of shell elements, different materials and thickness can be applied to individual layers. 65

List of Tables

Table 1. Measured values of various composite specimens evaluated by flexural beam testing..... 14
Table 2 Process conditions and mechanical properties of various TEP based and GA-HSiC joints 40
Table 3 Summary of DNS test shear strength for TEP3 joints processed at 1600°C, 30MPa 43
Table 4 List of joints chosen for TEM work 43
Table 5 Helium leak rate of various joints under a pressure difference of 24.7 psi 47
Table 6 List of large joint specimen process parameters and shear strength where oxide content in TEP2<TEP3<TEP4, and process pressure P1<P3<P5<50 MPa. “L” in ID indicates large plate specimen, “S” indicates small specimen. Four tests specimens were prepared from each “L” sample, while only a single test specimen was prepared form each “S” specimen..... 48

1. Executive Summary

Advanced ceramic materials exhibit properties that enable safety and fuel cycle efficiency improvements in advanced nuclear reactors. In order to fully exploit these desirable properties, new processing techniques are required to produce the complex geometries inherent to nuclear fuel assemblies and support structures. For example, General Atomics (GA) is actively developing silicon carbide (SiC) fiber reinforced, silicon carbide matrix (SiC-SiC) composites in support of its Energy Multiplier Module (EM^2) gas-cooled fast reactor. The high coolant temperature and long fuel cycle in EM^2 and other advanced high temperature gas, molten salt and liquid metal reactors necessitate the use of SiC-SiC composite for all structural materials within the core. Through DOE funding via the Advanced Reactor Technologies (ART) program, GA successfully demonstrated the fabrication of SiC-SiC composite components containing complex features required for utilization of these materials for in-core support structures such as the fuel rod support, spacer grid, and gas vent manifold structures shown in Figure 1. Fabrication of these complex structures included processing demonstrations in bulk composite densification, thru-hole and blind-hole features, varying radius of curvature in non-planar structures, and joining of composite substructures to create larger more complex assemblies.

Figure 1. Examples of complex SiC-SiC composite basal fuel rod support (a), spacer grid (b), and joined, multi-layered vent manifold (c) structures fabricated during this project.

In addition to first of a kind complex SiC-SiC composite structure fabrication, comprehensive characterization gleaned a deeper understanding of the relationship between incorporation of complex features and composite performance. Several key outcomes came from this characterization effort. The lower limit in thru-hole feature spacing while retaining bulk composite properties was determined to be 2.6 mm. This limit has implications on potential core loading efficiency if SiC-SiC composite is used as a fuel rod support structure. Finite element modeling was used to leverage experimental test data into a predictive tool for dynamic mechanical response in complex SiC-SiC composite structures (Figure 2). A non-destructive examination technique called impulse excitation (IE) was implemented to detect micro-scale damage in ceramic matrix composite structures. This NDE tool can be used to assess composite while in operation. The enhanced fabrication capability and performance data acquired have substantially advanced the case for implementation of SiC as a reactor core material.

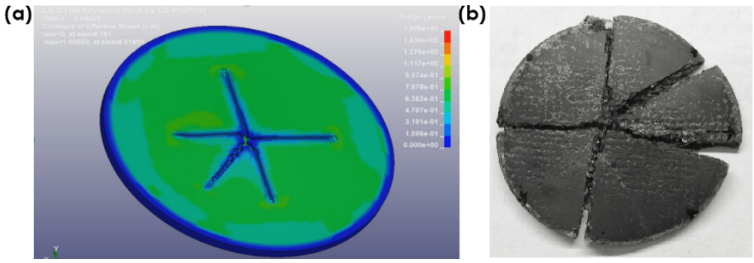

Figure 2. FE simulation in LS-DYNA showing comparable induced damage to experimental impact test of SiC-SiC composite

2. Summary of Accomplishments

For each of the project objectives listed below, a summary of the qualitative and quantitative results are provided.

1.) Fabrication of Planar SiC-SiC Composite Substructures

- Determined that transient eutectic phase (TEP) processing is the preferred composite fabrication route for complex structures due to high proportional limit strength, faster process time, larger critical thickness capability, and near net shape capability compared with CVI. In excess of 50 mechanical tests were performed to arrive at this conclusion
- Modeled heat transfer during composite consolidation in COMSOL and associated development of microstructural features in fabricated parts with conductive heat loss from sample to graphite tooling
- Determined that reduction in thru-hole spacing from 14 to 4 mm did not adversely impact composite strength, strain to failure or composite response using the closed hole tension test
- Determined that hole feature spacing was dictated by fiber architecture and limited to no smaller than 2.6 mm
- Fabricated 100 mm planar structures with 19 thru hole features of varying diameters with spacing as small as 3 mm while maintaining greater than 95% theoretical density and good composite microstructure
- Fabricated 100 mm planar structures with blind holes for fuel rod support and thru holes for coolant flow with no adverse effects on local hardness, density or microstructural variation.

2.) Fabrication of Non-planar SiC-SiC Composite Substructures

- Fabricated curved composite disks while maintaining same density and microstructure as planar composite
- Developed hydrostatic bladder test for mechanical testing of curved structures
- Fabricated hexagonal composite arrays as base unit of spacer grid structure
- Constructed heat transfer model in COMSOL to show how stress distribution is affect by fillet radius in hexagonal composite structure and determined that fillet radius of curvature greater than 3 mm is necessary to achieve uniform microstructure and hardness across geometric transition
- Conducted instrumented impact tests including repeated impact of the same specimen and observed no detectable damage by impulse excitation technique until after 4th impact of 3 kg indenter from 2 cm drop height
- Measured residual strength of composite specimens following impact testing using bladder test and showed 90+% strength was retained following impact at velocities relevant to LWR handling requirements
- Modelled anisotropic composite response in LS-DYNA and accurately reproduced fracture behavior force and energy of impact through representative simulation of composite damage accumulation during impact test

3.) Fabrication of Multi-layer SiC-SiC Composite Sub-Components by Modular Joining

- Determined that increased oxide content in TEP joints promotes good joint integrity at lower process temperature and pressure by depressing the liquid phase temperature of

the melt. Process pressures as low as 3 MPa enables joining of thinner delicate structures to create added complexity

- Conducted more than 30 double notch shear tests on various TEP joined CVD SiC blocks to establish TEP joint strengths greater than 125 MPa are attainable with high oxide content formula and joint thickness of less than 50 µm. Joint microstructure can be improved using multi-step binder burnout processing
- Performed scanning and transmission electron microscopy on TEP joints to show that strength is derived from high degree of chemical reaction and low differential coefficient of thermal expansion across interface
- Determined that joint processing above 1700°C results in nearly complete strength loss of composite substrate, while joint processing at 1600°C results in 90% strength retention, therefore joint processing at or below 1600°C is necessary to preserve composite performance
- Demonstrated permeability of TEP joint less than 1E-9 atm*cc/sec can be achieved
- Performed IE on as-fabricated and impact tested specimens and determined that acoustic signatures for induced damage were most clearly conveyed by changes in torsional frequency
- Fabricated 3 layer, 8-piece, 4-inch diameter TEP SiC-SiC composite multilayer vent manifold assembly featuring distinct, hermetic fluid flow pathways in-plane as well as thru-thickness.

4.) Fabrication of SiC-SiC Composite Assemblies through Mechanically-enhanced Joining

- Established geometric scheme for joining multiple multi-layer joined structures with mechanically enhanced joints to create larger complex structures while preserving feature spacing across joint interfaces
- Conducted flexural beam testing on set of 20 mechanically enhanced joints produced with butt-, corrugated-, and tongue and groove-type geometries and determined that butt joint gave highest average strength and smallest scatter. Alignment issues associated with the more complex alternatives led to poor interfacial contact and low strength
- Conducted flexural beam testing a 15 specimen set of butt joint
- Produced a 4 component multi-layer vent manifold assembly demonstrating the scalability of complex structure fabrication by way of edge-to-edge joining of SiC-SiC composite subassemblies

3. Project Activities

3.1 Background

The development of ceramic matrix composite (CMC) technology is an important area of enabling research and development (R&D) for advanced nuclear reactors. Silicon carbide (SiC) fiber-reinforced SiC matrix CMCs (SiC-SiC) are a particularly attractive materials for fuel cladding and core support structures in advanced reactor concepts such as General Atomics' gas-cooled fast reactor (EM^2), liquid metal reactors, and advanced molten salt reactors. SiC-SiC is also being looked at for use as accident tolerant fuel in current generation light water reactors (LWR). The capability to produce large complex SiC-SiC composite structures while maintaining the appealing properties of the base composite material is essential to the use of SiC-SiC for this purpose, and General Atomics

(GA) and others are currently developing the requisite composite fabrication technology. While significant progress has been made in qualifying the irradiation performance of SiC and SiC-SiC composite, and the DOE's program has promoted significant research in the utilization of SiC-SiC composite as a thin walled cladding material, little work has been done to examine the feasibility of producing SiC-SiC composite in the complex geometries necessary for deployment of this material as an in-core structural material. The dearth of research into processing methods for complex structure fabrication, and lack of associated data establishing structure property relationships in complex SiC-SiC composite assemblies is an impediment to the development, licensing and implementation of SiC-SiC composite in the nuclear industry.

DOE funded GA under the ART program (DE-NE0008323) to address this critical need and what follows is a final report on the work performed. During the period of performance composite fabrication by transient eutectic phase (TEP) processing, a form of liquid phase sintering, was used to demonstrate fabrication of a variety of increasingly complex SiC-SiC composite structures aimed specifically at addressing geometries useful to the nuclear reactor industry. TEP processing provides rapid, near-net shape composite fabrication to large thicknesses that make it ideally suited for the more robust structural components required for fuel rod support structures. Further, the TEP fabrication route has demonstrated strength and microstructural stability under neutron irradiation [1]. All composites produced in this work were reinforced with high purity SiC fiber. The work progressed in stages to address varying complex structures anticipated in an advanced reactor core using EM^2 to guide likely structures and function. The simplified fuel bundle assembly shown in Figure 3 highlights the critical design challenges addressed through fabrication and comprehensive testing in this work. Near-net shape processing was implemented to produce planar structures with blind and thru hole features. These planar structures serve as basal fuel rod support structures or substructures for more complex assemblies. Non-planar structures were produced to serve as a building unit for a spacer grid assembly. Joining techniques were implemented to bond planar substructures to produce multi-layer complex assemblies. Lastly, joining was leveraged again to produce larger assemblies by joining multiple multi-layer assembles edge-to-edge similar to the EM^2 tri-bundle assembly configuration.

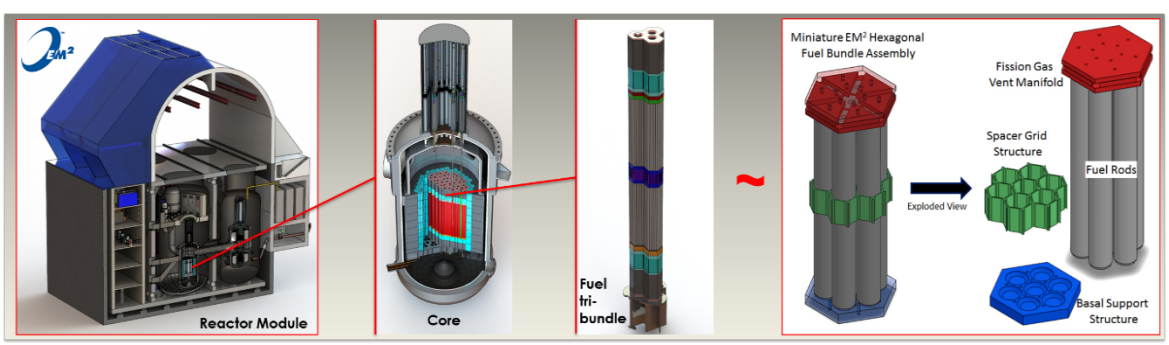

Figure 3. Schematic of EM2 advanced reactor showing core, tri-bundle assembly, and miniature hexagonal fuel bundle assembly with blue denoting target basal fuel rod support structure, green indicating spacer grid structure, and red indicating joined multi-layervent manifold SiC-SiC structures which were design objectives for this project

For each of the composite structures produced, comprehensive microstructural and mechanical testing was conducted to provide a better understanding of the effect of part complexity on SiC-SiC composite performance. This data established limits on part complexity such as feature size and

spacing which will ultimately inform fuel loading and efficiency of advanced reactor designs utilizing SiC-SiC composite.

Through this project, the state of complex SiC-SiC composite fabrication for nuclear components has advanced significantly. New methods to produce complex SiC-SiC composite structures have been demonstrated in the form factors needed for in-core structural components in advanced high temperature nuclear reactors. Advanced characterization techniques have been employed to demonstrate that these complex SiC-SiC composite structures provide the strength, toughness and hermeticity required for service in harsh reactor conditions. The complex structures produced in this project represent a significant step forward in leveraging the excellent high temperature strength, resistance to neutron induced damage, and low neutron cross section of silicon carbide in nuclear applications.

3.2 Fabrication of Planar SiC-SiC Composite Substructures

In this task, planar SiC-SiC composite structures with internal features such as thru-holes were fabricated and evaluated. Emphasis was placed on maintaining uniform microstructure throughout each part, particularly in close proximity to an internal feature. Microstructural variations are an indicator of abnormal processing conditions that can degrade performance. Through microstructural characterization, bulk mechanical testing, and microhardness testing, structure-property relationships were determined as a function of part complexity, and limits were established for how close together internal features could reliably be processed without adversely affecting performance.

3.2.1 Composite Fabrication

An evaluation of the different composite processing techniques was conducted on basic planar composite structures prior to transitioning to the challenges of fabrication with complex features. CVI and TEP composites were compared in terms of their mechanical properties, and applicability to the end use of producing robust structures necessary for use as core support structures.

3.2.1.1 Interphase coating

In order to achieve composite behavior in SiC-SiC composites, the fibers must have an interphase coating. For nuclear applications, this interphase is typically pyrolytic carbon (PyC). Under an applied load, this interphase layer gives rise to the fiber sliding that defines “graceful” failure in composite materials. Whether the composite is consolidated by TEP or CVI, the interphase coating is achieved by chemical vapor deposition. For CVI composites, this interphase coating is typically 100-500nm. However, the oxides in TEP powder precursors react with the PyC, and for thinner interphase coatings, the reaction totally consumes the interphase layer and can alter the microstructure of the fibers. The consumption or elimination of this interphase layer results in brittle behavior more typical of a fully monolithic material because the fibers can no longer slide in the matrix [2]. To combat this reaction, GA has been evaluating alternative interphase coatings interphase that ensure some residual PyC even if oxide reaction occurs, such that composite like behavior can still be achieved. Example cross sections of TEP composites with some of these different interphases are shown in Figure 4.

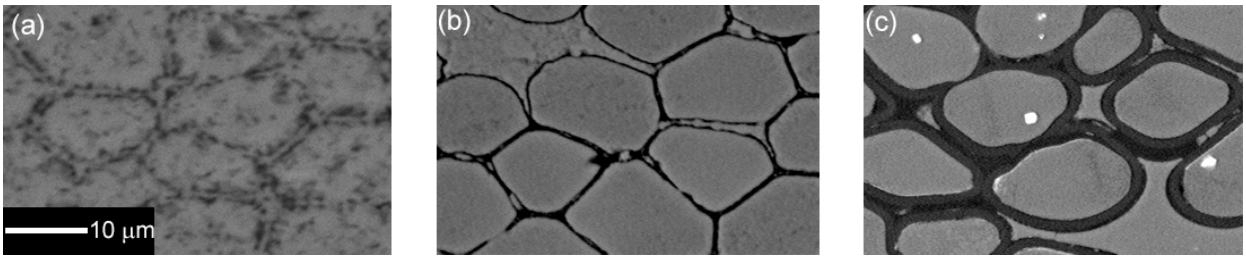

Figure 4.The interphase type and thickness results in different composite microstructures due to reaction of the oxide sintering aids with PyC. SEM images of fibers within different TEP composites show (a) fully reacted PyC interphase and coarsening of fiber structure interphase, (b) a thin but well preserved interphase, and (c) a fully preserved PyC interphase resulting from a thick interphase coating.

3.2.1.2 TEP vs CVI Composites

Transient eutectic phase (TEP) composite plates were fabricated for the purposes of mechanical and microstructural evaluation. Composites were initially made using the Tyranno ZMI fabric, which allowed for evaluation of densification efficiency, but for representative strength measurements, the higher purity, stoichiometric Tyranno SA3 fabric was used because the ZMI fiber degrades upon exposure to the 1800°C process temperature during TEP densification, which leads to weakened fibers and poor overall composite strength. TEP composites were fabricated in thicknesses ranging from 0.5 to 3 mm with a fiber volume fraction of approximately 45%. Examples of composite disks are shown in **Error! Reference ource not found.**, with an SEM cross-section of a 9 ply 3 mm thick composite part. Note that with TEP processing, larger thicknesses can be achieved while maintaining extremely low porosity and greater than 90% relative density. CVI composites were fabricated to nominal thicknesses of 0.5, 1.3 and 2.7 mm, which had relative densities of 85, 84 and 74%. The 0.5 mm and 1 mm composite panels were fabricated with 0-90 plain weave fabric, while the 2.7 mm panel was fabricated with 4 harness satin weave fabric. Increasing thickness did not affect composite density with TEP processing, whereas with CVI, increased part thickness resulted in decreased density, increased infiltration time, and also increases the likelihood of void

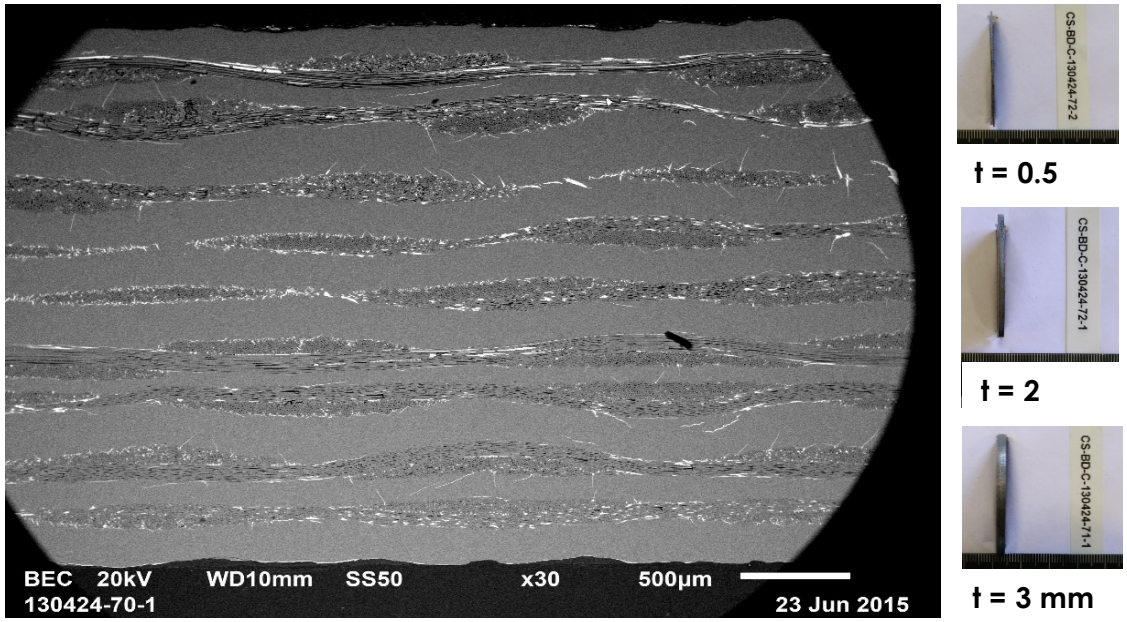

Figure 5.Cross-sectional SEM image of 9 ply, 3 mm thick TEP SiC-SiC composites showing uniform plies distribution and very low void fraction (left). Edge views of TEP SiC-SiC plates made to various thickness (right)

formation. In addition to density, the effect of composite thickness and fiber volume fraction was also evaluated by mechanical 4 point flexure testing.

3.2.2 Mechanical Performance of Base SiC-SiC Composite Material

Flexural beams specimens were sectioned from plates of TEP and CVI composite material. The selection of these specimen dimensions and fixture spans were made in accordance with ASTM 1341, "Standard Test Method for Flexural Properties of Continuous Fiber-reinforced Advanced Ceramic Composites." For each sample set, 10-20 specimens were tested.

Composite behavior is characterized by "pseudo-ductile" fracture behavior. This type of failure can be described as a departure from linear elastic behavior as matrix cracking occurs and load is transferred from the matrix to the fibers. As loading continues fibers begin to move within the matrix and final composite failure results when significant fiber breakage catalyzes larger scale cracking through the bulk material. Both CVI and TEP composite materials exhibited composite-like fracture, however, the different microstructural features of the two composite types gave rise to some notable differences in the stress-strain behavior. TEP composites exhibit significantly higher proportional limit stress (PLS) and elastic modulus. CVI composites exhibit more strain prior to the ultimate flexural stress (UFS). However, after reaching the UFS, the TEP composites show a more gradual degradation in strength indicated by several load drops. In both cases, the UFS and total strain to failure are comparable. Representative stress-strain curves for TEP and CVI composites are shown in Figure 6. As cracking progresses during composite testing, the propagating crack takes a circuitous route through the composite layers. The crack will often travel along a fabric ply interface before turning and meandering through a tow of fibers. As the crack propagates through the fabric layer, individual fibers will slide out of the matrix prior to individual fiber breakage. All of these processes are energy consuming phenomena that define composite behavior. Examples of these phenomena are shown in Figure 7**Error! Reference source not found.**.

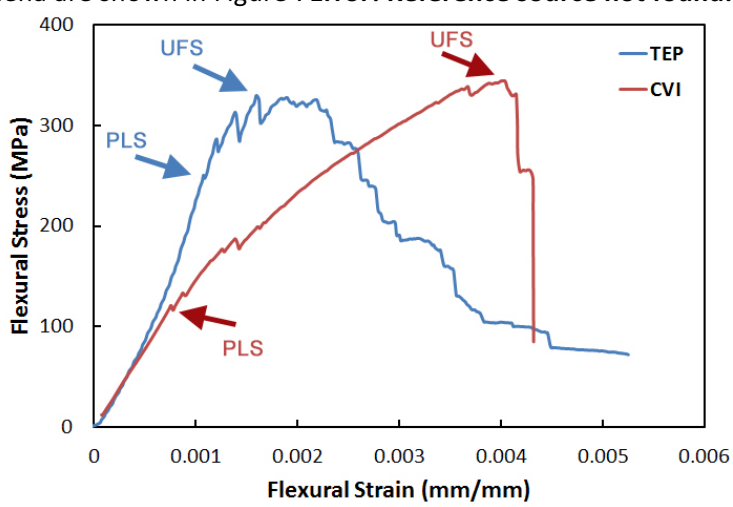

Figure 6. Representative flexural stress vs strain curves for SiC-SiC composite fabricated by TEP (blue) and CVI (red) processing methods

Table 1. Measured values of various composite specimens evaluated by flexural beam testing.

Fabrication type	ρ_{rel} (%)	t_{avg} (mm)	PLS (MPa)	UFS (MPa)	E (GPa)	m_{PLS}	m_{UFS}	m_E
TEP - 2 ply	88	0.57	189	321	354	5.3	6.4	5.9
TEP - 3 ply	89	0.97	213	306	343	6.2	7.0	3.5
TEP - 6 ply	90	2.06	194	303	331	5.4	6.3	5.1
CVI -2 ply	85	0.51	122	318	255	4.1	4.4	4.0
CVI - 4 ply	84	1.36	113	324	234	3.8	4.3	3.9
CVI - 8 ply*	74	2.67	125	410	226	4.1	6.2	3.6

* thick CVI specimen was fabricated with different fiber architecture (Satin than plain weave)

The results for the different thicknesses of CVI and TEP composites are presented in Table 1. Within the thickness range evaluated, no degradation in strength or elastic modulus was observed for either CVI or TEP composites. The TEP composite density was insensitive to overall composite thickness, while the CVI material showed decreased density as part thickness increased. This density degradation did not have a significant effect on the mechanical performance. It should be noted however, that the thickest CVI sample set was made using different fiber architecture. The use of satin weave can explain the higher UFS observed for the 8 ply sample. The fiber architecture would not affect the linear elastic behavior of the composite so both the elastic modulus and PLS may be compared to the thinner samples with a high level of confidence. Within this context, the 8 ply CVI composite performed similarly to the thinner CVI samples with regard to PLS, UFS, and E.

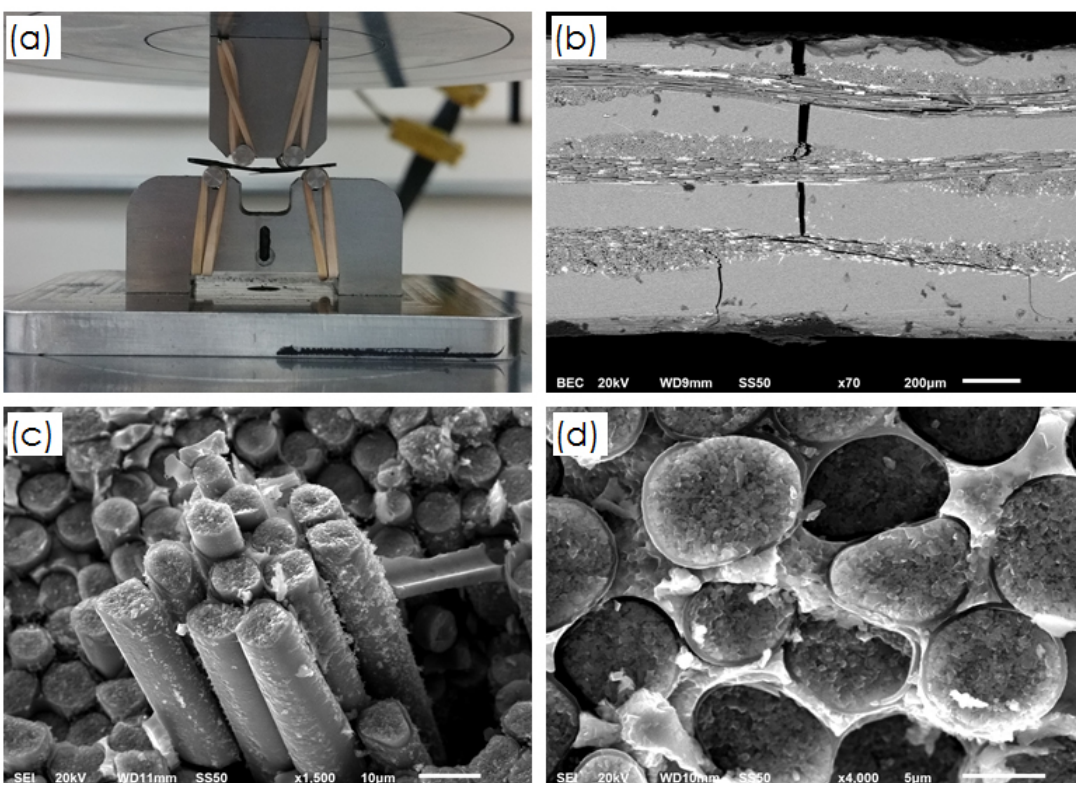

Figure 7. Four point flexural beam test set-up for 25 x 3 x 1 mm TEP SiC-SiC composite specimen following composite fracture (a), Low magnification cross-sectional SEM image of crack deflection in tested specimen (b), SEM image of fiber pull-out on fracture surface (c) and high magnification SEM image showing fiber and matrix fracture surface (d)

Each sample set was assessed via Weibull analysis. The Weibull modulus is a parameter that describes the reliability of the property being analyzed. A high Weibull modulus indicates a more reliable material. Weibull analysis was applied to the PLS, UFS, and E of each sample set. In general the Weibull values are in good agreement with ceramic matrix composite materials. Within this study, the TEP composites exhibit slightly higher Weibull modulus for PLS and UFS, while the elastic modulus Weibull value is similar between CVI and TEP composite material. TEP composite material is more appealing for future complex structure work owing to this improved Weibull performance.

The most significant conclusions to be drawn from these data are the enhanced PLS strength and elastic modulus in the TEP composite material. The TEP composite exhibited a PLS at least 55% greater than the CVI composite at each thickness. The elastic modulus was also at least 44% greater than the CVI at each thickness. The PLS indicates the progression of matrix cracking. Although the CVI material continues to strengthen beyond this point, the PLS is considered as a likely design parameter since hermeticity will be lost at this point. The substantially higher PLS values for TEP composite processing make it the preferred route for fabrication of complex structures for the target application.

3.2.3 Planar Fabrication with Thru holes

Special graphite tooling was designed and fabricated for systematic evaluation of thru-hole spacing feasibility. Composite plates, were fabricated with two different center-to-center hole spacings – 10 mm and 20 mm, corresponding to edge-to edge spacing of 4 mm and 14 mm between adjacent holes. The transition to complex plates with thru hole features did not impact the bulk density of the parts being fabricated. Typical 2 hole plates have relative densities from 86-91%. Examples of the two different plate types geometries are shown in Figure 8. The objective in fabricating the two hole plates with these two different spacings was to evaluate whether smaller spacing led to interaction of these affected zones as hole spacing decreased. Initial mechanical testing of closed hole tension specimens sectioned from these 2 hole plates is described in section 3.2.4 below.

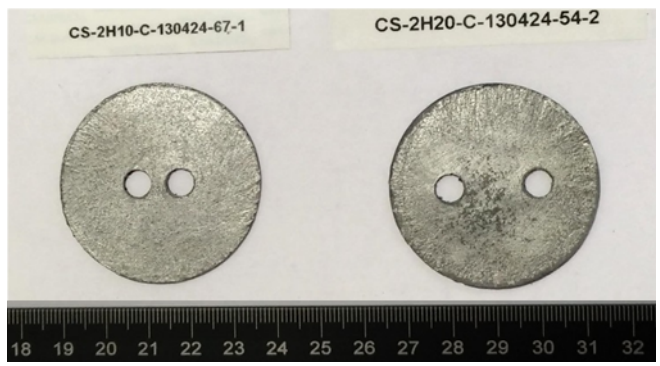

Figure 8. Examples of TEP SiC-SiC multihole plates with 10 mm (left) and 20 mm (right) center to center spacing.

The same graphite tooling design methodology was used to successfully fabricate a plate with a hexagonal 7 hole array. The smaller 10 mm center-to-center spacing was used for fabricating these structures. XCT data of monolithic SiC and composite versions of this hexagonal array plate are shown in Figure 9. From these volumes, it is apparent that discolored zones near the holes in the monolithic SiC plate intersect with one another, potentially affecting overall performance. However, when fiber reinforcement is introduced, the improved stress distribution and in plane heat transfer offered by the continuous fibers eliminates the affected zones surrounding the hole features and specimen edge.

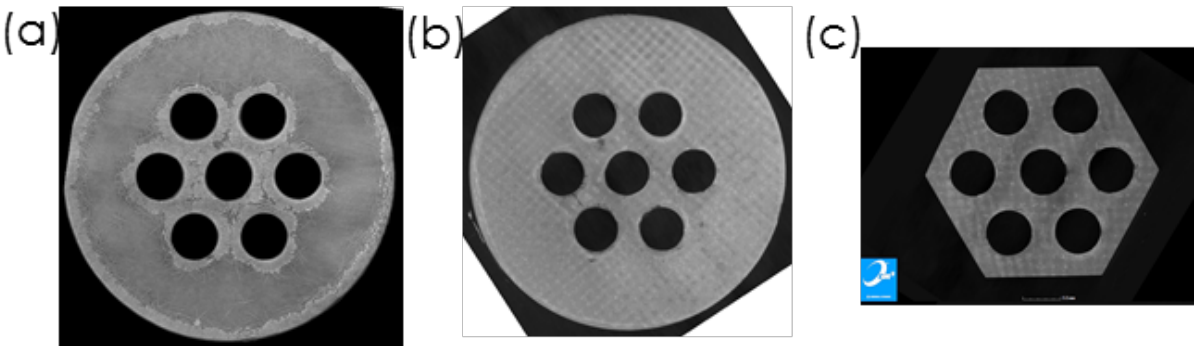

Figure 9. Examples of monolithic (left) and composite (middle) 7 hole plate TEP plates in as-fabricated state, and following sectioning into hexagonal structure (right)

The scalability of this fabrication route was demonstrated with a 101.6 mm diameter basal fuel rod support structure. Through TEP processing, composite structures with blind hole features or reservoirs, each designed to receive a single fuel rod 21 mm in diameter, arranged in a hexagonal pattern of 7 holes have successfully been processed. The scaled example of a basal support structure is 5 mm thick. The size of these parts can be easily scaled up with appropriate equipment. This is not intended to be a final design, but a representation of how such a component may be fabricated. It should be understood that additional design inputs for specific reactor applications will dictate the final design features to optimize fuel loading, coolant pressure drop, etc. In this example, each fuel rod reservoir is 3 mm deep with a 3 mm fillet radius to help center and align the fuel rod during insertion. In addition, the components feature 12 thru-holes each 3 mm in diameter designed to allow coolant flow between each rod. During preforming of the composites, care was taken to ensure minimal deflection of each fabric ply, as this presents potential for fiber or interphase damage. The microstructure of these composite specimens was not appreciably different than planar parts fabricated earlier in the project. The composite parts have a 95% relative density and 40% fiber volume fraction. This result is notable because it demonstrates retention of part density while also, for the first time, showing the ability to fabricate recessed, curved features and thru-hole features in a single, near-net shape part. Figure 10 contains XCT volume, axial and cross sectional views to show both thickness uniformity and the arrangement of fabric plies in the part following consolidation. The thickness analysis in Figure 3(c) shows constant thickness of 5.5 mm away from features. Below the blind hole there is approximately 2 mm of composite material. One of these scaled example basal support structures has been sent to DOE to fulfill the second physical deliverable of this project.

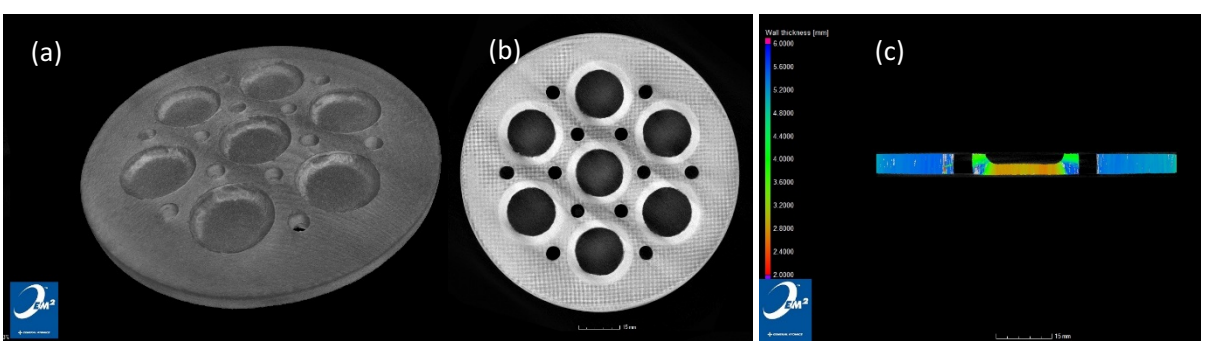

Figure 10. XCT images of basal fuel rod support structure showing (a) 3D volume of entire part, (b) axial plane view at mid height showing different hole arrays and SiC fabric arrangement, and (c) cross sectional plane view including thickness analysis color map

3.2.4 *Mechanical Testing of Complex Planar Structures*

The bulk and microscale mechanical response are important indicators of quality consolidation and retention of composite behavior which are necessary for demonstrating the reliability of these composite structures for the target application.

3.2.4.1 *Closed Hole Tension Testing*

Tension testing instrumented with digital image correlation (DIC) has been set up and implemented for full field strain visualization of TEP SiC-SiC composites specimens containing thru-hole features. Specimens sectioned from 10 and 20 mm spacing 2 hole plates were tested. The test configuration is shown in Figure 11. The critical issue involved with testing of these specimens were proper gripping and alignment to prevent unexpected damage or bending during testing. A ball joint fixture prevents off axis loading of the specimen throughout the test, while aluminum tabs epoxied onto the SiC-SiC coupon allow reliable, damage-free gripping.

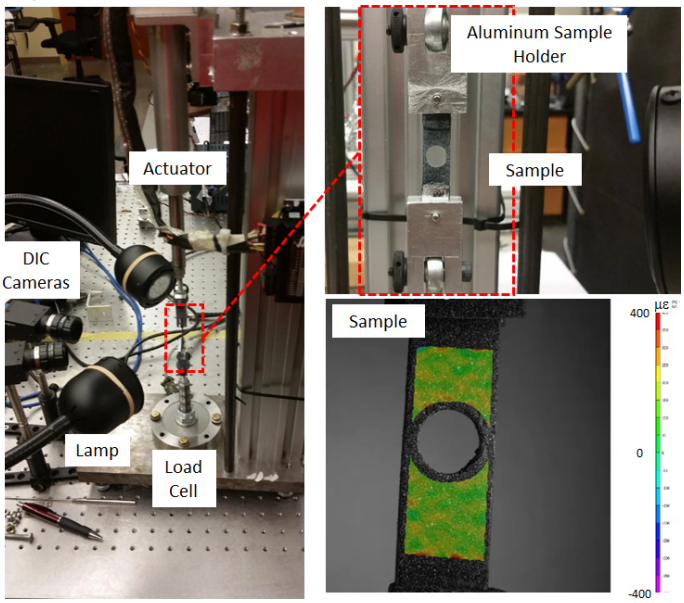

Figure 11. Test set-up for DIC instrumented closed hole tension with overall set-up (left) specimen gripping and alignment (upper right), and DIC-produced strain field (lower right)

The results of the closed hole tension test are summarized in Figure 12. The strain is localized around the thru-hole feature, and the strength and strain values are nearly identical irrespective of hole spacing. Furthermore, traditional fracture mechanics predicts a 2.19σ stress concentration resulting from a hole in a finite plate. The composite strength is therefore approximately 225 MPa or similar to the values in Table 1. This data strongly indicates that spacing between hole features is not a limiting factor in terms of deformation behavior. The artifacts observed in Figure 9 do not appear to impact composite response. Edge to edge hole spacing as low as 4 mm was experimentally shown to retain similar composite behavior to the bulk composite and the fiber weave unit cell of 2.6 mm for Tyranno SA3 is likely the lower limit for feature spacing based on all analyses performed on these complex planar structures

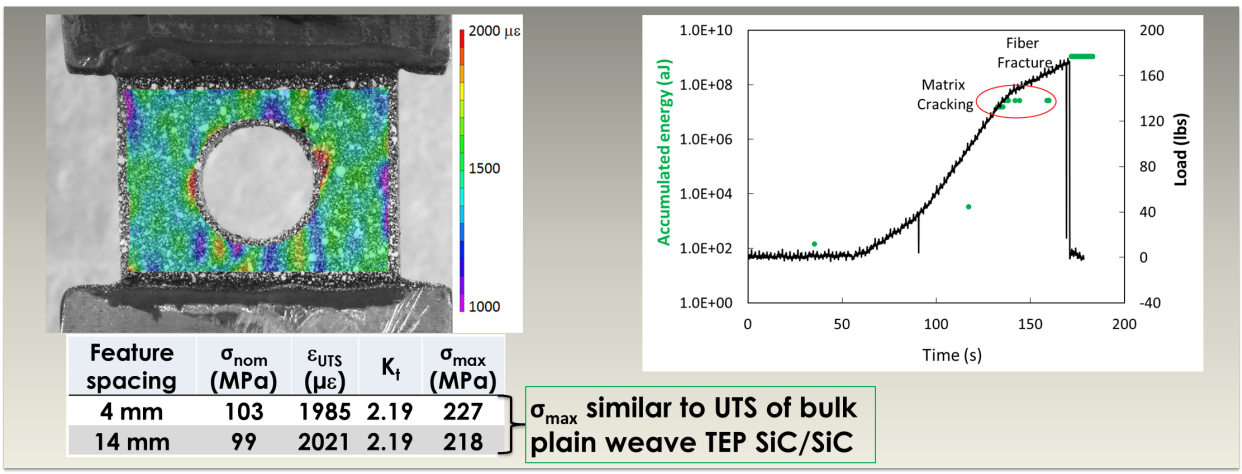

Feature spacing	σ_{nom} (MPa)	ε_{UTS} (με)	K_t	σ_{max} (MPa)
4 mm	103	1985	2.19	227
14 mm	99	2021	2.19	218

Figure 12. Summary of closed hole tension testing on 4 and 14 mm edge to edge hole spacing composite coupons. Strain is localized, composite behavior is retained, and strength is similar independent of hole spacing.

3.2.4.2 Microhardness Testing

Vickers microhardness was conducted for examination of both surface properties as well as bulk properties following sectioning of composite specimens. The hardness was measured within the matrix material as well as on individual fibers. These hardness values were compared across multiple specimens as a function of processing as well as within single specimens as a function of position from thru-hole features.

Hardness measurements conducted between adjacent hole features did not reveal significant trends in spatially derived property variation. Hardness was relatively constant near the edge of hole features as well as equidistant between adjacent hole features. A profile of hardness measured every 2 mm in a plate with holes centered 20 mm (14 mm edge to edge) as well as 10 mm (4 mm edge to edge) apart is shown in Figure 13. Furthermore, the hardness did not change significantly as the spacing between holes decreased 14mm vs 4 mm edge-to-edge hole spacing). In fact, the average Vickers hardness was slightly lower (1568 HV) in the 14 mm edge to edge spacing specimen, than it was in the 4 mm edge-to edge spacing specimen (1616 HV). This data taken together with the closed hole tension data (section 3.2.4.1) and heat transfer modeling (section 5.1) show the link between processing, structure and performance.

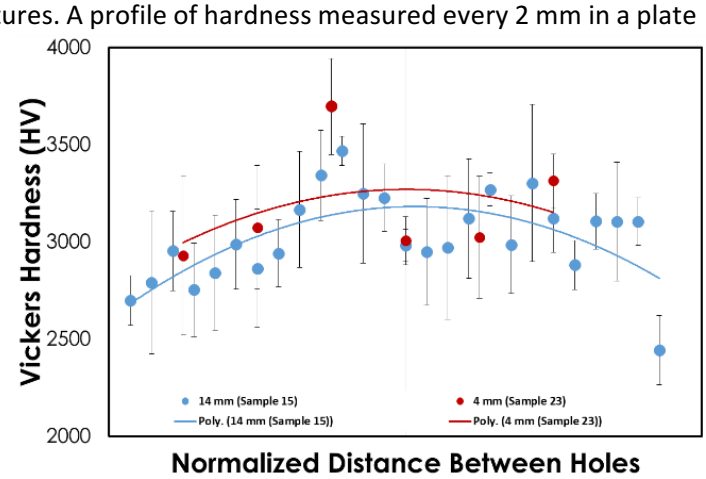

Figure 13. Vickers hardness profiles between adjacent hole features in composiet plates with 4 mm (red) and 14 mm (blue) hole spacing

3.3 Fabrication of Non-planar SiC-SiC Composite Substructures

In this task, non-planar SiC-SiC composite structures were fabricated by the TEP process and evaluated. Emphasis was placed on maintaining uniform microstructure throughout each part; particularly as a function of curvature in a specimen. The fabrication advanced from simple curved plates to periodic hexagonal SIC-SiC composite structures to serve as a base unit for a fully composite fuel rod

spacer grid structure. The hexagonal structures were made with varying amplitude and periodicity to accommodate different fuel rod diameters. Additionally, the radius of curvature at the facet transitions was varied to control composite densification and structure. Microstructural variations are an indicator of abnormal processing conditions that can degrade performance. The impact of non-planar structure processing necessitates mechanical testing of these parts. In addition to microhardness for assessing local property variation, a custom hydrostatic burst test was developed and implemented to apply uniform stress on curved structures for evaluation of these parts. Additionally, instrumented drop tests were performed on different structures to assess impact resistance. Through microstructural characterization, bulk mechanical testing, and microhardness testing, structure-property relationships were determined as a function of part complexity.

3.3.1 Non-planar geometries

The ultimate goal of non-planar SiC-SiC composite processing was to produce a spacer grid type structure. However, the principal demonstration of retaining optimal composite microstructure and properties was established in a simple curved "potato chip" components before advancing to the hexagonal strip structures for spacer grids. Initial work focused on examination of ply distribution and local property variations in as-fabricated "potato chip" curved structures. The fabric ply spacing in curved plates has been assessed via XCT and is shown in **Error! Reference source not found.**. In this example, a cylinder is fit to the plate curvature. The cylinder fit uses 10,000 points to very accurately match the specimen curvature. Using Volume Graphics VGL imaging software, the specimen was then un-rolled based on the reference cylinder such that a planar representation of the composite structure could be analyzed. With this analysis, it was determined that the spacing between adjacent plies was 155 µm ± 24 µm. The standard deviation value is less than what had been previously measured for planar composites (167 µm ± 32 µm). This result indicates that fabrication of curved structures does not introduce any added inter-ply skewing which could adversely impact mechanical performance.

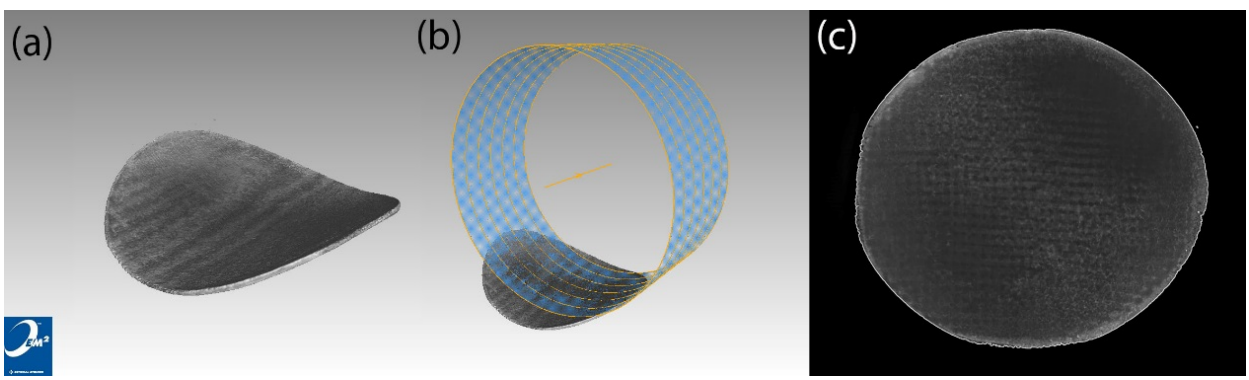

Figure 14. XCT analysis of TEP SiC-SiC curved plate with (a) the complete 3D volume of the part, (b) the cylinder fit to the curved surface via 10,000 point match, and (c) a mid-plane slice of the part taken from a volume created by unrolling the curved part base d on the cylinder fit. The mid-plane slice shows a single fabric ply across the entire plane, which indicates that the ply is parallel to the specimen surface.

Non-planar part fabrication is the first step associated with construction of an all SiC spacer grid structure. This step includes consolidation of hexagonal strips of TEP SiC-SiC that will serve as the base unit for spacer grid construction. These hexagonal strip units were subsequently bonded together to create an array of hexagonal cells that each constrain a single fuel rod (see Figure 15). A graphite tooling approach similar to what was utilized for planar complex structures was implemented in such a way that a corrugated structure was hot pressed. Hexagonal strip pieces with different periodicity and amplitude, to accommodate both LWR and EM^2 diameter fuel rods were successfully demonstrated. Furthermore, hexagonal strips were made to investigate the effect of fillet radius in the region where adjacent surfaces of the hexagonal structure intersect on part performance.

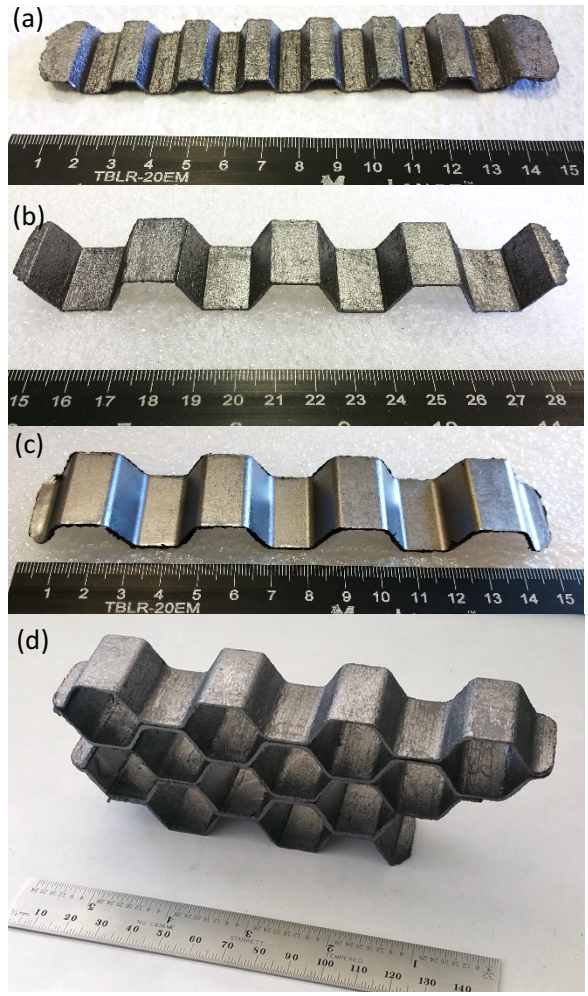

Figure 15. TEP SiC-SiC composites in various geometries: (a) LWR hexagonal strip, no fillet (b) EM2, no fillet, (c) EM2, 3 mm fillet and (d) 5 EM2 strips with 3 mm fillet arranged but unbonded in hexagonal cellular array configuration

Initially parts were consolidated without a fillet radius, however, the sharp edge resulted in significant fiber breakage and weaker part behavior. Consequently, a fillet radius was implemented into the design, which resolved fiber degradation in the transition zone. Examples of the different hexagonal strip parts are shown in Figure 15**a-c**. Additionally, a layup of multiple hexagonal strips (Figure 15**d**) illustrates how the hexagonal cellular array will look after joining has occurred.

Initially, the same processing pressure was used for the hexagonal strip structures as has been applied for other planar and nonplanar structures. However, composite specimen densities came in unexpectedly high at nearly 3.1 g/cc or 95% theoretical density. Upon microstructural evaluation via SEM, it was determined that more substantial fiber deformation was occurring in these non-planar specimens than had previously been observed in planar part consolidation. Based on the stress peaking informed by the structural modeling described in Section 5.1, process pressure was iteratively reduced to improve microstructure. However, even at drastically reduced pressures, microstructural differences are observed compared to planar or potato chip subcomponents. An example of this microstructure is shown in Figure 16. Optimal microstructure includes a clearly resolved pyrolytic carbon layer separating fiber cross sections from adjacent matrix. In these hexagonal strip specimens, no such pyrolytic carbon layer can be resolved. The oxides in the matrix have reacted with the PyC layer entirely, and even penetrated into the fiber itself, resulting in significant grain coarsening within the fibers. This microstructure is unlikely to provide the composite behavior necessary

for reactor performance. Two deleterious phenomena have occurred: (1) the reaction of the PyC interphase prevents fiber sliding from occurring meaning failure is likely to be brittle rather than composite-like, and (2) penetration of the oxide into the fiber has coarsened its structure and altered its composition in way that will reduce fiber strength and weaken the overall component. This microstructure occurs both with and without a fillet radius and is evident in all regions of the structure. Investigation of the fabric prior to consolidation did not show any obvious damage to the PyC layer, so it is likely this damage occurred at process temperature and pressure. Typically when load, temperature, or process time is too high, degraded microstructures like Figure 15(b) are observed. Future work on non-planar spacer grid type structures will necessitate use of thicker PyC layer and further reduction of process pressure to overcome this issue.

(a) (b)

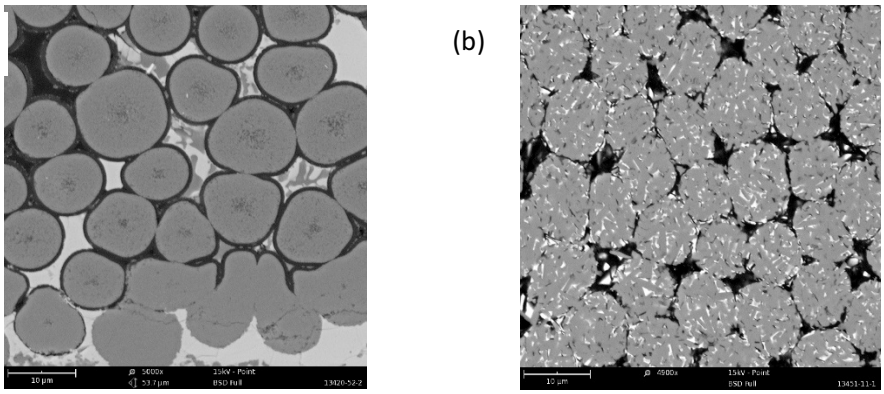

Figure 16. Comparison of composite microstructure in (a) a planar composite processed at standard TEP process pressure, and (b) a hexagonal strip composite specimen processed at 20% of standard pressure.

3.3.2 Local Property variation in curved features

Another critical concern in transitioning to curved structures is the potential for the non-planar geometry to result in local property degradation as evidenced by the hexagonal grid type structures. While the XCT and density data above suggest no deterioration in performance for curved plates, microhardness provides higher resolution assessments of any localized property variations.

Microhardness values were collected on specimen cross sections in various positions along the “potato chip” curvature. Data presented in Figure 16 compared hardness in planar and non-planar composites. Each data point represents 5 measurements, with error bars depicting one standard deviation. Data was acquired every 500 micrometers along the specimen curvature to assess spatial variations. No appreciable variation in hardness was observed as a function of position within the specimen. Similar to planar composites. Additionally, no significant difference was found between the two specimen types. The planar composite had an average microhardness of HV = 2845 ± 155, while the potato chip specimen had average microhardness of HV = 2820 ± 170.

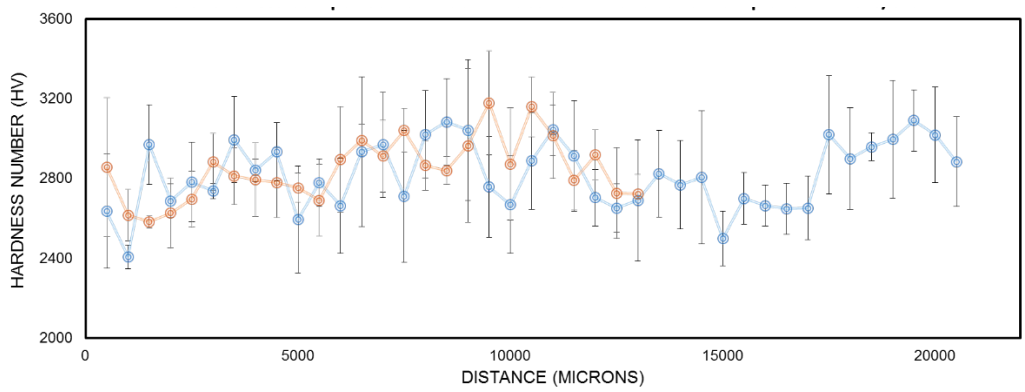

Figure 17. Micorhardness data comparing planar composite (orange) and curved "potato chip" composite (blue) specimens.

X-ray computed tomography and microhardness were conducted on hexagonal strip specimens. No significant ply skewing was observed in transitioning across hexagonal faces. Microhardness measurements were conducted at various locations in both the fibers and the matrix. The hexagonal strip was categorized into three regions: the flat, nose and angled portions of each repeating hexagonal unit. Measurements were taken across the specimen thickness in each region.

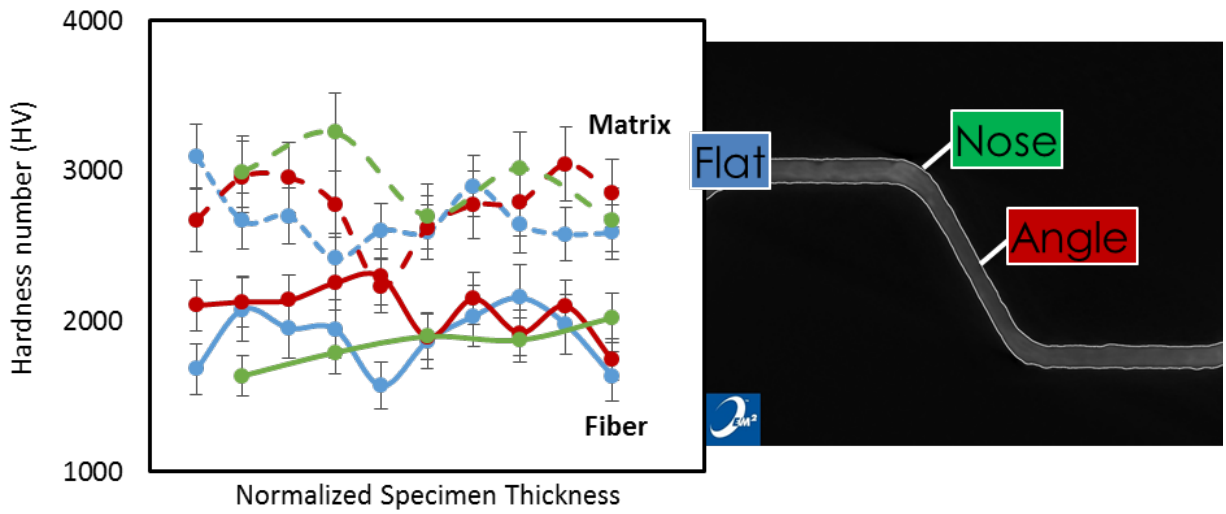

Figure 18. Microhardness data from different regions of a hexagonal strip structures with 3 mm fillet radius. Colors in hardness profiles indicate the three geometric regions identified in the XCT image at right.

The results are summarized in Figure 18. Each data point represents the numerical average of 10 individual measurements. The data bars represent plus/minus one standard deviation. Two conclusions can be drawn from the hardness data: (1) hardness is generally unaffected by location in the specimen, and (2) the average matrix and fiber hardness values of ~3000 and ~2000 HV, respectively, in the hexagonal strip specimens, are an indicator of the consolidation affects in these specimens. The matrix consolidation is quite uniform, however, the increase in fiber hardness in the nose regions, and generally higher hardness values in the fiber of hexagonal strips corroborate the microstructural evolution observed in Figure 16. Ultimately the potential for non-planar SiC-SiC composite fabrication has been demonstrated, and unlocks significant opportunities to produce complex structures for extreme environment applications, but the tool designs and processing parameters must be tailored specifically

depending on stress distributions arising from the geometric design. With due diligence these stress variations can be accommodated to produce a quality part.

3.3.3 Burst testing of curved structures

Initially, mechanical testing of curved structures was conducted using traditional three point bend test fixtures, however, the hard contact points of the load and support beams, coupled with the curved structure and stiffness of the ceramics led to substantial local crushing of the specimens at load points that invalidated tests. To overcome this testing challenge, a hydrostatic bladder test rig was designed and constructed to uniformly apply load to the specimen and get very accurate strain response from the composite deformation using DIC.

A high-pressure bladder rig was designed to accommodate the geometry of the specimen. In the rig, the specimen was placed between a pressure relief plate and a rubber foam gasket, with a rubber bladder located on the concave side of the specimen, which was used to transmit the pressure to the specimen, see schematic in Figure 19. On top of this assembly a pressure plate applied the necessary force to hold the different components and to seal the rig. The bladder rig was connected to a two-stage 10-ksi oil pump using high-pressure tubing. The pump allowed a smooth increase in pressure in the range 0-200 psi. A 500-psi pressure transducer from Omega Engineering was used to measure the pressure in the system. The evolution of damage was monitored using a Micro-II AE system equipped with a Nano-30 sensor and 20 dB pre-amplifier and the data is analyzed using AEWin software. The strains in the specimens were measured using two techniques, strain gauges and 3D-DIC. The strain gauge provided very good accuracy for the measurement of strains in small areas, and 3D-DIC was used to obtain full-field strain measurement on the curved surface of the specimen.

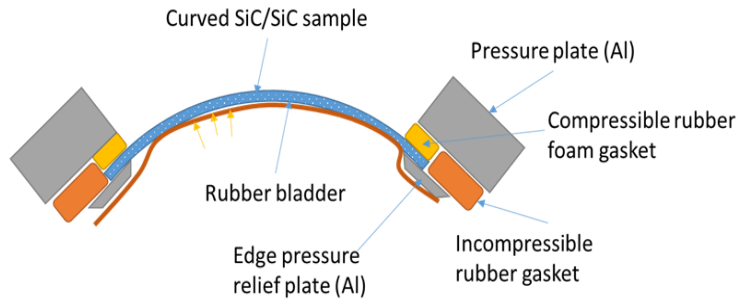

Figure 19. Schematic of bladder rig test configuration for potato chip specimen

The sample was placed in contact with a polymer bladder and the edge of the disk was held by a holding plate with soft polymer gasket placed between the face in contact. Pressurized hydraulic oil was introduced to the opposite side of the bladder so that the bladder exert a uniform pressure on the disk sample. This unique method generate a high bi-axial tensile stress near the center of the sample (away from the edge constraint) and avoided edge failure due to hard contact. The method was successfully applied to both flat and curved samples. Representative failure modes and results for a planar specimen are shown in Figure 20.

During testing, the accumulated pressure, acoustic emission energies, and strain were simultaneously monitored. Since the bladder is applying pressure to nearly the entire specimen, the stress state is far more complex than a simple uniaxial loading configuration. Furthermore, the bladder applied pressure across a much larger volume of material than the load pins in a traditional flexure test. As such, direct comparison to a small planar flexure coupon is not constructive. Instead, basic material properties such as the elastic modulus can be leveraged in conjunction with some of the data acquired on the acoustic and strain behavior of the specimens to infer performance of these large composite components and compare them to traditional measurements. This sample failed at a burst pressure of 200 psi. The strain

was measured with both a strain gauge and via digital image correlation, while the acoustic signature was simultaneously acquired. The strain gauge output has component strains in x and y directions. As expected, the bladder uniformly loaded the specimen such that strain was essentially the same in each direction. The acoustic emission data shown in Figure 20c exhibit the signature stepped energetics of SiC composite fracture. Events initiating after 365s around $5x10^7$ aJ are indicative of matrix cracking, while the higher energy events in the 10^9 aJ range indicate fiber fracture. This observation is significant because it confirms composite like fracture. The pressure signal alone cannot convey this composite behavior so the AE data is imperative for composite characterization. The strain at matrix cracking is approximately ~1500 micro-strain. This strain taken with the previously measured elastic modulus of TEP SiC-SiC of 320 GPa, allows calculation of the proportional limit stress (PLS) of these composite specimens The PLS as measured via the hydraulic burst test is 192 MPa, which is in excellent agreement with the 194 MPa average PLS strength reported in Table 1 for TEP SiC-SiC composites as measured by conventional 4 pt bend testing. Following matrix cracking, it is not possible to accurately predict the elastic modulus, so the strain cannot be used to predict fracture strength, only the pressure output can be reported.

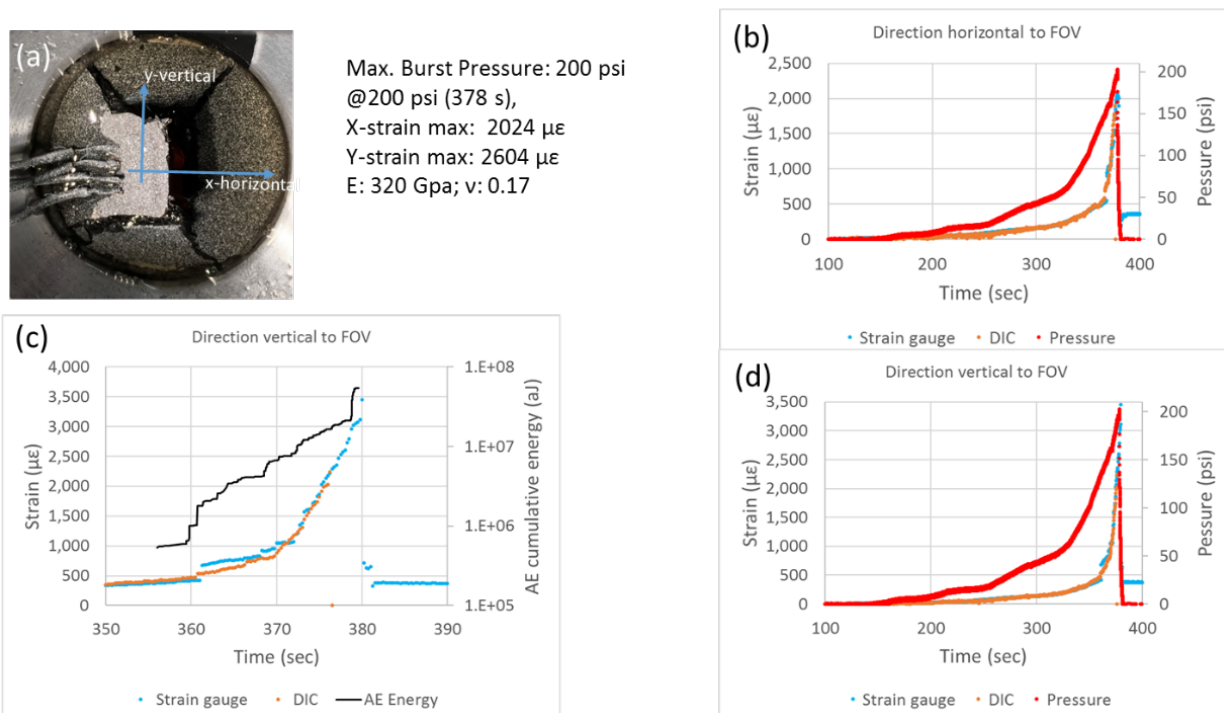

Figure 20. Hydraulic bladder flexure test for a planar specimen showing (a) a sample following testing to failure, (b) pressure and strain in the x-direction (c) DIC and AE data, and (d) pressure and strain in the y-direction.

Hydraulic bladder testing was also performed on several curved composite disks. In conjunction with the physical testing, FEM was performed to confirm uniform stress and strain application. The FEM results are shown in Figure 21 (a) and (b), for stress in the x- and y-directions, respectively. The bladder approach applies uniform stress across a large surface of the specimen. In the experiments the average burst pressure of 120 psi was comparable to planar composite disks of similar thickness (1 mm). However, the strain was both lower (only about 10-20% of the planar composites) and more directionally dependent in the curved specimen. The lower strain is unexpected given the similar microstructures observed at the fiber matrix interface between curved and planar parts. The asymmetry is expected given the geometric

stiffening generated by the crest or ridge in the curved part. DIC strain maps are presented in Figure 21c and d.

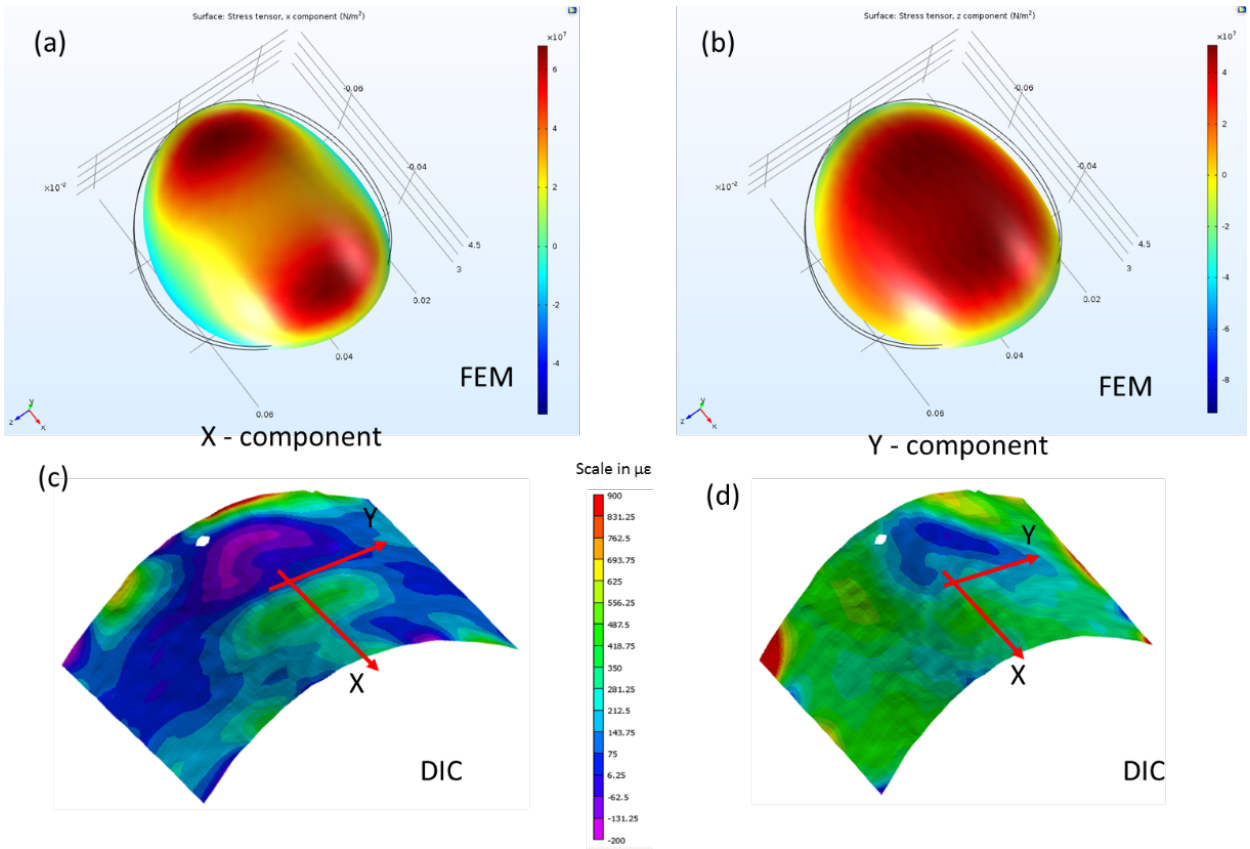

Figure 21. Details of bladder testing on curved specimen including FEM of stress distribution in x-direction (a) and y-direction (b), as well as DIC strain map in x-direction (c) and y-direction (d).

The bladder test was successfully demonstrated on planar and curved specimens. The implementation of the test established that although microhardness and microstructure appeared indistinguishable when comparing planar and curved specimens, there is a distinct loss of pseudoductility and strain to failure in curves specimens. Understanding this relationship is critical for implementation of complex non-planar SiC-SiC designs. Additionally, successful demonstration of this test methodology permitted its use for bulk comparison of specimens before and after impact tests as discussed in section 3.3.4.

3.3.4 Impact testing

In the nuclear industry, it is common to evaluate in-core structures via impact testing to simulate likely occurrences during operation and handling. While impacts may range from vertical drops of fuel assemblies during loading and unloading, to lateral fuel assembly impacts during seismic or LOCA events, as well as impact vibrations, the spacer grid is considered the most critical component in the fuel assembly with regard to impact events. Loads are typically applied perpendicular to the fuel rod axes, and the performance is evaluated based on strength retention compared to the based material [3] [4]. The simulated impact of a zircaloy spacer grid until buckling [5] served as a benchmark for comparison of the composite impact performance. In Yoon's test configuration, the spring dampened impact resulted in a .64 m/s impact velocity at a force of 9445 N. The sample geometry plays a role, but the magnitude of

these critical parameters serve as a guideline for impact performance. During the impact test, the impact force, velocity and acceleration were measured, while the potential energy and instantaneous impact velocity were calculated from the acquired data. The impulse excitation technique is used to determine the evolution of the natural frequencies and damping of the sample after repeated impact. It was found that both natural frequency and damping are indicative of damage evolution in the specimen. The correlation between the impact force, the natural frequency, and the damage development was clearly identified.

A modified Instron Dynatup 8200 HE drop tower is used for the drop weight tests (Figure 22). The impact force is measured via a piezoelectric force sensor and is recorded with a PICO Technology 5444B oscilloscope. An optic sensor is used to measure the instantaneous velocity of the impactor right before impacting the sample. The weight of the cart including the impactor is 2.76 kg. The impactor is cylindrical (12.7 mm in diameter) with a spherical contact surface (radius of curvature is 56.8 mm). The sample holder is similar to the sample holder described in ASTM-7136 [2] with an opening size suited to accommodate the nominally 50 mm specimen sizes. The sample is held between the sample holder and a steel plate by toggle clamps which apply a holding force without damaging the specimen.

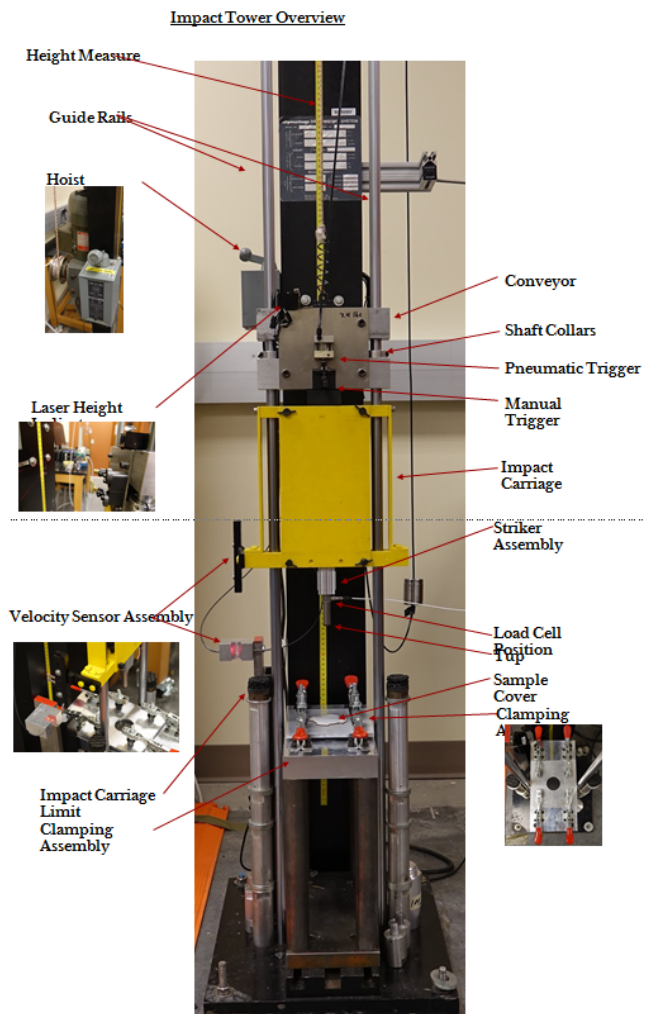

Figure 22. Drop weight impact test (DWIT) apparatus

Following the calculation method in ASTM-7136, the impact velocity is obtained by using the equation,

$$v_i = \frac{w_{12}}{t_2 - t_1}\frac{w_{12}}{t_2 - t_1} + g\left(t_i - \frac{t_1 + t_2}{2}\right)$$

Where w12 = distance between flag prongs, t1, t2 = time first and second flag prong passes detector, seconds, ti = time of initial contact,

The velocity during the impact is calculated using equation,

$$v(t) = v_i + gt - \int_0^t \frac{F(t)}{m} dt$$

Where: v_i = impact velocity, t = time, g = acceleration, F = impact force, m = mass of impactor.

The impactor displacement is calculated by using the expression

$$\delta(t) = v_i t + \frac{gt^2}{2} - \int_0^t \left(\int_0^t \frac{F(t)}{m} dt \right)$$

The transferred energy (Joules) is calculated by

$$E_a(t) = \frac{m\left(v_i^2 - v(t)^2\right)}{2} + mg\delta(t)$$

The impulse excitation technique (IE) was used to determine the resonance frequencies of the specimens. A Resonant Frequency and Damping Analyser (RFDA) System by the company IMCE is used. The specimen was excited by a small hammer positioned at a distance of 5 mm from the specimen. A microphone is used to detect the vibration frequency and amplitude. The material damping is derived from amplitude decay recorded by the microphone. The frequency and damping of the fresh specimens and the specimens before and after the drop-weight test were measured. The resonance frequency is related to the elastic properties of the material [3] impact damage typically results micro- and macro-cracking in the CMC, reducing the effective elastic properties and increasing internal damping. This makes it possible to relate the damage of the material by measuring the variation frequency and damping. Assuming the material is isotropic and homogeneous; the Young's modulus of the round specimens was calculated by [3]. This equation does not directly apply to composite samples which as anisotropic.

$$E = 3\rho D^4 (1 - \nu^2) \left[\frac{\pi f_{mn}}{h\lambda_{mn}}\right]^2$$

Where D = diameter, ρ = density, ν = Poisson's ratio, f_{mn} = frequency, λ_{mn} = f (ν, thickness/radius), and h = thickness

Repeated drop tests were performed on samples ranging from 1 mm to 6 mm in thickness and on basic and complex structures. An initial set of impact tests performed on basic planar composites conveys the method by which damage is tracked in impact tests. The specimens were 2 and 3 mm in thickness. The thicker specimens resulted in 2x higher impact forces at the same impact velocity, and were more resilient than 2 mm specimens. The 3mm specimens experienced an impact force of 1740N at a velocity of 0.52 m/s following impact from 2 cm, followed by an impact force of 1666 N at 0.71 m/s following impact from 4 cm in a subsequent event on the same specimen. After the initial impact, the sample did not show visible damage. The impact force and velocity are measured and from it, the impact energy is determined, as shown in Figure 23. The 0.7 J impact energy is typical for composite specimen of this 48 mm diameter. The gap in the energy hysteresis loop indicates the energy absorbed by the SiC composite following impact.

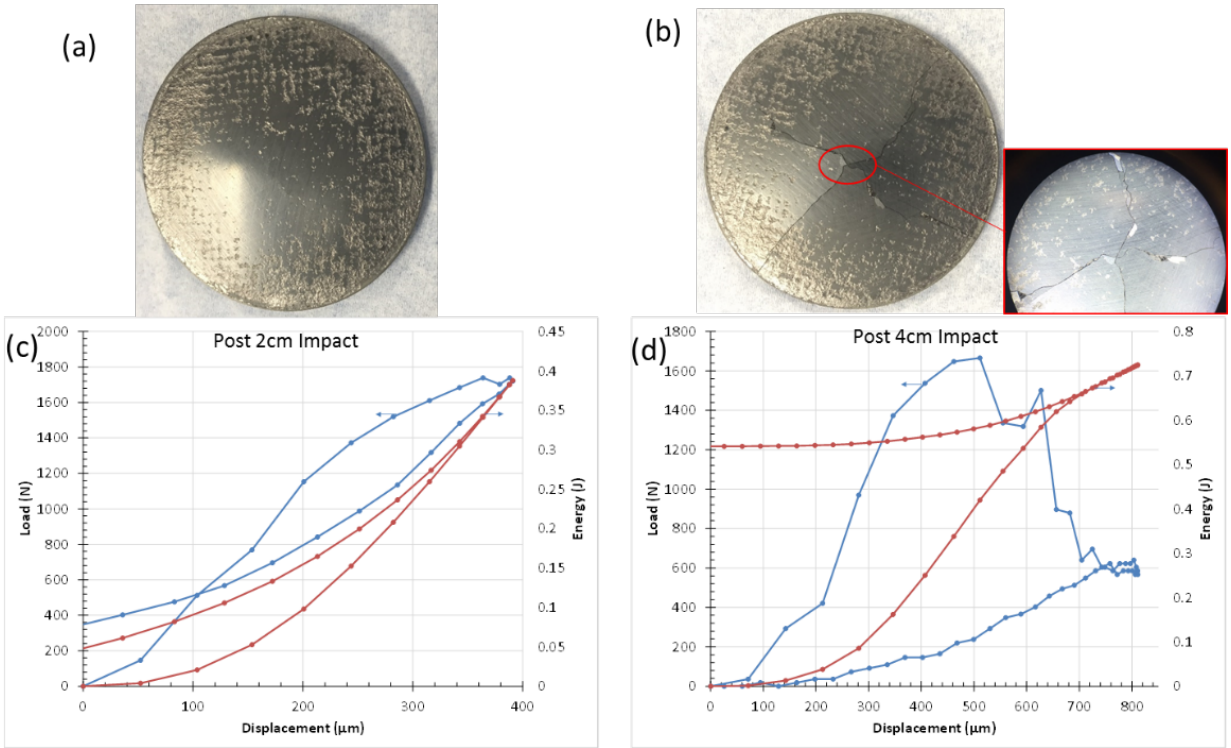

Figure 23. Impact test results for 3mm thick TEP SiC-SiC showing same specimen after 2cm drop (a), 4cm drop (b), impact energy after 2 cm drop (c) and impact energy after 4 cm drop (d).

The post impact bladder testing revealed that, following a 2 cm impact event, 2mm thick composite specimens retained 46% of their strength, dropping from 200 psi to 83 psi, while 3mm thick composite specimens exhibited a 97% strength retention (391 psi to 386 psi), which is well within the anticipated distribution in strength for a ceramic matrix composite. Residual strength can only be measured on samples following impact if they did not experience any significant cracking. If such cracking is observed, the residual strength is expected to be less than 25%. It is of note that composite performance is maintained following multiple impacts such that, if extended to a nuclear component, even if damage is incurred, a coolable geometry can still be maintained. This is a significant result given the dearth of impact data on CMC material. Such conclusions must be considered with the fact that impact force and energy are geometrically dependent, and a larger spacer grid type structure is likely to be more compliant.

Though more than 40 impact tests were performed, the resilience of the SiC-SiC composites produced in this work are best described through a subset of tests performed to progressively damage specimens through repeated impact on both basic and complex structures. For the basic composite SiC-SiC specimen CS-BD-C-13537-58-1, the drop height started from 20 mm, and then increased 20 mm for each test after, until visible crack was observed on the surface of the specimen after a 120 mm drop. For the samples with 5 holes, CS-5H-MM-C-13537-62-1, the drop height was 20 mm repeated 3 times, no crack was identified. Then the drop height was raised to 40 mm, after which a crack was observed. After each drop, pictures of the front and back surface of the specimen were taken. Optical microscope was used to take crack details during the inspection. An impulse excitation test was also performed to capture the natural frequency of the sample.

The solid sample (CS-BD-C-13537-58-1) as shown in Figure 24 has experienced repeated impact, ranging from 20 mm to 120 mm, with 20 mm increase for each step. The sample showed a visible crack

on the surface after the 120 mm impact. The impact force time history and natural frequency were studied after the experiment.

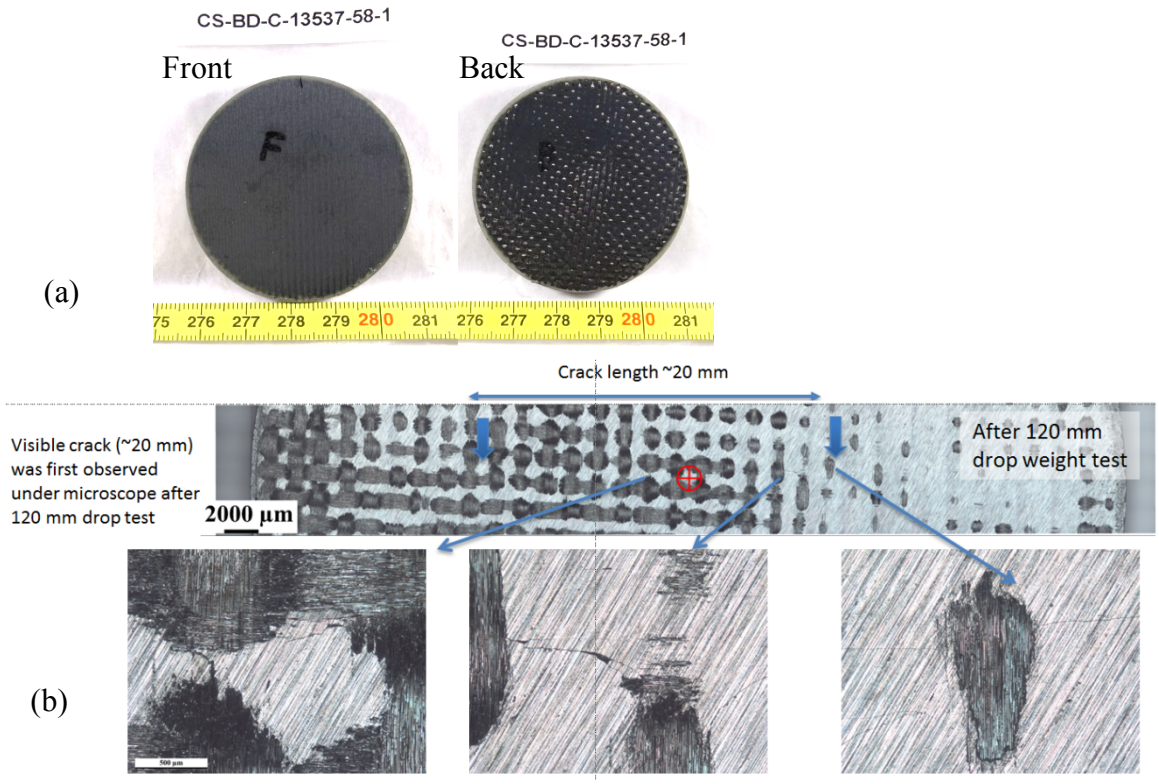

Figure 24. Images of specimen CS-BD-C-13537-58-1 (a) before test, and (b) after indicating visible damage from repeated drop test including details of hairline crack extension

A typical impact, contact force, and energy plot is shown in Figure 25. The force and energy curves are both bell shaped. For a perfect elastic impact event, the force curve is perfectly symmetrical, and the energy curve returns to zero at the end. For the case shown in Figure 25 some damage was generated during the impact, hence the absorbed energy is greater than zero (~0.22J). Some small disturbances on the second leg of the force curve were also observed, indicating loss of support from the specimen due to material damage.

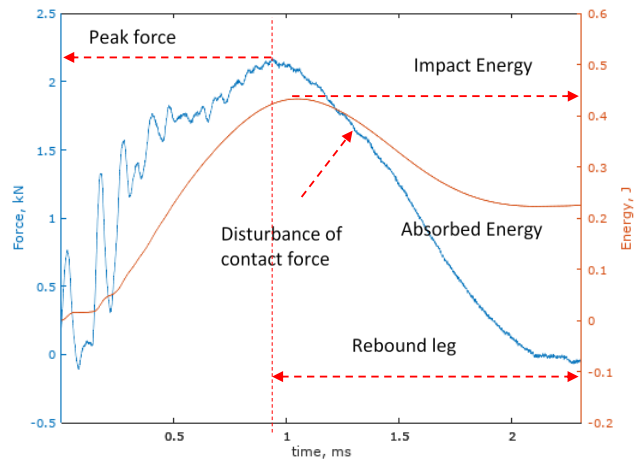

Figure 25. Typical impact force and absorbed energy time history plot during a drop weight impact test. The absorbed energy indicates there are energy loss during the impact event

The impact force and energy history from sample CS-BD-C-13537-58-1 is shown in Figure 26. Clearly, the impact force and energy are larger for higher drop height. Every force curve showed some level of force drop on the "rebound" leg of the impact events, indicating some level of damage to the material. It is also interesting to note that the more impact energy, the more absorbed energy is presented at the end of the impact. Furthermore, with the increased level of damage, the maximum impact force is reduced, such that the two events of 100 mm and 120 mm drop have almost the same maximum force. As shown in Figure 27, the natural frequency captured using IE method also clearly shows a steadily increasing frequency shift during the test. Both the flexural and torsional mode frequency showed almost identical trend of change.

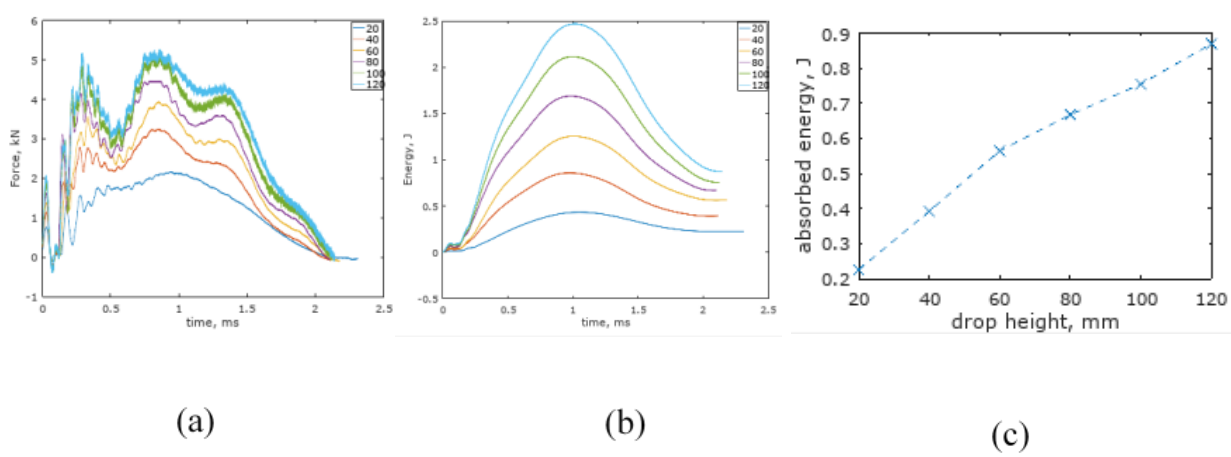

Figure 26. Specimen CS-BD-C-13537-58-1 impact force time history and absorbed energy plot during a drop weight impact test. (a) Impact force time history, (b) energy time history, and (c) energy absorbed by specimen. The drop heights are increased from 20 mm to 120 mm with a 20 mm step. Gradually increasing absorbed energy indicates damage accumulation during the repeated impact events.

The complex composite specimen, CS-5H-MM-13537-62-1, is a joined 3 layer vent manifold structure containing 5 open holes on one side, 4 holes on the other side, and a central channel in the mid plane. The impactor was incident on the 4 hole side of the specimen such that the 5 hole side was put in tension on impact. This specimen was subjected to three subsequent 20 mm impacts. Because no clear sign of

crack were noticed, the drop height was increase to 40 mm, at which point the sample cracked. The impact force time history and natural frequency are studied after the experiment. The specimen is shown in Figure 28

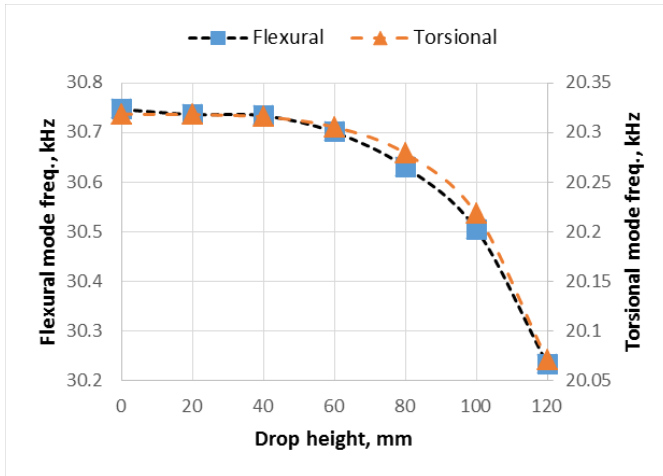

Figure 27. Sample CS-BD-C-13537-58-1 impulse excitation test data after drop weight impact test. The frequency of the first flexural vibration mode and the first torsional vibration mode are plotted against the drop height. The deviation of vibration frequencies indicates a gradually increasing damage induced by repeated impact events

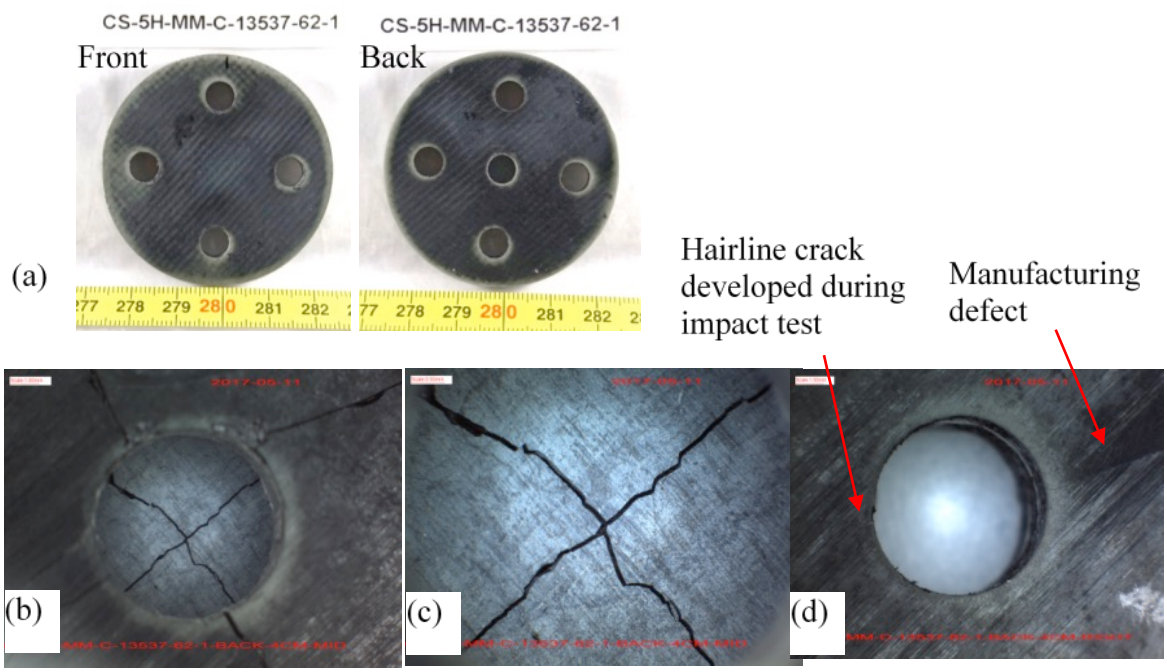

Figure 28. Sample CS-5H-MM-13537-62-1 pictures (a) before test, and (b)-(d) visible damages after repeated drop test. The specimen cracked after 4 repeated drop tests. In (b) radial cracks formed at the center hole directly under the impact site, both the front and the back layer are cracked in a similar pattern; (c) crack propagation along the fiber direction in the underlying fabric layer; and (d) around one of the outer holes, a smaller crack developed along a consolidation defect.

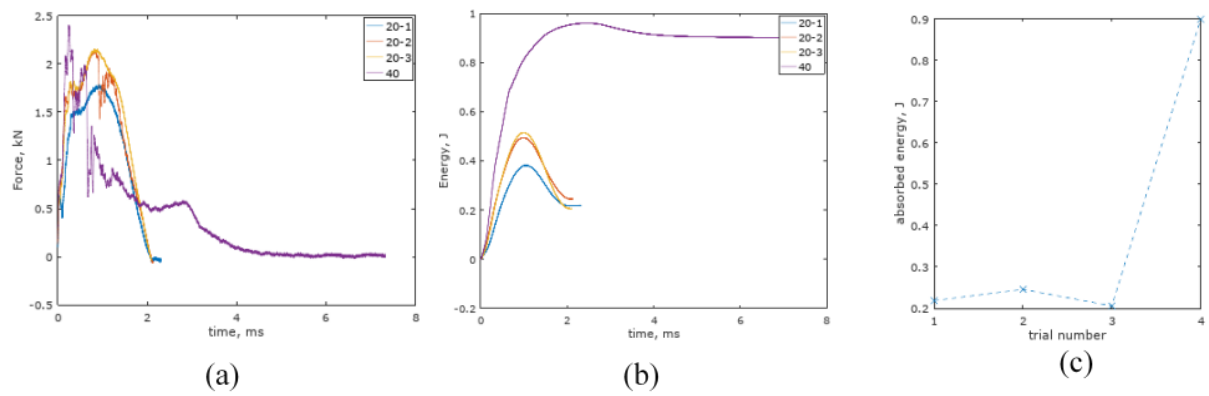

Figure 29. Sample CS-5H-MM-13537-62-1 impact force time history and absorbed energy plot during a drop weight impact test. (a) Impact force time history, (b) energy time history, and (c) energy absorbed by specimen. The drop heights are 20 mm repeated three times, and then a 40 mm drop test. The absorbed energy plot (c) indicates slight increase in absorbed energy following the second impact, and a much more pronounced energy absorption following the 40 mm impact indicative of more widespread induced damage.

The impact force and energy history from sample CS-5H-MM-13537-62-1 is shown in Figure 29. As expected, the three 20 mm drop trials present force and energy curves similar to that from the solid sample. Then the 40 mm drop force curve took much longer time to complete the impact process. It also shows many drops on the rebound leg, indicates damage propagation during the impact. The absorbed energy also show similar behavior, where almost all the impact energy are absorbed by the specimen in the 40 mm drop.

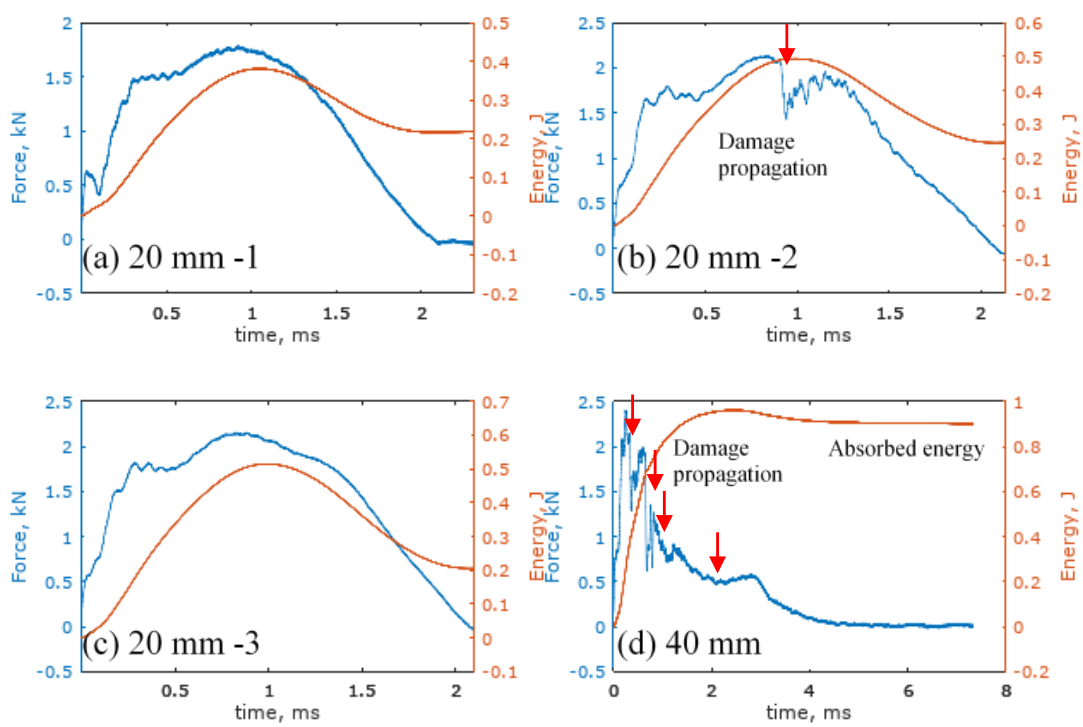

Figure 30. Sample CS-5H-MM-13537-62-1 Impact force and energy time history plots indicate the damage accumulation, propagation, and the final cracking during a repeated impact events.(a)-(c) are for three repeated 20 mm drop; and (d) is the final 40 mm drop, when large scale cracking was observed.

Detailed impact force and energy plots are shown in Figure 30. It is interesting to notice that the first and third 20 mm drop events are showing very similar force curve and absorbed energy (about 0.2 J), while the second 20 mm event shows a clear force drop around 1 ms, which identifies a significant damage propagation during this impact. The energy plot also shows more absorbed energy (about 0.25 J). The 40 mm drop event shows multiple large force drops on the rebound leg. The force curve is distinctively different from the 20 mm drops. The energy curve also indicates significant energy absorption during the event. As shown in Figure 31, the natural frequency captured using IE method also clearly shows a similar behavior, where the second 20 mm drop induced noticeable frequency shift, while the first and third drop are virtually not changing frequency.

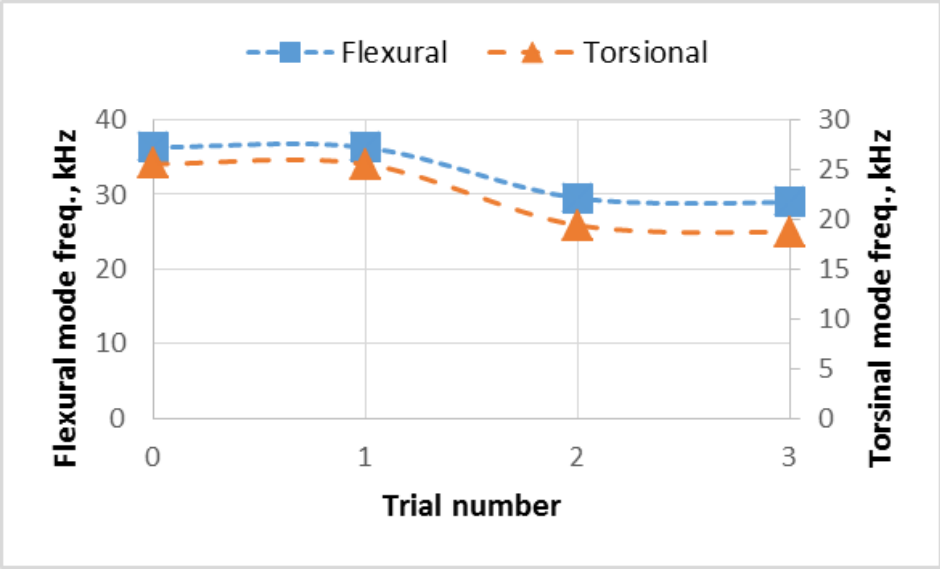

Figure 31. Sample CS-5H-MM-13537-62-1 impulse excitation test data after drop weight impact test. The frequency of the first flexural vibration mode and the first torsional vibration mode are plotted against the drop height. The deviation of vibration frequencies corroborate the gradually increasing damage induced by the repeated impact events.

The impact force and absorbed energy are related to the level of damage induced in the material. IE was used to study the damage evolution and proved extremely sensitive in detecting changes in natural frequency even when damage is not visible. This was corroborated by very slight decreases in strength of material when bladder tests were performed following impact. Further, the lessons learned from impact response of these composites can be extended, through dynamic mechanical modeling as described in section 5.2, to much more complex geometries. The notable outcomes of this work were clear retention of composite behavior in all composite structures following low velocity impact, and perhaps equally important, the potential use of IE as an NDE tool to monitor induced damage in SiC-SiC composite reactor components following transport or seismic events. Additional study is needed to build a statistical model predicting the damage level from impact data and natural frequencies. Future study will focus on establishing the impact damage model using both theoretical and numerical methods. This work has shown that relationships between frequency change and strength drop can be established such that easy to measure frequency response of a component can tell an operator whether that component retained the requisite strength to remain in operation following an event.

3.4 Fabrication of Multi-layer SiC-SiC Composite Sub-Components by Modular Joining

Joining for SiC and SiC-SiC composites for nuclear application is an enabling technology. Katoh et al. reported on several nuclear joining technologies for SiC [6]. Most joints suffer from radiation induced microstructure evolution and micro cracking. Among the joints evaluated only the TEP joints showed both no microstructural evolution and minimal strength change after irradiation. This is not surprising since the same formula has been used to fabricate monolithic SiC ceramics and SiC-SiC composites, which are microstructurally stable under irradiation to medium doses [7]. Because of these promising results from the literature, the TEP based joining methods were chosen to be the focus of our joint development. The basic steps of the TEP joining method include fabrication of the slurry with various formulas, applying the slurry to the substrates and finally heat treating the parts in the hot press with various hot pressing pressure and temperature profiles to form the final joints. Ultimately, the successful evaluation of this joining technology and demonstration of this joining technique enabled its deployment as a means to create additional part complexity in SiC-SiC composites through joining multiple substructures.

3.4.1 Initial screening and development of the TEP joint process

Various TEP based joints medium and TEP based sandwich joints (using CVD SiC as substrates), which were derived from pre-mixed slurries containing SiC powder, oxide powders (SiO_2, Al_2O_3 and Y_2O_3) and organic additives were fabricated and subsequently characterized. In order to have a systematic understanding of the effect of oxide content, five different formulations designated as GA-TEP1 to GA-TEP5 with GA-TEP1 having the lowest oxide content and GA-TEP5 the highest oxide content were evaluated. Various joining temperatures and hot press pressures were also investigated and designated as T1<T2<T3<T4<T5<1900°C and P1<P2< P3<P4<P5<50 MPa. GA-TEP1-T5-P4 represents the standard TEP process, which has been used in composites as well as initial joints. All other joints were processed at lesser or equal temperature and pressure.

3.4.1.1 Thermal gravimetric analysis (TGA) and differential scanning calorimetry (DSC) study of TEP based joint slurry

A STD Q600 (TA Instruments) instrument was used to for thermal gravimetric analysis (TGA) and differential scanning calorimetry (DSC) measurements at a heating rate of 5 °C/min from room temperature up to 1500 °C in a flowing argon atmosphere (100 ml/min) in order to analyze the organic additive burn out, the releasing of volatile compounds at higher temperatures, and melting of the oxides. The DSC curves for GA-TEP1, GA-TEP2, and GA-TEP5 are shown in Figure 32. The DSC data confirm that the organic additive burn-off process is affected by the oxide content with higher oxide content formulas showing earlier onset of burn off at 200°C. The large exothermal peak between 1300 and 1500 °C for GA-TEP1 and GA-TEP5 is speculated to be caused by the forming of the liquid phase. GA-TEP2 behaves quite differently, showing an earlier onset of the exothermal peak at 1150 °C. The SiO_2 - Al_2O_3 - Y_2O_3 ternary system has been studied both thermodynamically and experimentally. The formation of liquid phase around 1400 °C has been reported [8]. It should be noted that no significant weight loss is associated with the formation of the liquid phase according to TGA data.

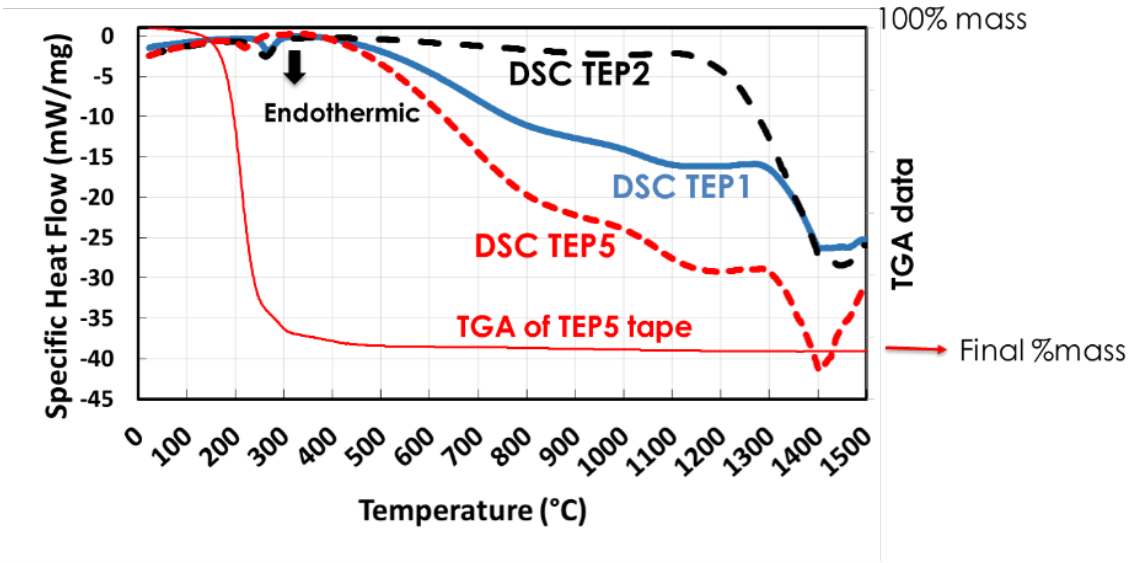

Figure 32 DSC and TGA curves of TEP SiC joint precursor in flowing argon atmosphere

3.4.1.2 *XCT and SEM study of various TEP based joints*

X-ray computed tomography (XCT) images of various specimens are shown in Figure 33. Drastically different joint layer appearances were shown by XCT. Figure 33-(1) shows a joint with the highest processing temperature (T5) and pressure (P4) using the lowest oxide content formulation (GA-TEP1). Some river-like patterns are seen in GA-TEP1. Those dark areas represent voids in the joint layer and will be discussed later in this section. Figure 33-(2) and (3) show two joints specimens with higher oxide content and lower processing temperature and pressure. More pronounced microstructure development was observed especially with increased joint oxide content from TEP2 to TEP3. Figure 33-(4) and (5) show two joints with the highest oxide content, joined at same pressure but at different temperatures (T2 and T1). Both images suggest complete melting of the joint layer during processing with a non-wetting behavior between the melted joint layer and the CVD SiC substrate. GA-TEP5-T2-P1 has a higher processing temperature than T1 and shows a joint layer with large voids, while GA-TEP5-T1-P1 joint has a lower processing temperature and shows a network of small interconnected voids. One possible explanation is that at a higher processing temperature, the oxide melt has a lower viscosity, which facilitated coalescence of the TEP melt, resulting in a continuous layer of joint material with large voids. In contrast, at a lower joint temperature, T1, the joint layer showed an island-like appearance with voids

surrounding the islands. This type of appearance suggests the coalescence of the joint material (the islands) is incomplete.

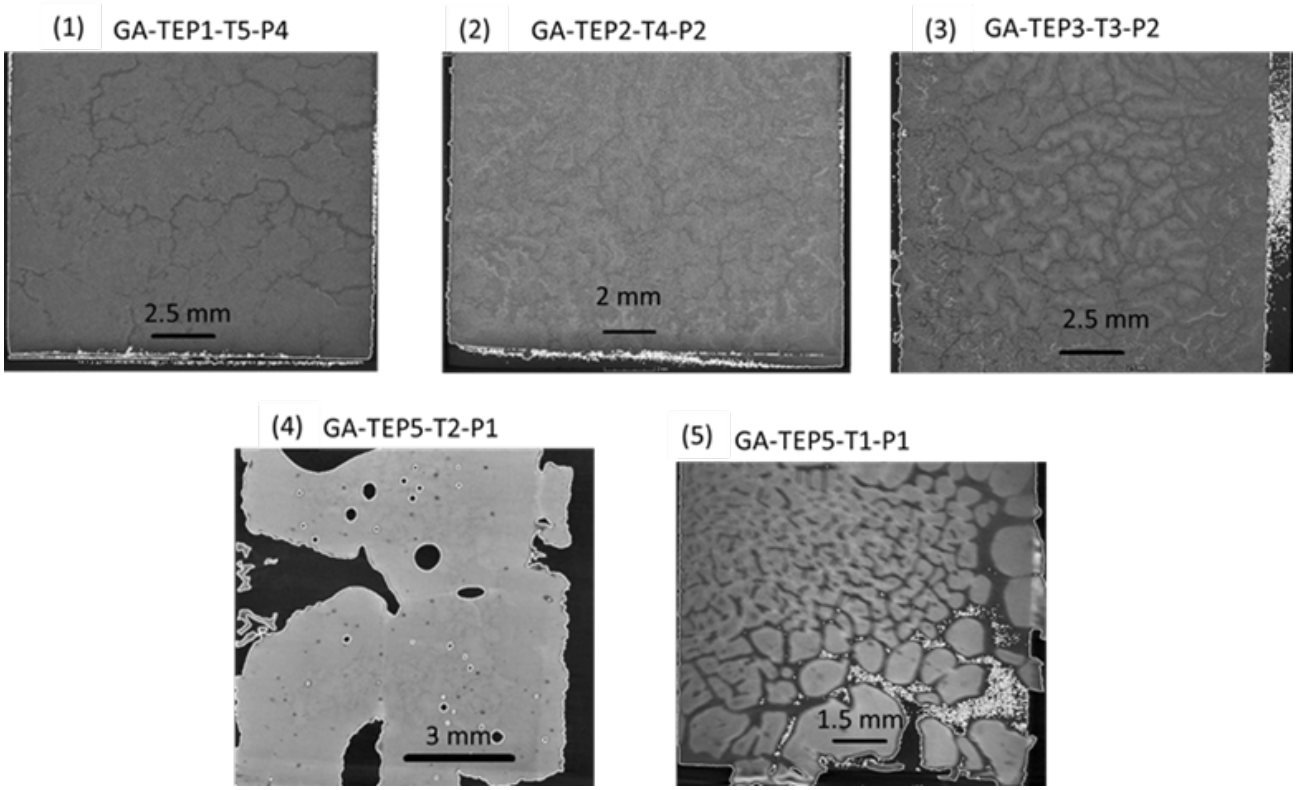

Figure 33 XCT images of selected sandwich joint specimens showing the microstructure of the joint layer

Selected back scatter electron SEM images of joint specimens are shown in Figure 34. Sample GA-TEP1-T5-P4 showed a high density joint area with evenly distributed oxide sintering aids (white contrast phase). This high density joint layer is attributed to the high processing temperature and pressure. Figure 34-(2) shows SEM image of GA-TEP2-T4-P2 joint, in which large voids span the joint thickness. This type of microstructure suggests that these process parameters are unlikely to achieve a mechanically strong and hermetic joint without significant improvement

Figure 34-(3) and (4) show SEM images of GA-TEP5-T2-P1 and GA-TEP5-T1-P1 joints, respectively. The two joints utilized the same high oxide content but are processed at different temperatures. Both joints showed a bright contrast matrix and dark contrast yttrium aluminum silicate (YAG) precipitate particles embedded in the matrix. Some large precipitates in the size of 8 µm were observed in GA-TEP5-T2-P1 joint layer likely because the higher processing temperature promoted more precipitate grain growth upon

cooling. A large through thickness void can be seen on the left side of Figure 34-(4). This through thickness void corresponds to the dark area in the XCT image Figure 33-(5)

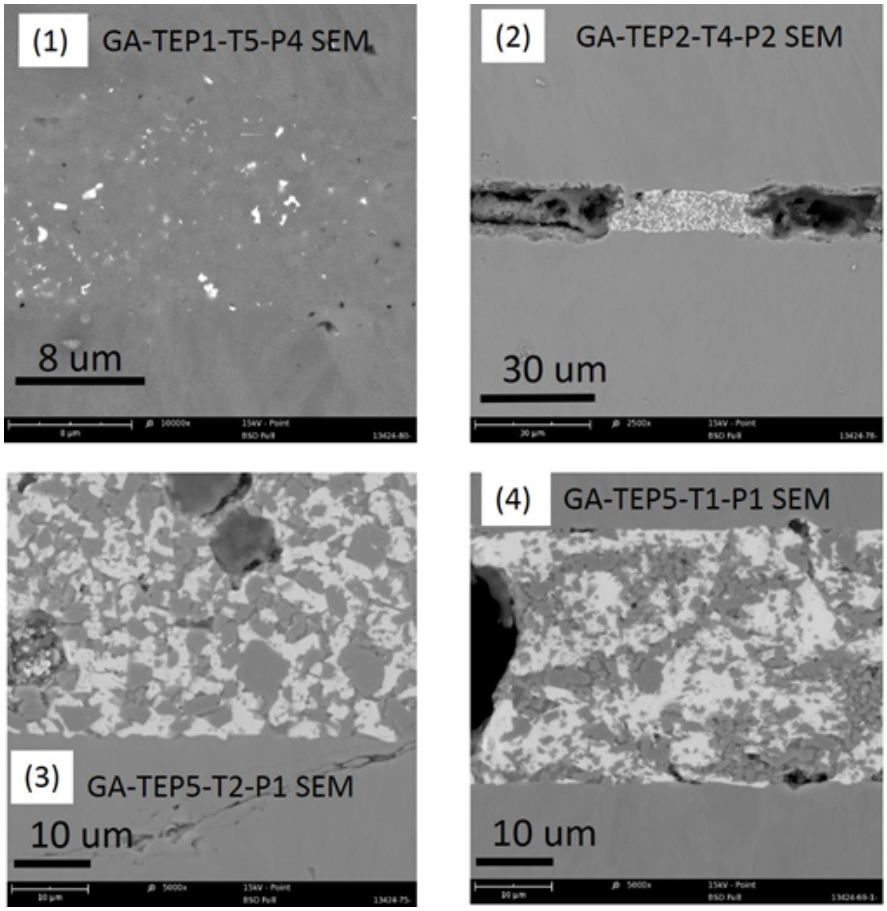

Figure 34 SEM images of various TEP joint cross-sections

3.4.1.3 Shear test of various TEP joints for initial screening

The apparent shear strength of selected joints was determined with double notch shear (DNS) test at room temperature. General guidelines of the ASTM C1292 were followed for the DNS test. The DNS specimen size is about 15 to 20 (Length) X 10 (width) X 12 (thickness) mm. The distance between the notches is 3 mm, the notch width is 0.5 mm, and the notch radius of curvature is 0.4 mm. Figure 35 shows the first results of the DNS tests. The reference joint GA-TEP1-T5-P4 showed apparent shear strength of 85.1 MPa. Substrate failure was observed for this specimen. Substrate failure is common when using DNS to evaluate shear strength of particularly strong SiC sandwich joints; it indicates a joint that is approaching the strength of the substrates it's joining.

GA-TEP2-T4-P2 and GA-TEP3-T3-P2 failed along the joint interface (adhesive failure) at substantially lower stress than the reference specimen. The crack initiated from the edge of a through thickness void and propagated between the interface of the substrate and the joint layer. Optical microscope images of GA-TEP3-T3-P2 joint before and after DNS test are shown in Figure 36. The low apparent shear strength indicates that chemical bonding between the GA-TEP2 or GA-TEP3 and the SiC substrate was weak at these processing temperatures and pressures, even though melting of the oxides sintering aids were

expected at these processing conditions. This finding suggests that merely having oxide sintering aids in a liquid state, even in relatively large quantities, is not enough to create strong bonding between the joint layer and the substrate. Temperatures much higher than the liquid phase forming temperatures are necessary to promote strong chemical bonding between the joint layer and the SiC substrate.

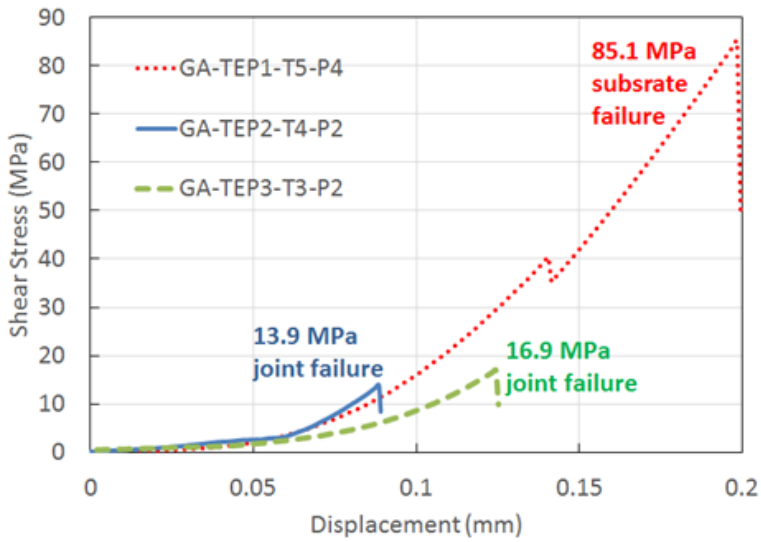

Figure 35 DNS stress-displacement curves for different TEP joints

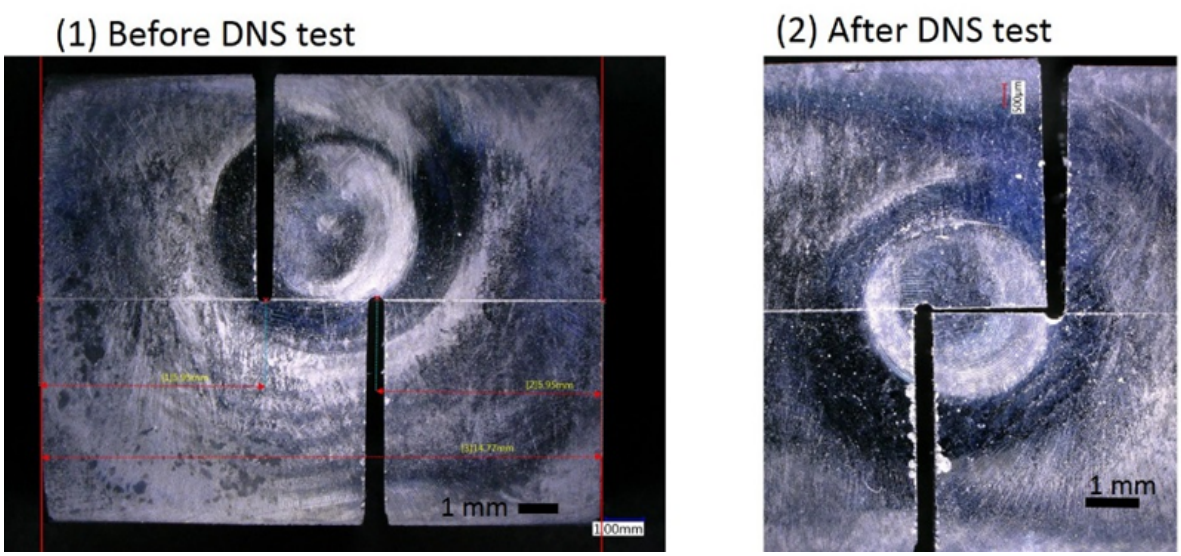

Figure 36 Optical microscope images of notched GA-TEP3-T3-P2 specimen before and after DNS test

3.4.2 Determination of upper-bond joint processing temperature limit through TEP SiC-SiC composite substrate heat treatment

The high temperature during the joining process might damage the TEP SiC-SiC composite substrate and this phenomenon needs to be investigated in order to make complex and mechanically sound SiC-SiC parts through modular joining. For this reason, standard 2D planar TEP SiC-SiC composite disks

fabricated under this study were heat treated at 1600, 1700 and 1800 °C under argon atmosphere for one hour and the room temperature flexural strength retention following the high temperature heat treatment was investigated. The results are summarized in Figure 37. Representative stress extension curves are shown in Figure 38 . Figure 39 shows SEM images of the composite fracture surface after heat treatment. While it is necessary to heat to at least 1600°C to achieve a robust joint, there is a penalty for processing at higher temperatures. Processing joints at 1600°C resulted in ~97% strength retention, while 1700°C exposure results in 93% strength retention. In both cases, typical pseudo ductility of composite behavior were observed. The degradation in strength is attributed to coarsening of the fiber microstructure as well as volatilization of the oxide containing phases. 1800°C heat treatment results in the destruction of the composites. Bearing this in mind, one must either minimize joint processing temperature or design the end use components with knowledge of the reduced strength in joined structures.

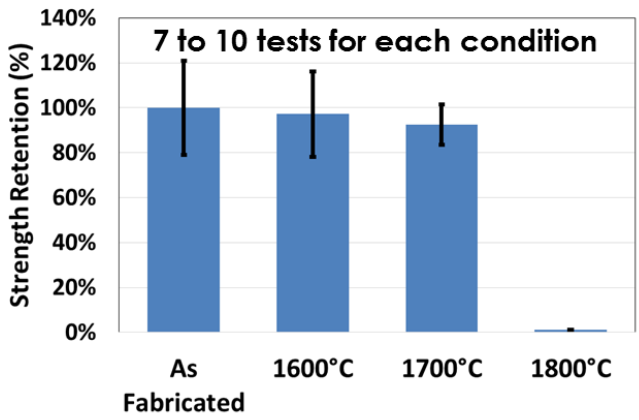

Figure 37 Average flexure strength of as-fabricated and heat treated TEP SiC composites. Each bar represents the average of 7 to 10 tests. Error bars indicate +/- 1 standard deviation

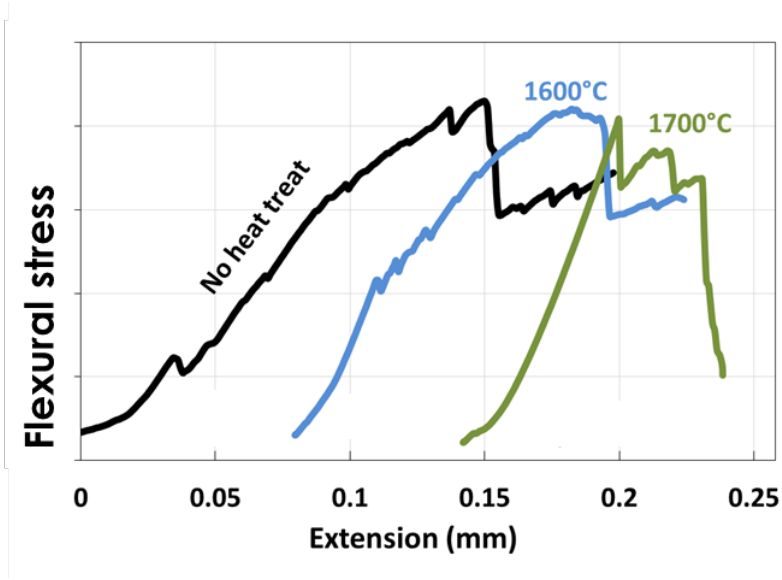

Figure 38 Representative stress extension curves of as fabricated and heat treated TEP SiC-SiC composites

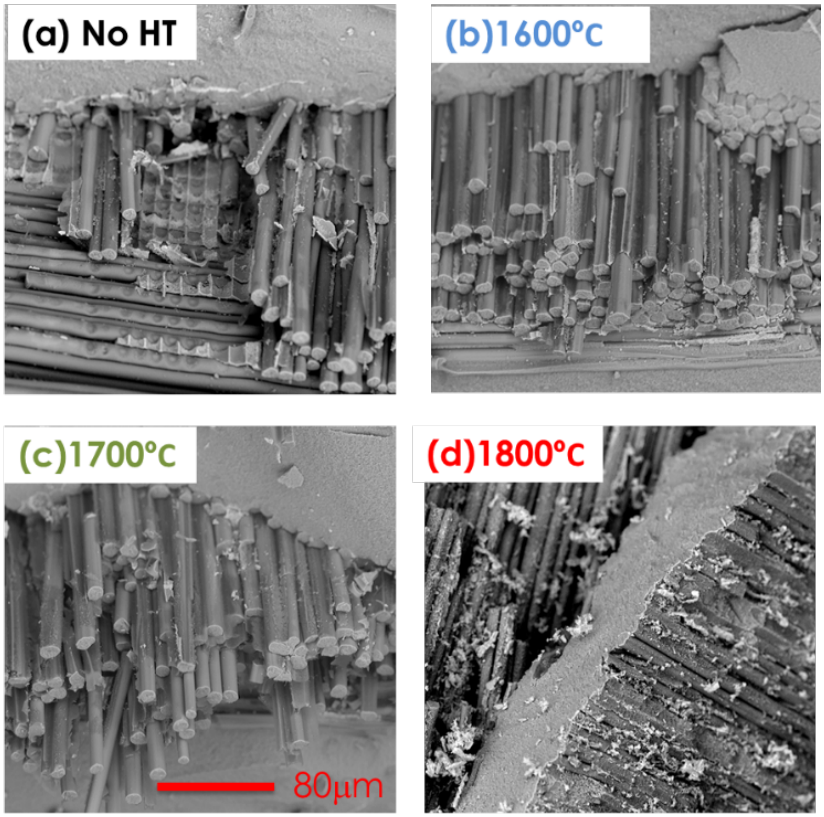

Figure 39 Fracture surface SEM images of as fabricated and heat treated TEP SiC-SiC composites

3.4.3 Development of low temperature TEP based joints

3.4.3.1 Low temperature TEP based joint with lowered oxide content

From the TEP SiC-SiC composites heat treatment studies, it was established that joining process temperatures at or below 1600 °C is desired in order to prevent damage to the SiC-SiC composite substrates during the joining process. It has been established that a high oxide content joint composition (TEP4) can successfully join CVD SiC substrates at 1600°C with good mechanical strength. In this section, efforts on reducing oxide content while still using a low joining temperature of 1600°C and maintaining the desired high joint shear strength were reported. The process parameters and shear strength of selected low temperature joints are shown in Table 2, which also contains a GA-HSiC joint as a reference.

Table 2 Process conditions and mechanical properties of various TEP based and GA-HSiC joints

Specimen ID	Joint type	Joining temperature	Joining pressure	DNS shear strength	Failure location
-	-	°C	-	MPa	-
13453-23	TEP4	1600	P1	54	Substrate
13453-27	TEP4	1600	P5	77	Substrate
13453-36	TEP4	1550	P5	52	Substrate
13453-41	TEP3	1600	P5	109	Substrate
13453-45	TEP3	1600	P5	78	Substrate
13453-08	TEP2	1600	P4	15	Joint
13219-41	GA-HSiC	1600	<1	11	Joint

The results suggest that for forming a mechanically strong joint, the oxide content can be reduced by 33% (TEP4 to TEP 3). Further reducing the oxide content an additional 50 % (TEP3 to TEP2) results in a weak joint, indicated by the lower shear strength together with change of failure location from substrate to joint layer indicative of weaker interfacial reaction. Reduction in joint oxide content can extend the service lifetime of joined SiC structures exposed to neutron fluence. It is therefore imperative to assess the strength requirements for a given application. The joint formulation yielding the highest strength isn't necessarily the best. In fact the GA-HSiC joint has been shown to provide sufficient strength to exceed anticipated end of life pressurization in a PWR fuel rod [9] and the DNS strength of every joint demonstrated in this project exceeds that of GA-HSiC.

3.4.3.2 Joint sintering process development for improved joint microstructure

In order to reduce the evolution of macro-pores in the TEP joints during fabrication, a "two-step" sintering process was implemented. The low temperature, low ramp rate, initial stage of this process reduces the formation of macro-pores by controlling the evolution of volatile species. The microstructure of the joints fabricated with the original (one-step) and the modified (two-step) sintering profiles are shown in Figure 40. All the process parameters are the same except the sintering profile and can be found in Table 2. With the two-step sintering profile, the oxide segregation and the formation of macro-pores were nearly eliminated. This results in a much more homogeneous joint microstructure. It is worth noting that a significant difference in joint thickness was observed for the two sintering profiles. It is speculated that a large portion of the joint medium is being "squeezed out" of the sandwich joint at low temperatures of 100 to 300 °C when the organic binder starts to soften, resulting in a thin final joint thickness with large pores scattered around the joint layer. For applications where hermeticity is not a major concern, thin, one-step sintered joints can still be a viable option. The joint shear strength associated with the two different sintering profile is discussed in the next section.

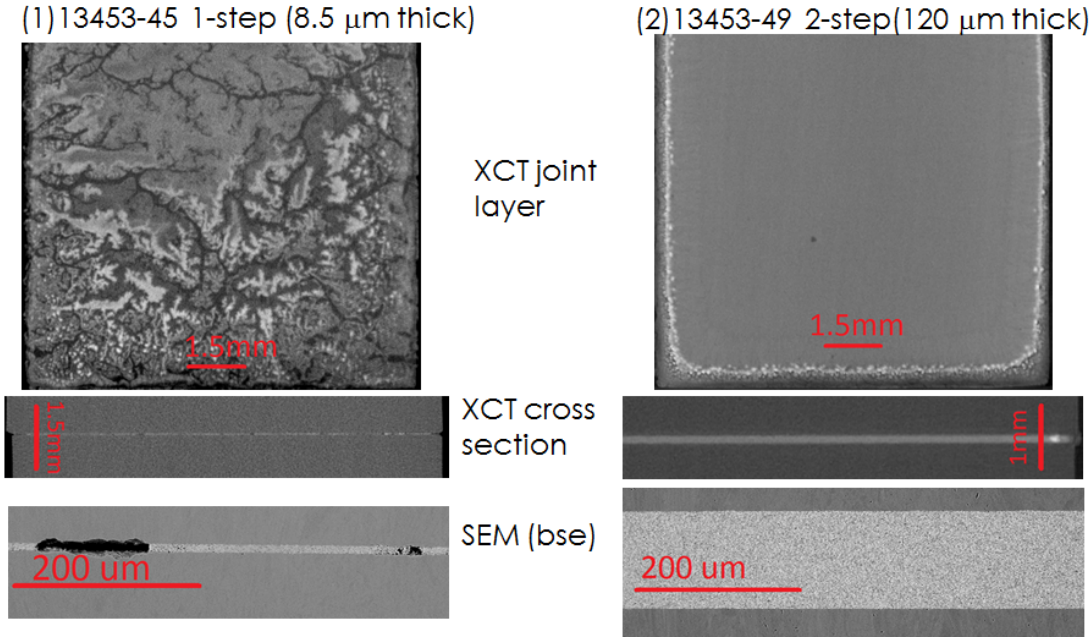

Figure 40 Microstructure of TEP3 joints with one-step and two-step sintering profiles

An investigation of the microstructure of the two-step sintered, 120 μm thick joint 13453-49 revealed some thru-thickness cracks as shown in Figure 41-(1). These cracks penetrated from the joint layer into the CVD SiC substrates on both sides. The depth to which the cracks extended into the substrates is ~33 μm, also shown in Figure 41-(1). The cracks are caused by coefficient of thermal expansion (CTE) mismatch between the joint layer and the CVD SiC substrate. This morphology suggests that the oxide rich joint layer has a higher CTE than the substrates. Thus, upon cooling from the joining temperature, experienced a residual tensile stress, while the substrates see a residual compression stress. This type of behavior has been reported before for other type of SiC sandwich joints e.g. glass ceramic joint and titanium diffusion-bonded joint [6].

Fabrication of joints with reduced final joint thickness of 46 μm (Figure 41) using the two step sintering process decreased the penetration depth of the crack into the SiC substrates from 33 μm to 4 μm (Figure 41). The thru-thickness crack appears to propagate trans-granularly through the SiC grains (rather than between them) in the joint layer, indicating strong bonding between the oxide phase and the SiC phase within the joint and along the interface. Evidence of this strong reaction between the disparate phases provides insight into the nature of the high joint shear strength.

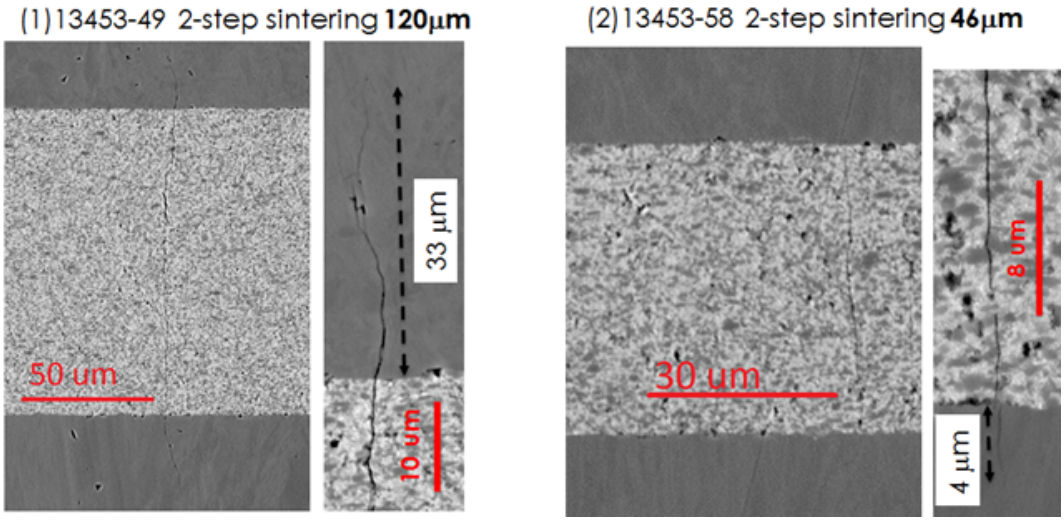

Figure 41 . Back scattered SEM images of two joints with different thickness and its effects on crack propagation into the substrate

3.4.3.3 Strength improvement of low temperature TEP joints with two-step sintering process

The DNS shear strength of the TEP3 sandwich joints processed at 1600°C, with P5 pressure are summarized in Table 3. Optical microscopy images showing the fracture patterns are presented in Figure 42. The one-step sintered specimen 13453-45 showed a strong shear strength of 109 MPa, demonstrating the insensitivity of the shear strength to the macro pores and microstructure inhomogeneity inside the joint layer. The two-step sintered 120 μm thick joint 13453-49 showed a low shear strength of 16 MPa, despite its macroporosity-free microstructure. Large strength improvement with the two-step sintering route was observed when the joint thickness was reduced from 120 μm to 46 μm, with the apparent shear strength reaching 90 MPa. The fracture pattern images in Figure 42 suggest that the low shear strength of the two-step sintered thick joint (13453-49) are caused by through-thickness crack extension into the CVD SiC substrates.

Table 3 Summary of DNS test shear strength for TEP3 joints processed at 1600°C, 30MPa

Specimen ID	Sintering	Joint thickness	DNS shear strength	Failure location
-	-	µm	MPa	-
13453-45	1-step	8.5	109	Substrate
13453-49	2-step	120	16	Substrate
13453-58	2-step, thin tape	46	90	Substrate

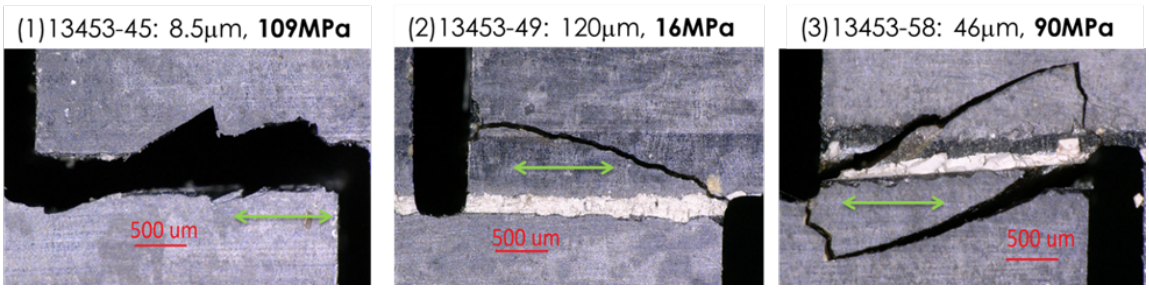

Figure 42 Optical microscopy images of specimens following DNS test, showing the fracture pattern. The green arrow indicates the shear direction

3.4.4 Joint layer TEM examination

Three TEP based joint samples were chosen for microstructural analysis using a transmission electron microscope (TEM). The TEM used in this study is a TecnaiTM TEM G2 Sphera with an operating voltage of 200 kV. The joint process parameters are summarized in Table 4. All three joints showed strong bonding between the substrate and joint material. The objective of the TEM work was to investigate the nature of this strong bonding behavior at higher resolution.

Table 4 List of joints chosen for TEM work

Specimen ID	Joint type	Sintering profile	Joining temperature	Joining pressure	Joint layer thickness	Joint DNS strength
-	-	-	°C	-	µm	MPa
13424-80	TEP1	1-step	1800	P4	13.5	85
13453-23	TEP4	1-step	1600	P1	4	54
13453-27	TEP4	1-step	1600	P5	6	77

A back scattered electron SEM image and a low magnification TEM image of specimen 13424-80 are shown in Figure 43. The TEM specimens were prepared using Focused Ion Beam (FIB) machining such that specimens could be prepared precisely at the substrate/joint interface. The green arrows indicate the joint interface between the CVD SiC substrate and the joint layer. In the SEM image, the oxide sintering aid (the white contrast phase) appears to be well distributed without any obvious agglomeration. Unlike SEM, there is no contrast difference between the SiC grains and the oxide sintering aids in the TEM images. However, the TEM image provides very clearly resolved grain boundaries. Both SEM and TEM images show a dense joint layer with negligible porosity. The low magnification TEM image shows SiC grain size inside the joint layer is approximately 1 µm. This finding suggests significant grain growth inside the joint layer

at the processing temperature of 1800°C since the SiC particles used to fabricate the green tape have a nominal diameter of less than 100 nm.

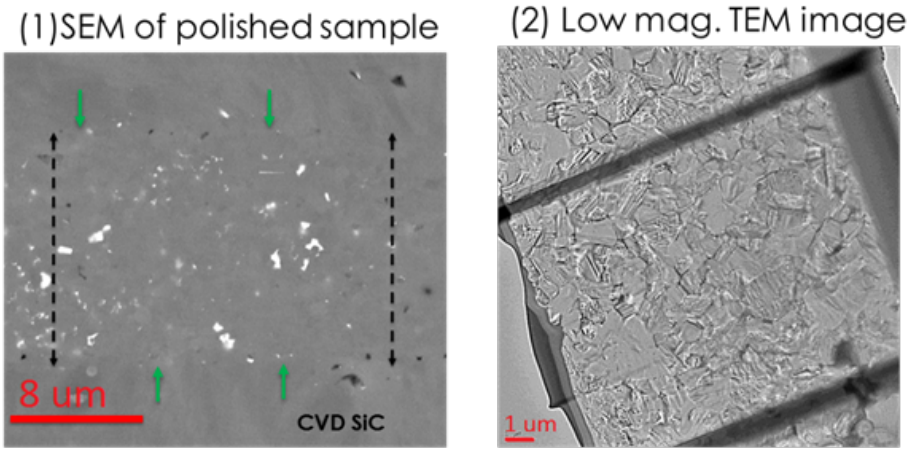

Figure 43 SEM and low magnification TEM image of specimen 13424-80. The entire field of view in the TEM image is joint material.

Figure 44 shows a series of TEM images and two selected area electron diffraction (SAED) patterns (d and f) of specimen 13424-80. The green arrows indicates the joint interface between the substrate and the joint layer. In Figure 44-(a) AND (b), the columnar grain structure of the CVD SiC (top section) and the rounded grains in the joint layer (bottom section) can be distinguished easily. The grain boundaries of the rounded grains inside the joint layer are atomically sharp with no sign of oxide except at the grain boundary triple points. Figure 44-(c) shows the oxide sintering aids at high magnification, and the SAED pattern is presented in Figure 44-(d). The lattice constant estimate from the SAED pattern of 2.87 Å, indicates mullite ($Al_6Si_2O_{13}$) phase as a reactive byproduct of the sintering aid with the SiC within the joint layer. Figure 44-(e) shows an area where individual grains and grain boundaries can been observed. The interface at the substrate is also atomically sharp with no sign of defects or pore formation. The non-linear interface also suggests dramatic reaction of the joint layer into the substrate. The corresponding SAED pattern is shown in Figure 44-(f). A lattice constant of 3.08 Å was determined from the SAED pattern corresponding to SiC.

Figure 45 shows the back scattered SEM images of sample 13453-23 and 27 (processed at process pressures P1 and P5, respectively). No detectable difference was observed with the SEM or TEM pictures for the two specimens. The insensitivity of the joint microstructure to the joint pressure is attributed to the high oxide content TEP4 joint medium. Because no difference in microstructure was observed between the two specimens, only TEM images from specimen 13453-27 are shown (Figure 46). The joint interface is indicated by the green arrows. The interface appears to be very clearly defined with minimal voids and also non-linear, indicative of significant interfacial reactivity.

The large island-like grains 1 to 2 μm in size are observed in the SEM and TEM images. The contrast in the SEM images (Figure 45 and the SAED patterns (Figure 46-(E)) from TEM suggest that these large island like grains are SiC. The oxide rich matrix, white in the SEM images, consists of small crystalline grains less than 100 nm, which are clearly resolved in the TEM images.

Some small pores with size less than 30 nm are observed both within the joint and along the interface between joint and substrate. These pores appear bright white in TEM (Figure 46-(C) and (D)) and are

highlighted with blue arrows. The pore morphology suggests that pores are not interconnected and represent an extremely low fraction of the overall joint and interfacial boundary, and thus are not expected to significantly affect hermeticity or strength. Typically, only larger macro-pores impact performance and the two stage sintering process has eliminated such defects.

SAED pattern of the oxide matrix region is shown in Figure 46-(F). The identified lattice parameter of 6.96 Å and two fold symmetry indicative of monoclinic crystal structure correspond well with the YAM phase ($Y_4Al_2O_9$, 7.26 Å) and the β-$Y_2Si_2O_7$ phase (6.87 Å). The $Y_2Si_2O_7$ phase has been reported previously for similar joints [10].

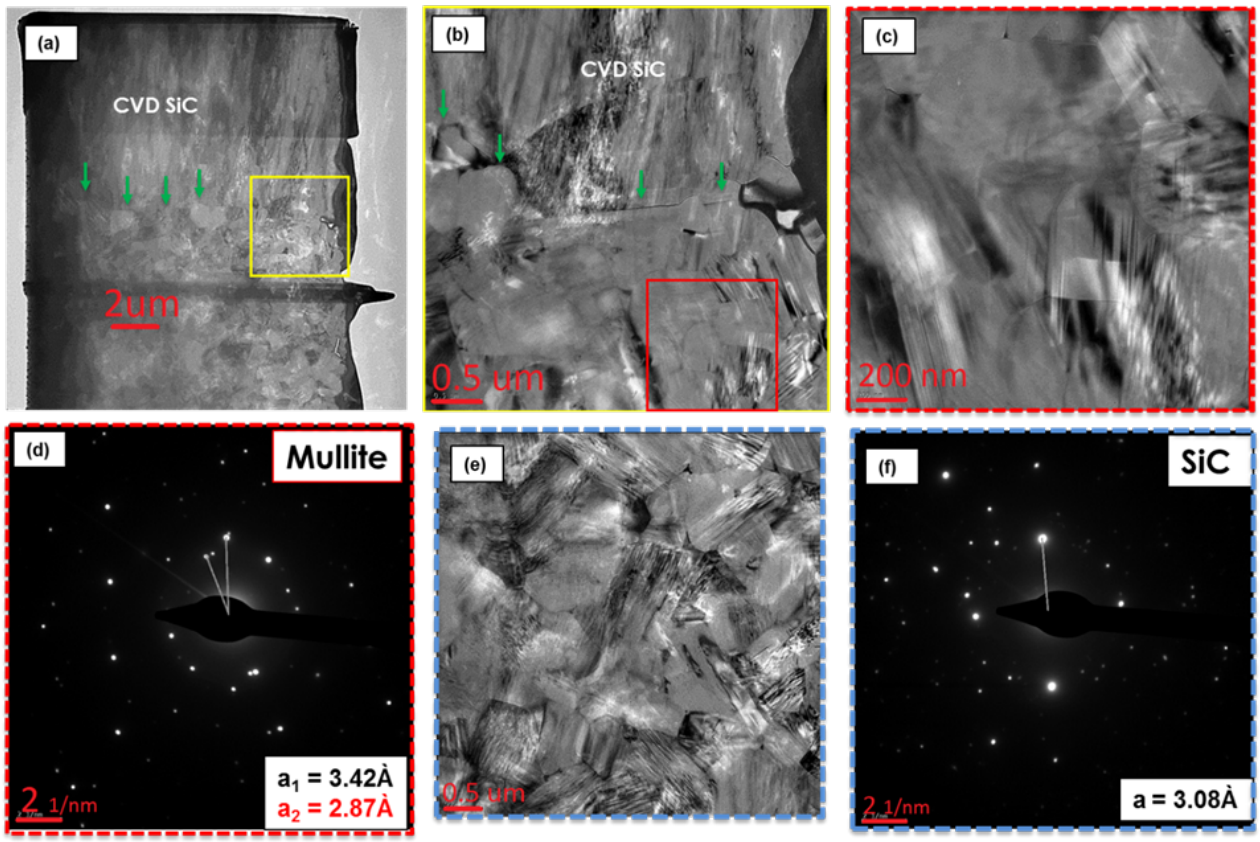

Figure 44 TEM images and selected area diffraction patterns (d and e) of specimen 13424-80. The colored boxes in (1) and (2) indicate the regions where higher magnification images and SAED were taken.

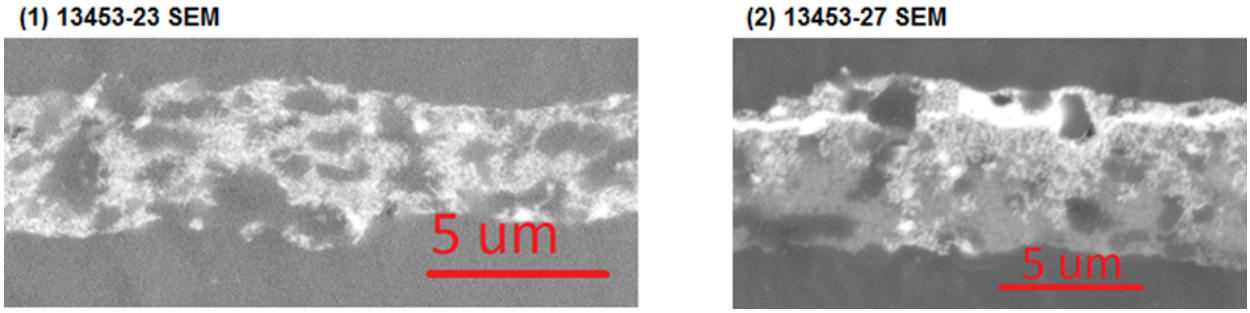

Figure 45 Back-scattered electron SEM images of joint 13453-23 and 27

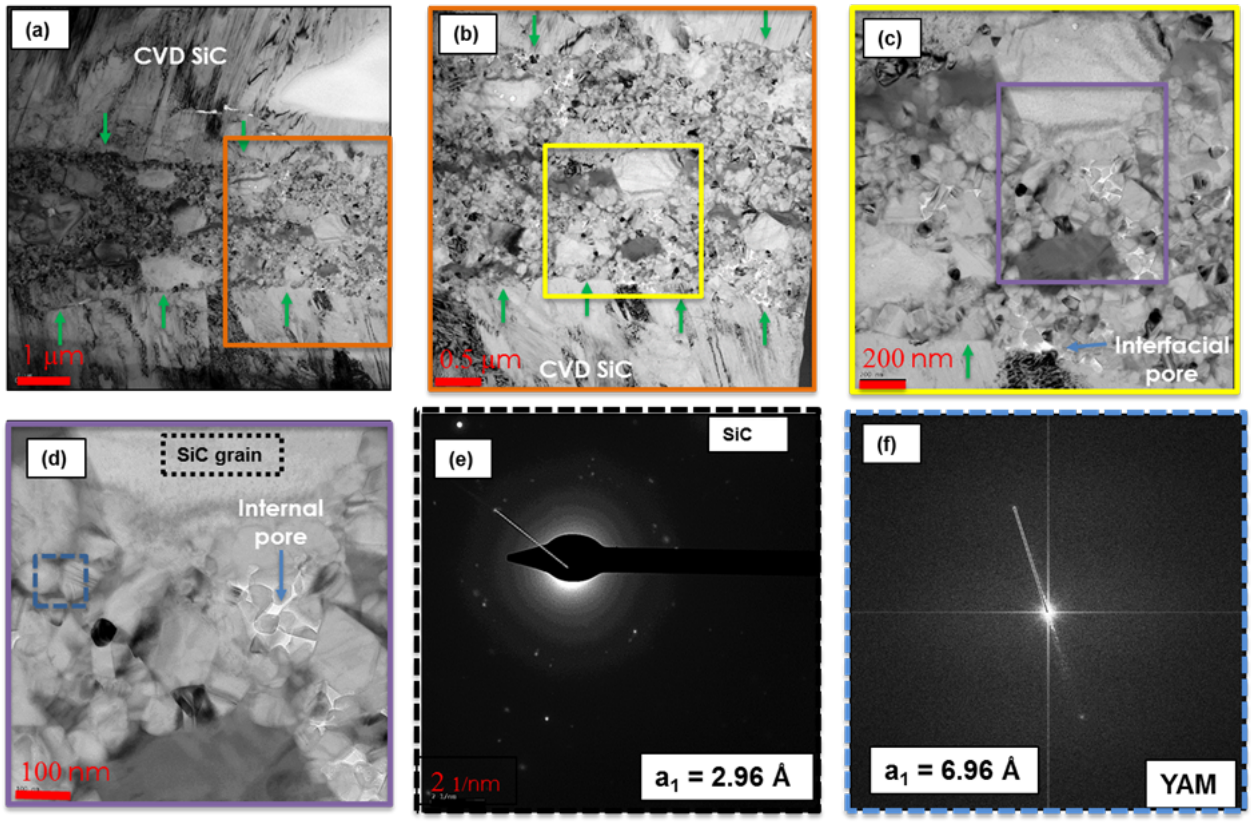

Figure 46 TEM images and SAED patterns of specimen 13453-27. Green arrows indicate joint interface, blue arrows indicate pores, and colored boxes indicate areas of interest SAED and high magnification images.

3.4.5 Hermeticity of Joined Structures

Hermeticity of selected joints was investigated in a test rig previously developed at GA using a helium leak detector. The schematic of the rig and a photograph of the sample mounted on a steel flange are shown in Figure 47-(a) and (b), respectively. One side of the joint specimen is connected to a chamber which is pressurized with helium to 10 psi gauge pressure. The other side of the joint is connected to a vacuum chamber and a helium leak detector, making the total pressure difference 24.7 psi. The leak rate results are shown in Table 5 and the microstructure of the specimens are shown in Figure 48. Please refer to Figure 40-(2) for microstructure of sample 13453-49.

Very low leak rate, below the instrument detection limit of 1.0E-11 atm-cc/sec is observed for sample 13453-60, which is processed at 1800°C. The joint layer structure in this sample is similar to the matrix of the TEP SiC-SiC composites in this study. The hermetic nature of this sample suggests that the matrix of the TEP SiC-SiC composite is impermeable. The 1600°C processed TEP3 joint 13453-62 also showed hermetic behavior. The microstructure of this sample in Figure 48-(b) suggests the existence of some fine, nano-sized pores. The fact that this sample is hermetic confirmed that those nano-pores are not inter-connected and. Sample 13453-41 and 49 had leak rates of 3.0E-6 and 9.6E-6 atm-cc/sec. The two samples have very uniform microstructures other than the through thickness cracks which are identified as the source of the leak. This suggests that for application where hermeticity is critical, the through thickness cracks need to be avoided.

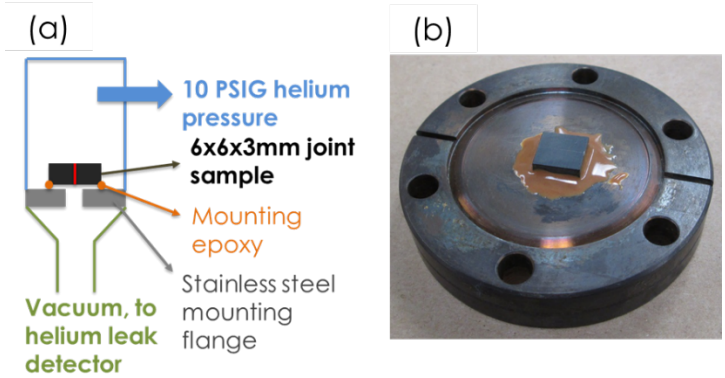

Figure 47 (a): Schematic of the hermeticity test rig and (b): a photograph of a joint specimen mounted on a metal flange

Table 5 Helium leak rate of various joints under a pressure difference of 24.7 psi

Material ID	Joint type	Joining temperature	Joining pressure	Joint thickness	He leak rate
-	-	°C	-	μm	atm-cc/sec
13453-60	TEP1	1800	P2	100	$< 1 \times 10^{-11}$
13453-62	TEP3	1600	P2	8	$< 1 \times 10^{-11}$
13453-41	TEP3	1600	P5	65	3.0×10^{-6}
13453-49	TEP3	1600	P5	120	9.6×10^{-6}

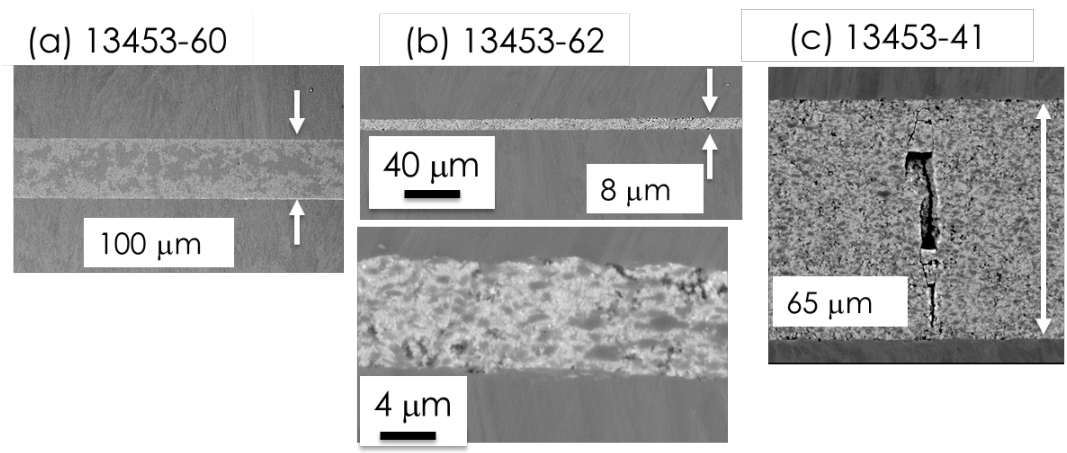

Figure 48 SEM images showing microstructure of hermeticity samples

3.4.6 *Shear strength measurement from large sandwich plates*

Large plates of CVD SiC were joined using selected process parameters. From each large joint plate, four double notch shear specimens were machined by an outside vendor (BOMAS) to gain statistical insight into the variability in the joint strength. The process parameters and shear strength, evaluated by the double-notched shear (DNS) test, of large sandwich joints are shown together with small joints as a

reference in Table 6. All specimens sectioned from large plates show moderate shear strength of 40 to 60 MPa except specimen 13453-42L, which showed a low shear strength of 8.1 MPa. The standard deviation for these sample sets were somewhat large, but reasonable due to the stochastic nature of failure in ceramic materials

Table 6 List of large joint specimen process parameters and shear strength where oxide content in TEP2<TEP3<TEP4, and process pressure P1<P3<P5<50 MPa. "L" in ID indicates large plate specimen, "S" indicates small specimen. Four tests specimens were prepared from each "L" sample, while only a single test specimen was prepared form each "S" specimen.

ID	Medium Type	Sintering profile	Joining T	Joining pressure	Joint thickness	Joint Shear Strength	Standard Deviation
-	-	-	°C	MPa	μm	MPa	MPa
13453-42L	**TEP4**	**1-step**	**1600**	**P1**	**130**	**8.1**	**7.0**
13453-23S	TEP4	1-step	1600	P1	4	54	--
13453-62S	TEP3	1-step	1600	P3	8	101.7	--
13453-47L	**TEP3**	**1-step**	**1600**	**P5**	**120**	**58.9**	**21.9**
13453-41S	TEP3	1-step	1600	P5	65	109.0	--
13453-56L	**TEP3**	**2-step**	**1600**	**P5**	**135**	**42.2**	**11.1**
13453-58	TEP3	2-step	1600	P5	46	90.0	--
13453-59L	**TEP2**	**2-step**	**1600**	**P5**	**170**	**49.8**	**3.8**
13453-08S	TEP2	1-step	1600	P5	15	-	--

Optical microscopy images of specimen 13453-42L before and after DNS test are shown in Figure 49. According to the images, the joint thickness is estimated to be around 100 μm. This is significantly thicker than the small sandwich joint processed under the same conditions (13453-23S), which showed a joint layer thickness of 4 to 10 μm using identical process conditions. This substrate size effect on final joint thickness is speculated to be caused by the required 0.5 kN pre-load of the hot press. This pre-load results in a 5x difference in applied stress between the small and large sandwich joints due to surface area difference. When small joints were processed, the combined effect of low joint slurry viscosity and high compressive pressure in the hot press at temperatures below 200°C caused the joining slurry to be squeezed out, resulting in a thin joint. When large substrates were used, the compressive stress is reduced enough to prevent the slurry from squeezing out process, which results in a thick joint. Although the high temperature process pressure was the same for small and large plate joint specimens, the slurry squeezing out process had a profound effect not only on the joint thickness but also on the joint layer microstructure and consequently, the joint strength.

Figure 49-(2) shows an adhesive failure of a 13453-42L series joint between the substrate and the joint layer, suggesting a weak chemical bonding condition between the joint medium and the CVD substrate. Since other large sandwich joints processed at the same temperature (1600°C) but with lower oxide content (TEP3 vs TEP 4) showed much higher strength, the low joint medium/substrate binding strength is attributed to the low hot press pressure (P1). This suggests that hot press pressure has a direct impact on the strength of the sandwich joint. It should be noted that the same process parameters can be used to produce stronger and thinner joints when small substrates are used. This increased strength for small sandwich joint is attributed to the change in joint thickness, joint microstructure and joint phase formation, which are all associated with the joint slurry squeezing out step occurring below 200°C.

For comparison, a TEP3 joint sample 13453-62S hot pressed at intermediate pressure (P2) using small size substrates is included Table 6. This joint has a thickness of 8 μm because of the aforementioned joint slurry squeeze out effect. The high apparent shear strength of 101.7 MPa is attributed to the thin joint layer, which eliminates the through-thickness cracks.

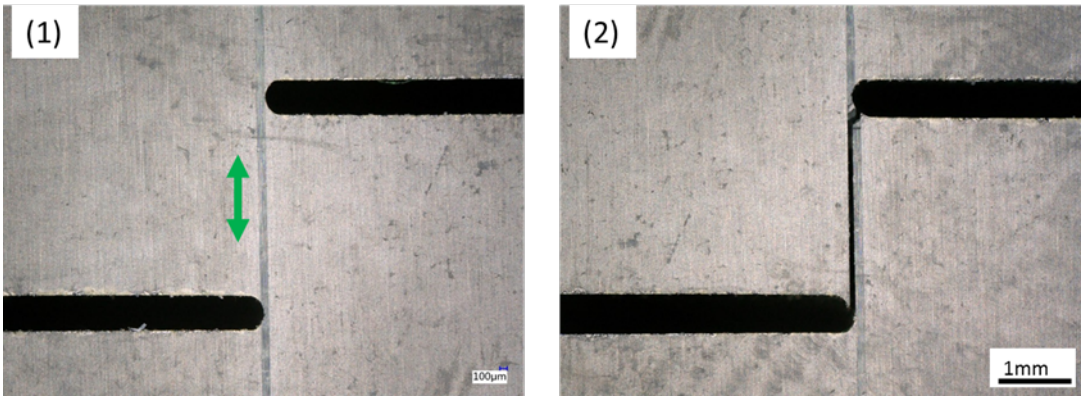

Figure 49 Optical microscopy images shown specimen 13453-42L before (1), and after (2) DNS test. Green arrow indicates the shear direction.

Specimens from 13453-47L showed an average shear strength of 58.9 MPa. Figure 50 shows optical microscopy images of a DNS specimen from 13453-47L before and after DNS test. The test was manually stopped after the initial load drop in order to observe the crack propagation. Several joint-layer through thickness cracks (light contrast areas in the joint layer) can be seen in Figure 50-(1) before the shear test. Post-test images indicate the through thickness defects such as existing cracks, started to propagate, within 20° parallel to the shear direction, into the CVD SiC substrate. This pattern suggests that the chemical bonding between the joint medium and the substrate is strong and the weakest link during the shear test is the existing through thickness cracks, to extend from the joint medium into the substrate.

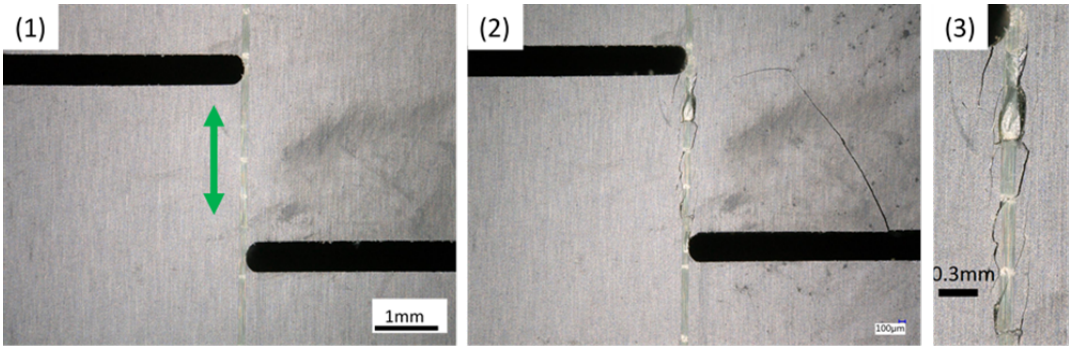

Figure 50 Optical microscopy images shown specimen 13453-47L before (1); and after (2), (3) DNS test. Green arrow indicates the shear direction

Sample plate 13453-56L uses the same process parameters as 13453-47L except the two-step sintering profile designed to mitigate macropore formation was used. Utilizing this 2-step sintering approach on the large sandwich joint resulted in a slightly lowered average apparent shear strength of 42.2 MPa (compared to 58.9 MPa for 1-step processing). The test crosshead was also manually stopped after the initial noticeable load drop for crack propagation observation. Images of a representative sample before and after the shear test are shown in Figure 51. A through thickness crack near one notch tip was

identified as the critical defect that is responsible for the failure of the specimen. This crack propagated horizontally (perpendicular to the shear direction) for a few microns, then it started to divert and propagated along a ~45° line to the shear direction into the CVD SiC substrate. The 45° angel corresponds to the virtual plane of the largest shear stress. The lower strength in the 13453-56L is attributed to the large joint thickness of ~150 µm. When the joint thickness is reduced in the small sandwich sample (13453-58S had joint thickness of 46 µm), the shear strength increased to 90 MPa. These factors must be considered when determining the processing parameters for a given joint application.

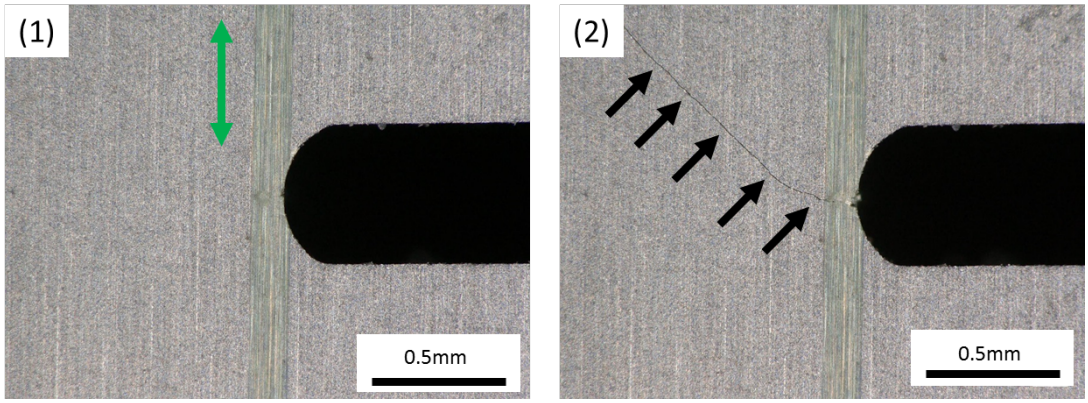

Figure 51 Optical microscopy images shown specimen from 13453-56L before (1), and after (2) DNS test. Green arrow indicates the shear direction and the black errors indicate the main failure crack

Images of sample 13453-59L before and after shear test are shown in Figure 52. The sample is joined using the lowest oxide content tape (TEP2) and showed an average shear strength of 49.8 MPa. Before the shear test, no large through thickness cracks are observed in the joint layer because its low oxide content results in similar coefficient of thermal expansion (CTE) values to the CVD SiC substrate. The fracture surface showed a partially adhesive type of failure at the joint interface with the substrate, indicating a lowered bonding strength between the medium and the substrate, which is also attributed to the low oxide content of the joint medium.

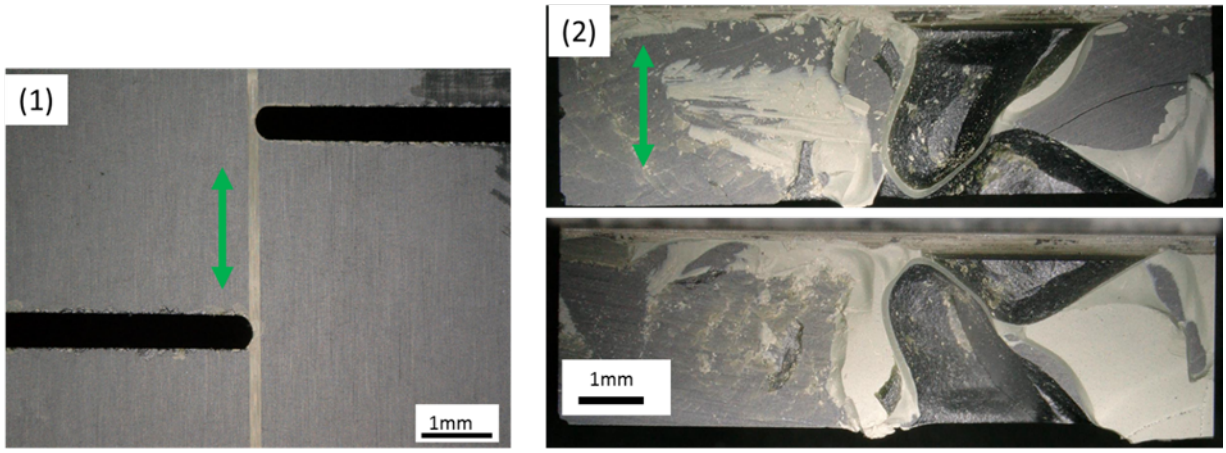

Figure 52 Optical microscopy images showing specimen from 13453-59L: (1) before test, and (2), the two fracture surfaces. Green arrow indicates the shear direction

3.4.7 TEP-based joint development summary

Joining SiC materials using the transient eutectic phase (TEP) route requires either high temperature or high oxide content in order to create strong bonding strength between the joint layer and the SiC substrate. However, the joining temperature is limited by the onset of substrate strength degradation. When TEP processed SiC-SiC composites are used as substrate, it is highly desirable to have joining temperatures at or below 1600°C in order to preserve the strength of the substrate during the joining process. 1600°C is relatively low for the TEP joining process so that higher oxide content formula (higher than TEP 2) is required to achieve a desirable bonding strength between the substrate and the joint layer. Meanwhile, higher oxide content of the joint medium also increases its CTE and hence enlarges the CTE mismatch between the substrate and the joint layer. This creates through-thickness cracks spanning the joint because of the residual tensile stress created in the joint layer. These through-thickness cracks are the strength-limiting factor for the two TEP3 samples 13453-47L & 56L. One solution for the CTE mismatch cracks problem is to reduce the thickness of the joint layer, as shown in the results in Table 3 and Table 6.

In this study, two methods have shown to be able to fabricate thin joints. The first method is one-step sintering, which results in in-situ slurry squeeze out at organic additive softening temperatures (~200°C) and thus achieving a thin joint. Results show the heterogeneous microstructures and large pores are associated with this method. However, the joints showed strong shear strength despite the non-ideal microstructure. The second method is the two-step sintering process with reduced joint layer thickness in the green state (sample 13453-58), which in turn results in a thin and impermeable final joint layer thickness and hence a strong joint.

Overall, a wide range of TEP joint process parameters have been investigated and correlation between the process parameters and joint properties has been established. The exact process parameters to be used depend on the requirement of specific systems. For example, when radiation resistance is not a major concern, higher oxide content formulas can be used. When hermeticity is not a critical issue, the one-step sintering profile can be used. TEP based joining offer a wide range of process conditions and can be used in various circumstances.

The joint development described above enables the fabrication of composite assemblies with enhanced complexity that will be required in advanced nuclear reactors. As an example, vented fuel designs in some advanced reactors required a fission product vent manifold to capture and transport fission products from individual fuel rods out to a central collection system. In EM^2, this component must be SiC-SiC to accommodate temperatures and neutron fluence during its lifetime. These joining techniques have been leveraged with the complex composite substructures described in sections 3.2 to build up multi-layer structures with embedded internal features to demonstrate one such embodiment of a vent manifold system.

A 101.6 mm diameter multi-layer vent manifold has been produced by leveraging the techniques demonstrated throughout this project. The joined assembly is comprised of 3 separate layers, each derived from a 101.6 mm diameter, 4 mm thick complex planar composite substructure. Each layer has a different thru-hole geometry such that, when joined, additional complex internal features are created. Additionally, the middle layer was sectioned from a circular disk into 6 pie-shaped sections. The eight planar SiC-SiC components were joined together to make a 3 layer joined manifold assembly that is approximately 102 mm in diameter and 12.5 mm thick (Figure 53). All 8 components were joined simultaneously in a single furnace run using process parameters tailored to preserve composite performance, and materials which have demonstrated stability in nuclear environments. The assembly

has two distinct fluid flow pathways. A set of 12 holes, each 5 mm in diameter pass through the entire thickness of the assembly. These features make up the coolant flow channels that will allow coolant to pass up the length of the core and through the manifold plate to the power conversion system. The other fluid flow pathway is completely isolated from the coolant. Seven holes, 20 mm in diameter, on one side of the assembly represent where fuel rods will attach to the manifold. These 7 holes mate to interconnected channels 6 mm in width and 4 mm in height, created by 6 equally spaced pie-shaped pieces of composite in the middle layer (Figure 53). In this way, fission gases generated will vent out of each individual fuel rod and pass into the interconnected network so that they can be captured in the collection system. Effective joining of the composite structures has led to the successful fabrication of a first of a kind SiC-SiC composite vent manifold assembly.

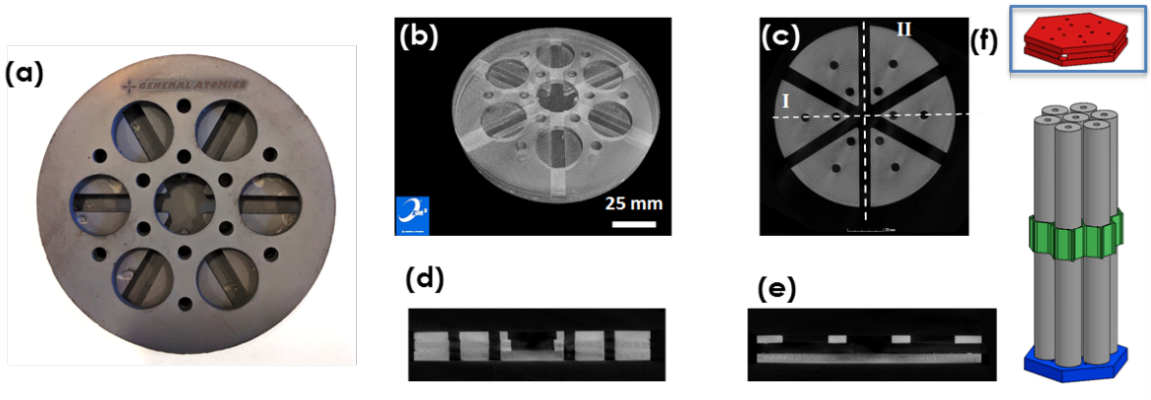

Figure 53. Image of joined multi-layer SiC-SiC composite vent manifold structure (a), Semi-transparent X-ray computed tomography (XCT) volume of the multi-layer vent manifold assembly showing internal channel network (b), with XCT slices of the middle layer of pie-shaped composite pieces that define the asterisk-shaped vent channels (c), cross sectional view indicated line I showing 4 coolant channels and the central fission gas channel in that plane (d), cross-sectional view indicated by line II, showing 3 fuel rod insertion points interconnected by fission gas channel (e), and rendering of miniature EM^2 hexagonal fuel bundle assembly showing vent manifold positioning in red (f).

3.5 Fabrication of SiC-SiC Composite Assemblies through Mechanically-enhanced Joining

The final task of this project developed techniques for attachment of multiple complex structures edge to edge. Since the surface area along the edges of the composite components fabricated in this project are small relative to the total surface area of the component, these edge joints are a potential weak point of the overall assembly integrity. The butt joint was successfully implemented to demonstrate multicomponent attachment schemes. However, as a risk mitigation strategy, the joint surface area was increased through geometric modification of the edge joint surface. In addition to simply butting multiple components up to one another and joining them, two separate mechanical enhancements were evaluated: (1) a triple butted lap or “tongue and groove” scheme, and (2) a triple scarf or “corrugated” scheme. The conclusion from this geometric evaluation led to final construction of a multi-component, multi-layered vent manifold assembly to demonstrate the potential scalability of complex SiC-SiC composite structure fabrication methods.

3.5.1 Evaluation of different mechanically-enhanced joint configurations

Alignment and load application are critical factors affecting joint integrity. Butt joints delivered good joint uniformity while maintaining substrate integrity. The tongue and groove and corrugated complex

joints resulted in substrate cracking or intermittent separation at the joint interface after processing. Despite substrate cracking, the interface of the corrugated joint appears to be uniform which is likely due to the configuration promoting pressure application across a large area of the available interface. Conversely, the tongue and groove joint shows large regions where no joint material is visible, as seen in Figure 54.

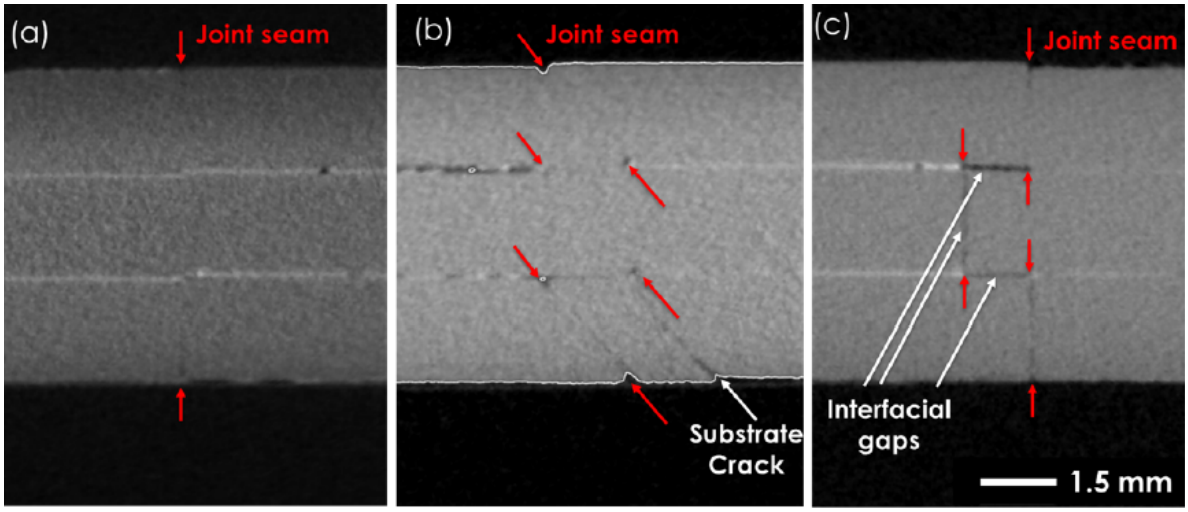

Figure 54. XCT slices showing the cross section of the different edge-to-edge joint geometries. Butt (a) and corrugated (b) joints show well mated interfaces, while tongue and groove (c) shows large regions along the interface where no joint material is present (black).

Mechanical testing was performed on each of the three edge joint geometries. Along with flexural testing, optical microscopy was used to associate and identify joint fracture surfaces to the different specimen types. These joint specimens were fabricated using a single step while the butt joint was fabricated using both a single and dual step sintering process as described in section 3.4. These results are summarized in Figure 55.

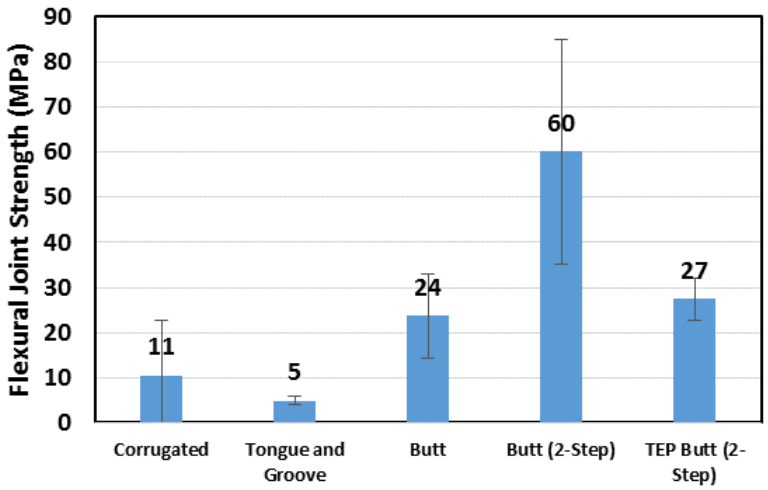

Figure 55. Summary of average joint strength for different joint geometries and process variations. Error bars are +/- one standard deviation.

Between all of the single step sintered joints, the butt joint exhibited more than twice the strength of the corrugated joint and nearly five times the strength of the tongue and groove joint. The complex geometries displayed weaker strengths overall and the fracture surface from both geometries showed little to no reaction on the joint interface. Islands of light green joint material on the surface indicates poor surface contact and little reactivity. In addition to poor interfacial contact, the specimens underwent substrate cracking during sintering which further compromised the flexural strength of the specimens by moving joint material away from the surface and towards the defects. Figure 56 shows the fracture surfaces and substrate features of a tongue and groove joint specimen.

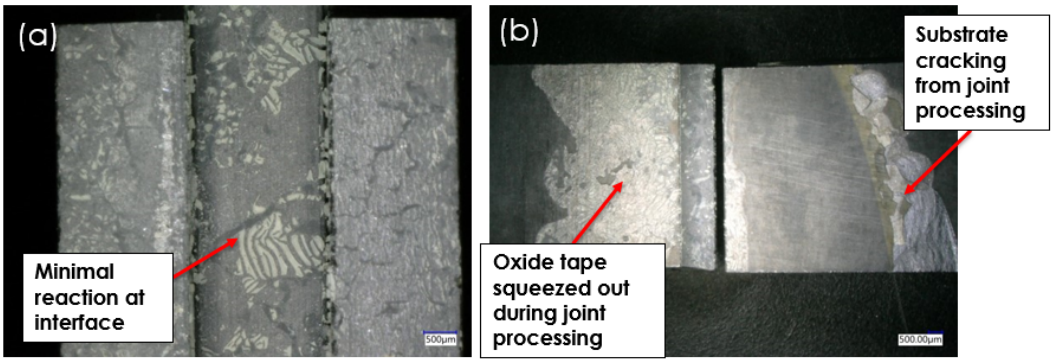

Figure 56. Optical microscopy shows tongue and groove specimen cross section (a), and side view (b) following flexural testing.

Among butt joint specimens, the transition from single step sintering to dual step sintering resulted in a nearly 250% increase in strength from 24 MPa to 60 MPa. The dual step sintering process prevents leakage of the joint material away from the interface during temperature ramp up due to the absence of binder material. As a result, oxide reaction occurs over a larger fraction of the joining surface and slight deviations across the interface are better accommodated by the thicker joint material. This improved interfacial reaction results in increased strength and a higher instance of substrate cracking rather than joint delamination during flexural testing. Figure 57 shows a comparison of the single and dual step butt joints which highlights the higher degree of reaction and substrate cracking in the dual step approach. It should be noted that dual step sintering was not employed on the complex geometries in this work. There is potential that a thicker joint interface could improve performance of the other two geometries but specimen damage induced during sintering is expected to persist due to stress concentrations arising from the intricate interfacial features.

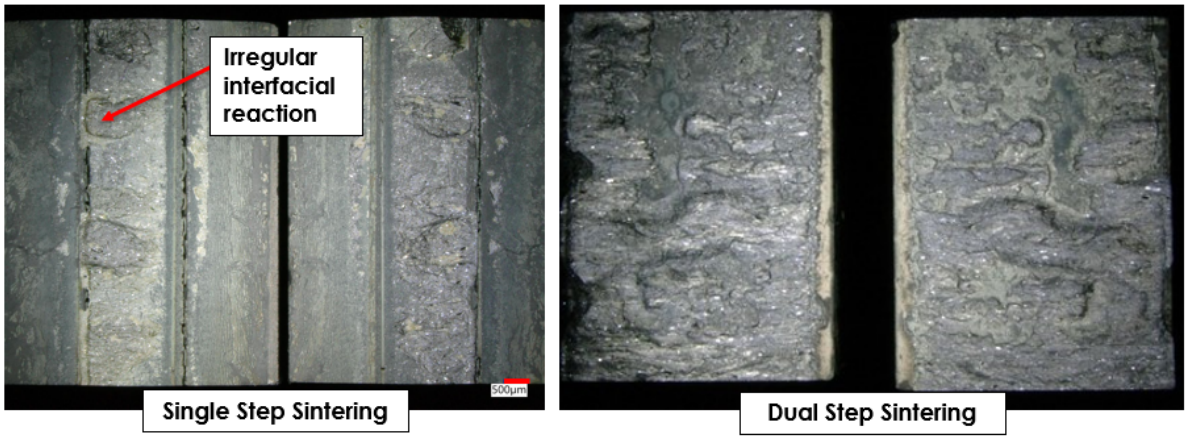

Figure 57. Optical micrograph comparing fracture surfaces following flexural testing of single and dual step sintered joints. The dual step sintering results in more uniform reaction across the joint, which results in high bond strengths.

An in-depth analysis of the butt joint geometry was also done to establish a more complete quantitative understanding of the performance. A total of 15 butt joint specimens were prepared and summarized in Appendix C.

Among the 15 specimens tested, 3 were deemed invalid due to defects in specimen preparation. Among the 12 valid tests, 10 were prepared from CVD silicon carbide (SiC) and 2 were prepared from TEP composite material (BJ-LS-14, 15). Notable within these results is that failure was observed in the substrate in all CVD SiC joint specimens but cohesive type failure was observed in the TEP specimen's joint layer. This disparity implies stronger reaction between the CVD SiC materials compared with the TEP composite substrates. The Weibull modulus and characteristic strength were calculated from the CVD SiC joint data in Figure 58.

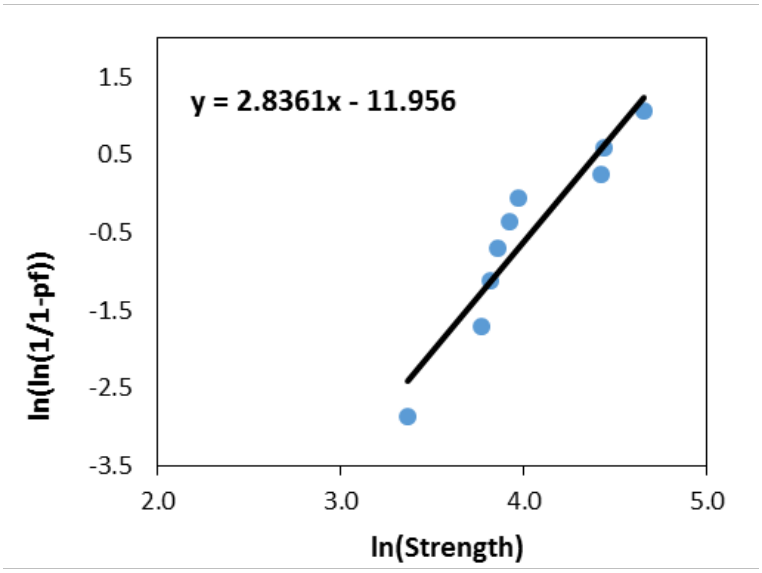

Figure 58. Weibull plot for flexural strength of CVD SiC butt joints.

The flexural strength of pure CVD SiC was approximately 240 MPa. When comparing the flexural strength of the joint material it is approximately 28% of the parent material. The Weibull modulus is also

low, at 2.83, which suggests a large distribution in strength. Even though the average strength has improved, the data indicates that additional process improvements are needed to ensure more uniform and complete reaction of the joint interface. Specimens BJ-LS-1 and 2 are good examples of the potential strength of these joints; these two specimens had flexural strength substantially higher than the others in this set (up to 105 MPa). Fractography of these specimens indicates substantially greater degrees of surface reaction and substrate fracture, shown in Figure 59. All 13 CVD SiC specimens underwent similar processing conditions which suggests variation arises from the quality of the interfacial reaction. Extremely flat surfaces are required to achieve uniform contact during high temperature processing and to ensure greater joint strength.

Figure 59. Optical micrograph of fracture in specimen BJ-LS-2 showing significant substrate fracture along entire surface.

The lower strength observed in the TEP composites was also investigated further using optical microscopy. Upon closer inspection, there is a preferential migration of joint material into the fibrous portions at the joint interface in the composite, whereas the CVD SiC butt joints have more uniform material distribution. This preferential distribution occurs due to the increased surface area in the fibrous regions which draws the joint material away from the planar surface during processing. The preferential oxide migration is visible in Figure 60.

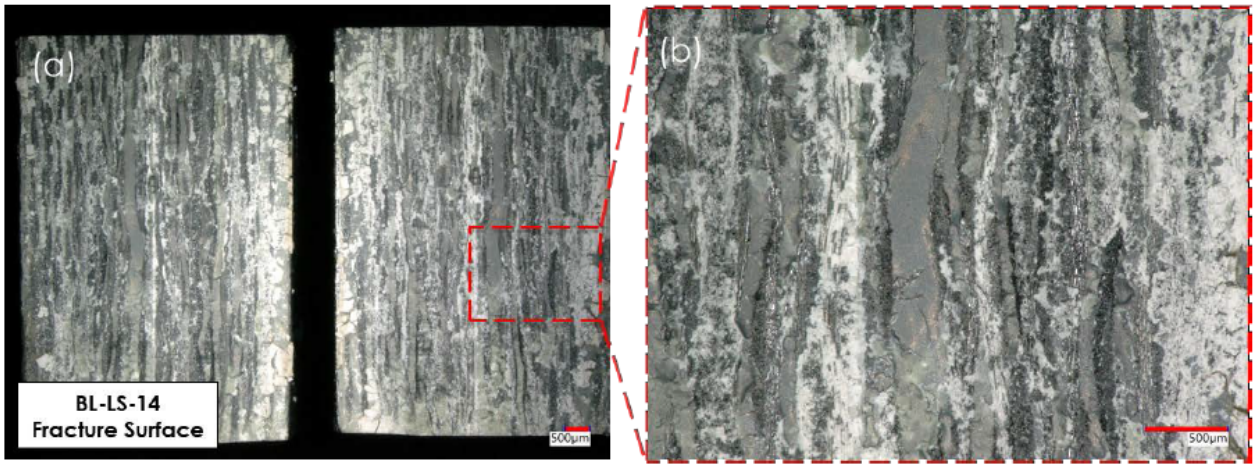

Figure 60. Low magnification image of fracture surface in TEP composite butt joint specimen (a), and high magnification image showing smooth, unreacted gray regions of matrix, adjacent to white, oxide rich regions where joint material has accumulated within fibrous regions.

The TEP composite joint showed little reaction in the matrix of the joint interface and a large accumulation of oxides on the fibers. Future work must be conducted to overcome this issue. Potential avenues to elucidate the origin of this phenomenon include systematic studies of oxide fraction in both the joint and composite matrix precursor.

3.5.2 Fabrication of multi-component vent manifold assembly

The specimen GA-JMCCS-D4 represents the potential for scalability of complex SiC-SiC composite structures. In the specimen shown in Figure 61, TEP joining technology was expanded to fabricate a multi-component assembly. Four multi-layer SiC-SiC subassemblies were joined edge-to-edge to create a single, large, complex assembly. As part of this work, different edge joint geometries such as scarf and butted lap features were evaluated to potentially strengthen these edge joints, but a simple butt joint has so far provided the best joint integrity as seen in section 3.5.1. The edge joining provides a pathway to create larger structures where single component construction is not feasible. The ability to join SiC-SiC composites enables the fabrication of large, complex structures required for advanced nuclear reactors. Vented fuel designs in some advanced reactors require a fission product vent manifold to capture and transport fission products from individual fuel rods out to a central collection system.

The specimen GA-JMCCS-D4 is a scaled version of what one such vent manifold assembly may look like. Each of the four multi-layer sub-assemblies consists of 6 planar composite components containing one or multiple thru-hole features. Multiple multi-layer subassemblies can be joined in a single furnace run. Each subassembly represents a vent manifold pathway for a single fuel rod. The four subassemblies were subsequently joined together to create a robust, hermetic, vent manifold assembly approximately 65.7 mm x 65.4 mm x 7.0 mm. The surface preparation and tooling used during the edge joining resulted in excellent alignment of the four subassemblies, as evidenced by the seamless intersection at the junction between the four subassemblies Figure 61. The alignment of the components is imperative for reliable joining of the components because gaps at the interface will degrade joint performance. As seen in section 3.5.1, the butt joint geometry offered the highest flexural strength with the dual sintering process. More complex edge joint features were not conducive to achieving this same level of interfacial alignment and

strength. It is for this reason that the butt joint was deemed the best option for edge joining in complex assembly fabrication.

The assembly has two distinct fluid flow pathways. A set of 16 holes, each 6.5 mm in diameter pass through the entire thickness of the assembly. These features make up the coolant flow channels that will allow coolant to pass up the length of core and through the manifold plate to the power conversion system. The other fluid flow pathway is completely isolated from the coolant. Four holes, 6.5 mm in diameter on one side of the assembly represent where fuel rods will attach to the manifold. These four holes mate to interconnected channels 6 mm in width and 2.5 mm in height, created by 16 equally spaced pieces of composite in the middle layer. In this way, fission gases generated will vent out of each individual fuel rod and pass into the interconnected network so that they can be captured in the collection system. While the overall dimensions of this assembly are smaller than previous single components fabricated during this program, the successful implementation of edge joining enables additional versatility in the size and complexity of SiC-SiC composites that can be produced. Figure 62 gives a schematic representation of the complete miniature fuel bundle assembly that can now be produced based on the progress in composite fabrication and joining demonstrated in this contract. Each of the main components in the assembly was successfully fabricated during the period of performance, and all of the techniques used are easily scalable to produce these parts in the dimensions required for deployment in EM^2 or other advanced high temperature reactor designs.

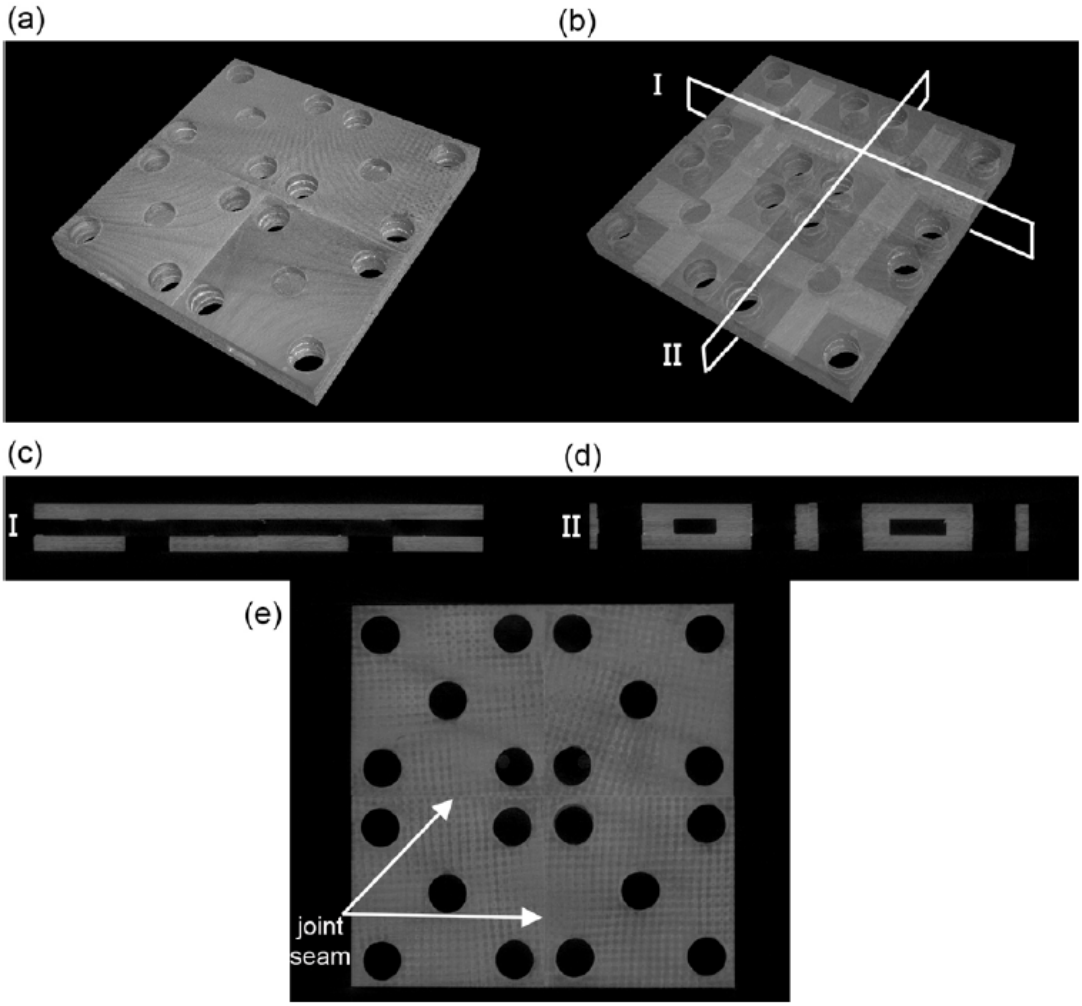

Figure 61. X-ray computed tomography (XCT) volume of edge-joined, multi-component vent manifold assembly, GA-JMCCS-D4 (a), with semi-transparent XCT volume showing internal vent channel structure (b), cross-sectional view indicated by line I showing two fuel rod insertion points interconnected by the fission gas channel (c), cross-sectional view indicated by line II, showing four coolant channels and two central fission gas channels (d), and 2-D XCT slice showing alignment of the four components and defect free join seam (e)

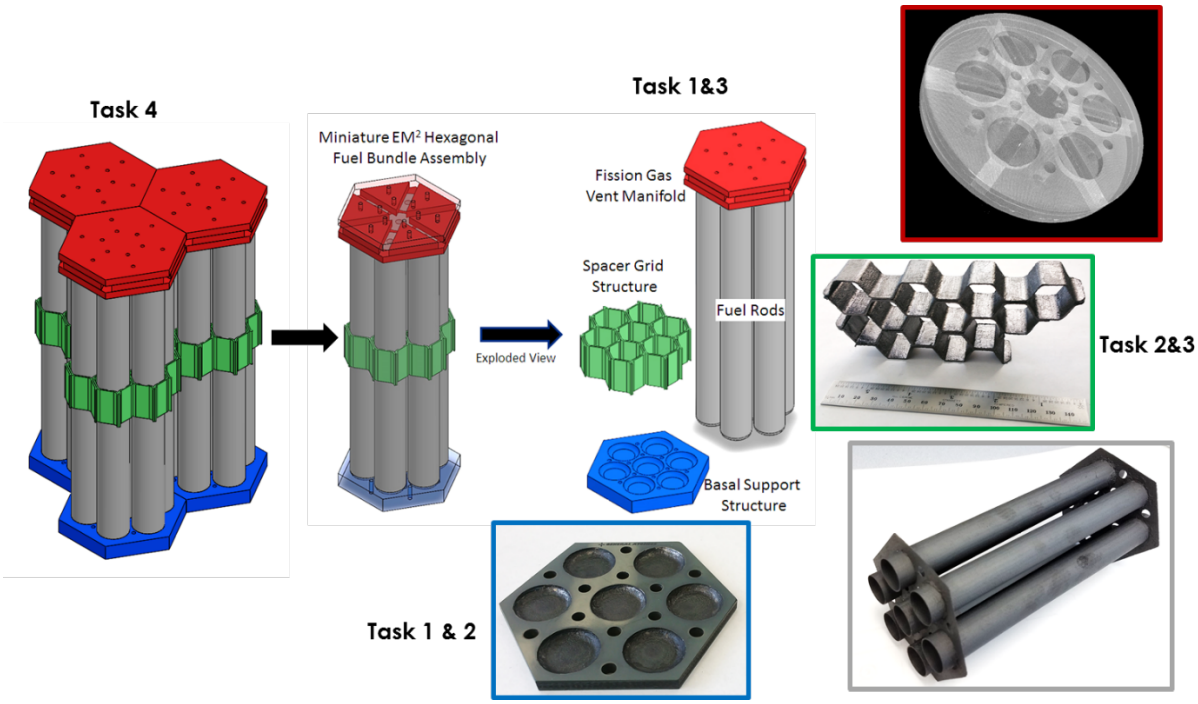

Figure 62. Schematic representation of how the components successfully produced as part of this project can be deployed to produce a miniature EM² tri-bundle assembly.

4. Products Developed/Technology Transfer

4.1. Conferences

H.E. Khalifa, C.P. Shih, G.M. Jacobsen, C.P. Deck, "Fabrication and Characterization of Complex SiC/SiC Composite Structures," Poster Presentation at Nuclear Fuels and Structural Materials Topical Meeting within the American Nuclear Society 2016 Summer Meeting, 6/15/16, New Orleans, LA.

H.E. Khalifa, C.P. Shih, C.P. Deck, O. Graeve, E. Novitskaya, X. Huang, L. Alva, H. Zhou, D. McCleeary, "Modular Fabrication and Characterization of Complex Silicon Carbide Composite Structures," Presented at the Annual Advanced Reactor Technologies, Advanced Reactors and Methods Meeting at Argonne National Lab, 11/18/16, Lemont, IL.

H.E. Khalifa, C.P. Shih, C.P. Deck, O. Graeve, E. Novitskaya, X. Huang, L. Alva, H. Zhou, D. McCleeary, "Modular Fabrication and Characterization of Complex Silicon Carbide Composite Structures," Presented at the 41st Annual International Conference of Advanced Ceramics and Composites, 1/25/17, Daytona Beach, FL.

C.P. Shih, H.E. Khalifa, G.M. Jacobsen, C.P. Deck, "Strength Retention and Microstructure Evolution of SiC/SiC Composites Following Heat Treatment in Argon up to 1800°C," Presented at the 41st Annual International Conference of Advanced Ceramics and Composites, 1/26/17, Daytona Beach, FL.

D. McCleeary , X. Huang, H. Khalifa, H. Zhou, L. Alva, J. Clifford, P, Majumdar, "Damage Tolerance of SiC_f-SiC_m Composite Plates Under Low Velocity Impact," Presented at the 41st Annual International Conference of Advanced Ceramics and Composites, 1/26/17, Daytona Beach, FL.

4.2. Papers

Both collaborating universities are preparing manuscripts based on the characterization performed in this work. Contributors from UCSD are preparing a manuscript on structure-property relationships that will include extensive analysis of composite structure using the electron microscopy and microhardness data acquired. Contributors from USC are preparing a manuscript on the evaluation and quantification of accumulated damage in SiC-SiC composites through the use of impulse excitation and drop weight impact tests. The journals to which these manuscripts will be submitted have not yet been determined. DOE will be notified once these manuscripts are ready for submission.

4.3. Collaborations Fostered

Through the course of this project strong working relationships were developed between General Atomics and each of the collaborating universities. GA has continued working with Xinyu Huang's group at USC through the DOE's Accident Tolerant Fuels program, where Dr. Huang's expertise in complex mechanical testing and analysis will continue to facilitate a deeper understanding of how SiC-SiC composite will perform in nuclear systems. GA also remains actively engaged with Olivia Graeve's group at UCSD in both materials synthesis and characterization. Dr. Graeve is affiliated with The CaliBaja Center for Resilient Materials and Systems and GA intends to remain an active partner with this center. A particular area of interest is rapid consolidation techniques for high temperature ceramics.

5. Computer Modelling

5.1. Heat transfer modeling in COMSOL

A 3D finite element model (FEM) of the TEP process was implemented for a two hole SiC plate consolidation described in section 3.2 using COMSOL. The objective of this task was to elucidate potential variations in temperature across the part during processing that may coincide with variations observed in the as-fabricated specimen. A number of initial assumptions were made to define the boundary conditions. The SiC plate is assumed to be monolithic such that isotropic properties can be used. Subsequent iterations may take into account anisotropic effects of fiber reinforcement. For both SiC and the graphite tooling, the thermal expansion coefficient, emissivity and thermal conductivity are temperature dependent and taken from literature [11] [12]. Heat transfer occurred by surface-to-surface radiation from furnace heater to the tooling, and by combined radiation, conduction and convection between interfacing graphite tooling parts and the SiC part itself. Translation and fixturing conditions were imposed to allow displacement from one side as is the case in the experimental set up.

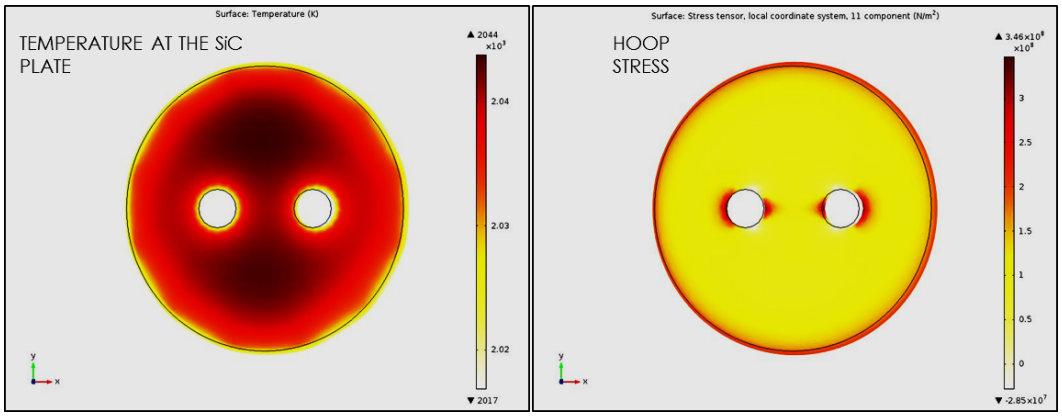

Figure 63. Results of TEP consolidation FEM. Temperature (left) and hoop stress (right) maps of a monolithic TEP disk with 2 holes at end of high temperature processing.

Axial and radial temperature gradients and differential CTE between SiC and graphite give rise to some variations in observed temperature and stress distribution in the SiC part. The SiC plate loses heat to the adjacent graphite material defining the internal hole features as well as the external diameter. The affected zone is constrained to approximately 0.5 mm and extends radially from the graphite surface. The affected zone depicted in the model is in good agreement with experimentally fabricated monolithic SiC plates shown above in Figure 9. A hoop stress biased in the x-direction arises around the 2 internal hole features. The graphite rods defining the holes are fixed in position by an additional graphite tooling component, and higher CTE in the SiC part in this temperature regime causes the SiC to grow more rapidly. Thus, the hole spacing between the constrained graphite tooling and the SiC part are different leading to generation of the hoop stress. Modelling results are shown in Figure 63

Additionally, heat transfer modeling was conducted on the hexagonal strip consolidation described in Section 3.3. In the model, the specimen is compressed between two graphite blocks (top tooling and bottom tooling) with 20 MPa applied pressure. The sample is modeled inside a furnace and heated at the temperature of 2200 K. The main forms of heat transfer are radiation and conduction. A small flux of heat is transmitted to the ambient through the graphite tools. The displacement of a few points of the furnace-tooling-specimen assembly was constrained in order to provide the boundary conditions necessary for the program to find the solution. In Figure 64 the Von Mises stresses and the pressure on the surface of the specimen are shown. The Von Mises stresses reveals the areas with stress concentrations and the distribution of pressure on the surface of the specimen can be used to analyze the effectiveness of the compression. The non-planar geometry creates a mixed stress state in the part where both tension and compression exist. Furthermore, the magnitude of the tensile stresses peak at 55 MPa while the compressive stresses reach up to 110 MPa, significantly higher than the applied pressure. The model was be used to determine the threshold process pressure to apply such that the pressure at the surface stays closer to the target 20 MPa. The temperature profile was also calculated from the model, but showed variation of less than 20 K across the entire 25 x 150 mm part.

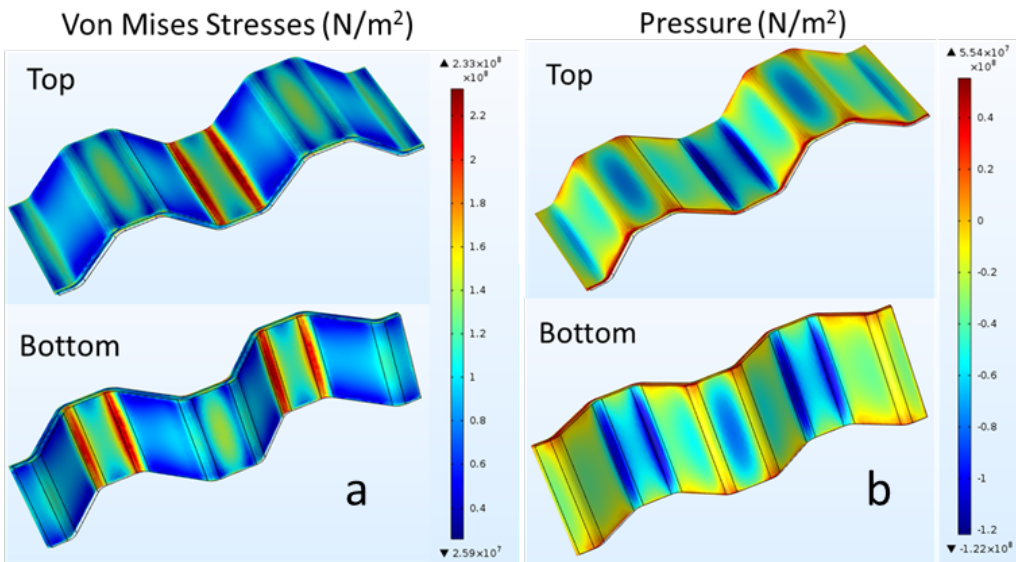

Figure 64. Calculated FEM results of hexagonal strip consolidation showing von Mises stresses (a) and resultant pressure on the specimen surface (b) for top and bottom faces of specimen

5.2. *Dynamic Impact Modeling in LS-DYNA*

A Finite element model was built in LS-DYNA to understand the damage in the SiC-SiC ceramic composite. LS-DYNA is efficient in multi-physics simulation with explicit time integration to solve nonlinear dynamic problems. Various material models and element types were implemented to capture the damage behavior, such as the damage shape, the impact force profile, and the absorbed energy during the impact. The ultimate goal is to build a predictive model that able to simulate the complex damage behavior of the SiC-SiC ceramic composite during a low velocity impact event.

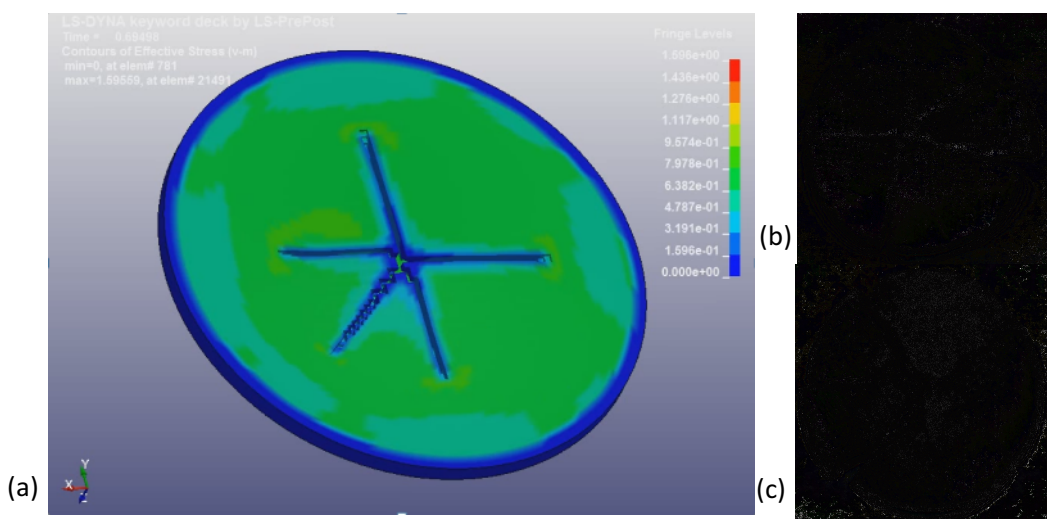

Figure 65 FE simulation of the radial damage from a 40 mm drop test. LS-DYNA MAT110 material and solid element are used to build the disk. In (a) 0, 45, and 90 degree radial cracks are predicted by the model, which are similar to the cracks observed in the experiment, as shown in (c) the impact surface and (d) the free surface of the disk after burst test.

Based on the TEP ceramic composite propertied obtained from experiment, we first built a simplified model with solid elements. The disk is constructed by MAT110 Johnson-Holmquist model ceramic

material, and solid brick elements with 5 nodes in the thickness direction. With the multiple layers of brick elements, it's possible to simulate damages developed between the top and bottom surface. The simulation result from a 40-mm drop test is shown in Figure 65(a). The cracks developed in the radial directions are distinctively similar to that observed in experimental results shown in Figure 65(b) and Figure 65(c). It is particularly interesting to notice the 45 degree crack shown in the simulation, which is also noticed in the experimental result.

Another important aspect of the simulation is to capture the force and energy of the impact event. In Figure 66(a) and Figure 66 (b), the simulation results from a 20-mm drop test is shown. The experimental result is shown in Figure 66(c). It can be identified that the shape of both the force and energy history are similar to the experimental results. Particularly in the force curve, the secondary peak (the "shoulder") after the initial impact force peak is associated with the damage developed in the specimen was successfully captured by the simulation.

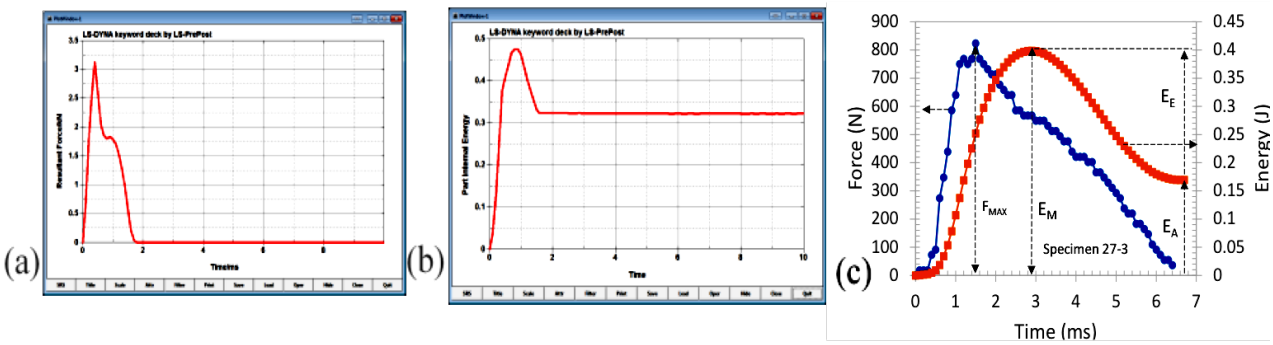

Figure 66.Impact force and energy simulation result of a 20 mm drop test from the FE model (a) the contact force and (b) the kinetic energy of the impactor are similar to the experimental result shown in (c). The shoulder in the force plot is associated with the damage developed in the specimen.

The drawback of the solid model is that it cannot fully represent the composite nature of the specimen. During experimental study, delamination, fiber kinking were observed in the sample, which are important to the damage model of the composite material. This explains the discrepancy between the simulation and experimental results in the force curve. In the experiment, the shoulder is much wider than that in the simulation. We believe this is due to the softening of the material caused by the evolving hierarchical damage in the composite layers. It is impossible to model these damage features with the solid element.

To improve the simulation, layered shell element model is under development to model the interleaving monolithic SiC layers and woven SiC composite layers. As shown in Figure 67, a 5-layer composite sample is constructed with shell elements. The LS-DYNA provides a model of multi-layer element where the material, the thickness, and fiber orientation can be individually assigned. Inter-layer and intra-layer damage can be identified in each layer.

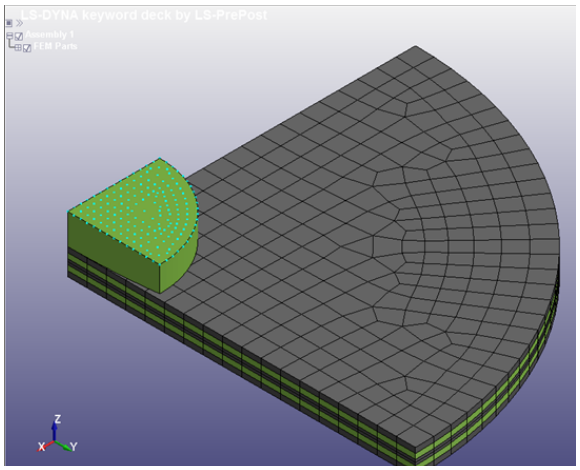

Figure 67. Layered shell element is implemented to model a 5-layer TEP-SiC composite. The disk sample is constructed by 5 layers of shell elements, different materials and thickness can be applied to individual layers.

This is a work in progress. After testing the layered shell element model is finished, we will compare the simulation results with experimental data to evaluate its capability in simulating composite delamination. In future work, we will also systematically study and implement other composite material and element models provided in LS-DYNA to improve our model towards a practical predictive tool for the low velocity impact behavior of SiC-SiC ceramic composite materials.

6. Participants and Other Collaborating Organizations

Institution: University of California – San Diego

Personnel and work summary: The PI for UCSD's effort is Professor Olivia Graeve. Her postdoctoral fellow Ekaterina Novitskaya conducted the research under Dr. Graeve's guidance. Dr. Novitskaya performed initial XRD-based residual strain measurements and guided the analysis towards the alternative route of microhardness based assessment of local property variation. She performed all microhardness measurements and performed analyses to draw effective conclusions on the role played by processing and geometry on local property variation. Dr. Novitskaya also performed all scanning and electron microscopy work on bulk composite and joint specimens included selected area diffraction and phase identification in the complex reaction zone of the joint interface.

Institution: University of South Carolina

Personnel and work summary: The PI for USC's effort is Professor Xinyu Huang. Other participants included, postdoctoral fellows Dr. Hongying Zhao, Dr. Jingjing Bao, PhD candidate Luis Alva and Undergraduate research assistants Cole Jackson, William Housley, and Donald McCleary (now, MS candidate). Dr. Zhao, assisted by Cole Jackson and William Housley, led the design and implementation effort of mechanical experiments to measure the strength and the facture toughness of SiC composites. Due to personal health issues, Dr. Zhao left the project in 2016. Mr. Jackson and Mr. Housley left the project after their graduation in 2016. Dr. Bao later participated in the project and contributed towards both experimental and finite element modeling effort. Mr. Luis Alva, Dr. Bao, and Mr. Donald McCleary were mainly responsible for the impact testing, the finite element modeling work of SiC composite plates, and the associated NDE study based on impulse excitation (IE) technique. Luis Alva carried out most of the microstructure characterization work.

References

[1] T. Koyanagi, K. Ozawa, T. Hinoki, K. Shimoda and Y. Katoh, "Effects of neutron irradiation on mechanical properties of silicon carbide composites fabricated by nano-infiltration and transient eutectic-phase process," *Journal of Nuclear Materials,* vol. 448, pp. 478-486, 2014.

[2] K. Shimoda, "Influence of pyrolytic carbon inteface thickness on microstructure and mechancial properties of SiC/SiC composites by NITE process," *Composites and Science Technology,* vol. 68, pp. 98-105, 2008.

[3] Zhao, "LS DYNA Applications in Simulating Impact Test of Nuclear Fuel Spacer Grids and Drop Tests of Fuel Shipping Packages," 2012.

[4] Song, "Non-linear FE analysis on Static Buckling Behabior of the Spacer Grid Structure," KAERI, 2000.

[5] Yoon, "Dynamic Impact analysis of the gris structure using multipoint constraint equation under the lateral impact load," *Computers and Structures,* vol. 82, pp. 2221-2228, 2004.

[6] Y. Katoh, L. Snead, T. Cheng, C. Shih, W. Lewis, T. Koyanagi, T. Hinoki, C. Henager and M. Ferraris, "Radiation-tolerant Joining Technologies for Silicon Carbide Ceramics and Composites," *Journal of Nuclear Materials,* vol. 448, pp. 497-511, 2014.

[7] Y. Katoh, K. Ozawa, C. Shih, T. Nozawa, R. Shinavski, A. Hasegawa and L. Snead, "Continuous SiC fiber, CVI matrix composites for nuclear applications; Properties and irradiation effects," *Journal of Nuclear Materials,* vol. 448, pp. 448-476, 2014.

[8] T. L. M. H. M. M. W. L. H. S. S. Ahmad, "Phase Evaluation During High Temperature Long Heat Treatments in the Y2)3-Al2O3-SiO2 system," *J. Euro. Ceram. Soc.,* vol. 34, pp. 3835-3840, 2014.

[9] H. Khalifa, C. Deck and C. Back, "High Durability Joints between Ceramic Articles and Methods of Making and Using Same". Unites States Patent US9132619 B2, 2015.

[10] M. Ferraris, "Effects of neutron irradiation on glass ceramics as pressure-less joining materials for SiC based components for nuclear applications," *Journal of Nuclear Materials,* vol. 429, pp. 166-172, 2012.

[11] L. Snead, "Handbook of SiC Properties for fuel performance modeling," *Journal of Nuclear Materials,* pp. 329-377, 2007.

[12] Uher, "Temperature dependence of thermal conductivity of graphite," in *Landolt-Bornstein - Group III Condensed Matter*, vol. 15c, W. Madelung, Ed., Berlin, Springer, 1991, pp. 430-439.

Appendix A – Specimen Fabrication History

Specimen Type Key	
BD	Blank disk
2H/4H/5H/7H/19H	2/7/19 hole plate
MM	Multilayer manifold assembly made from 4H/5H plates
4X	Edge to edge joined vent manifold assembly, 4 total, 80mm x 80mm
TC	Thick Composite
BDwCC	Blank disk with 12 coolant channels
7H HX	7 hole plate cut into a hexagon
7D	Plate with 7 25mm diameter 3mm deep blind holes
7HwCC	Plate with 7 25mm diameter holes and 12 coolant channels
7DwCC	Plate with 7 25mm diameter dimples and 12 coolant channels
PC	"Potato chip" curved plate
SW	"Sine wave" curved plate
HX	Hexagonal strip, 150mm x 25mm
MLJ	Multilayer joint subcomponent
BJ	Edge to edge butt joint
CG	Edge to edge "corrugated" joint
T&G	Edge to edge "tongue and groove" joint

Specimen	Year/Quarter	Specimen Type	Fiber Vol. Fraction (%)	Dimensions (mm)	Rel. Density (%)
130424-5-1	2015, Q1	BD	12%	51.5	89%
130424-6-1	2015, Q1	BD	12%	51.5	85%
130424-7-1	2015, Q1	BD	0%	76.2	85%
130424-8-1	2015, Q1	BD	6%	76.2	N/A
130424-9-1	2015, Q1	BD	6%	51.5	86%
130424-9-2	2015, Q1	BD	0%	51.5	92%
130424-10-1	2015, Q1	BD	6%	76.2	N/A
130424-11-1	2015, Q1	BD	0%	51.5	91%
130424-12-1	2015, Q1	BD	0%	51.5	90%
130424-13-1	2015, Q1	BD	12%	51.5	79%
130424-14-1	2015, Q1	BD	0%	51.5	90%
130424-15-1	2015, Q1	BD	0%	51.5	95%
130424-15-2	2015, Q1	BD	6%	51.5	89%

Specimen	Year/Quarter	Specimen Type	Fiber Vol. Fraction (%)	Dimensions (mm)	Rel. Density (%)
130424-16-1	2015, Q1	BD	0%	51.5	95%
130424-16-2	2015, Q1	BD	0%	51.5	94%
130424-16-3	2015, Q1	BD	6%	51.5	91%
130424-17-1	2015, Q1	BD	6%	51.5	93%
130424-17-2	2015, Q1	BD	6%	51.5	92%
130424-17-3	2015, Q1	BD	6%	51.5	89%
130424-18-1	2015, Q1	BD	24%	51.5	91%
130424-18-2	2015, Q1	BD	6%	51.5	92%
130423-17-1	2015, Q1	BD	48%	76.2	N/A
130423-19-1	2015, Q1	BD	52%	76.2	N/A
130424-19-1	2015, Q1	BD	0%	76.2	97%
130424-20-1	2015, Q1	BD	0%	48	96%
130424-21-1	2015, Q1	BD	0%	48	97%
130424-21-2	2015, Q1	BD	6%	48	96%
130424-22-1	2015, Q1	BD	6%	48	91%
130424-23-1	2015, Q1	BD	36%	48	84%
130424-24-1	2015, Q1	BD	36%	48	82%
130424-25-1	2015, Q1	BD	12%	48	80%
130424-26-1	2015, Q2	BD	24%	48	82%
130424-27-1	2015, Q2	BD	12%	48	88%
130424-28-1	2015, Q2	BD	24%	48	88%
130424-28-2	2015, Q2	BD	36%	48	89%
130424-29-1	2015, Q2	BD	12%	48	84%
130424-30-1	2015, Q2	BD	12%	48	82%
130424-30-2	2015, Q2	BD	24%	48	82%
130424-31-1	2015, Q2	BD	12%	48	N/A
130424-32-1	2015, Q2	BD	12%	48	N/A
130424-33-1	2015, Q2	BD	0%	48	78%
130424-34-1	2015, Q2	BD	12%	48	80%
130424-34-2	2015, Q2	BD	24%	48	83%
130424-34-3	2015, Q2	BD	36%	48	71%
130424-35-1	2015, Q2	BD	0%	48	91%
130424-36-1	2015, Q2	BD	12%	48	83%

Specimen	Year/Quarter	Specimen Type	Fiber Vol. Fraction (%)	Dimensions (mm)	Rel. Density (%)
130424-37-1	2015, Q2	BD	12%	48	84%
130424-38-1	2015, Q2	BD	12%	48	87%
130424-39-1	2015, Q2	2H	0%	48	88%
130424-40-1	2015, Q2	BD	12%	48	83%
130424-41-1	2015, Q2	BD	12%	48	85%
130424-42-1	2015, Q2	BD	12%	51.35	82%
130424-43-1	2015, Q2	2H	6%	48	94%
130424-44-1	2015, Q2	BD	12%	51.2	81%
130424-45-1	2015, Q2	BD	12%	48	80%
130424-46-1	2015, Q2	BD	12%	48	89%
130424-47-1	2015, Q2	BD	36%	48	85%
130424-48-1	2015, Q2	BD	12%	48	80%
130424-49-1	2015, Q2	BD	12%	48	83%
134024-49-2	2015, Q2	BD	24%	48	87%
130424-49-3	2015, Q2	BD	36%	48	88%
134024-50-1	2015, Q2	BD	36%	48	87%
130424-51-1	2015, Q2	2H	24%	48	85%
130424-51-2	2015, Q2	2H	24%	48	84%
130424-52-1	2015, Q2	BD	0%	48	91%
130424-53-1	2015, Q2	BD	12%	48	92%
130424-54-1	2015, Q2	2H	24%	48	83%
130424-54-2	2015, Q2	BD	24%	48	N/A
130424-55-1	2015, Q2	BD	36%	48	83%
130424-56-1	2015, Q2	BD	36%	48	91%
130424-56-2	2015, Q2	BD	0%	48	91%
130424-57-1	2015, Q2	2H	24%	48	88%
130424-58-1	2015, Q2	2H	24%	48	84%
130424-58-2	2015, Q2	2H	24%	48	80%
130424-59-1	2015, Q2	BD	36%	48	84%
130424-60-1	2015, Q2	BD	36%	48	86%
130424-61-1	2015, Q2	BD	36%	48	84%
130424-61-2	2015, Q2	BD	36%	48	88%
130424-62-1	2015, Q2	2H	24%	48	88%

Specimen	Year/Quarter	Specimen Type	Fiber Vol. Fraction (%)	Dimensions (mm)	Rel. Density (%)
130424-62-2	2015, Q2	2H	24%	48	89%
130424-63-1	2015, Q2	BD	0%	48	89%
130424-64-1	2015, Q2	2H	24%	48	87%
130424-64-2	2015, Q2	2H	24%	48	87%
130424-65-1	2015, Q2	BD	36%	48	85%
130424-65-2	2015, Q2	BD	36%	48	84%
130424-66-1	2015, Q2	BD	36%	48	85%
130424-67-1	2015, Q2	2H	24%	48	82%
130424-68-1	2015, Q2	BD	36%	48	87%
130424-69-1	2015, Q2	7H	0%	48	94%
130424-70-1	2015, Q2	BD	36%	48	91%
130424-70-2	2015, Q2	BD	36%	48	90%
130424-71-1	2015, Q2	2H	24%	48	84%
130424-71-2	2015, Q2	2H	24%	48	84%
130424-71-3	2015, Q2	2H	24%	48	83%
130424-72-1	2015, Q2	BD	36%	48	90%
130424-72-2	2015, Q2	BD	24%	48	82%
130424-72-3	2015, Q2	BD	36%	48	80%
130424-73-1	2015, Q2	BD	0%	48	90%
130424-73-2	2015, Q2	7H	0%	48	88%
130424-74-1	2015, Q2	2H	36%	48	84%
130424-74-2	2015, Q2	2H	24%	48	86%
130424-74-3	2015, Q2	BD	36%	48	85%
130424-75-1	2015, Q2	7H	24%	48	80%
130424-75-2	2015, Q2	BD	36%	48	84%
130424-75-3	2015, Q2	BD	36%	48	85%
130424-76-1	2015, Q2	BD	36%	76.2	82%
130424-76-2	2015, Q2	BD	36%	76.2	82%
130424-77-1	2015, Q2	2H	24%	48	83%
130424-77-2	2015, Q2	2H	24%	48	83%
130424-78-1	2015, Q2	2H	24%	48	87%
130424-78-2	2015, Q2	2H	24%	48	85%
130424-78-3	2015, Q2	BD	0%	48	N/A

Specimen	Year/Quarter	Specimen Type	Fiber Vol. Fraction (%)	Dimensions (mm)	Rel. Density (%)
130424-79-1	2015, Q2	BD	36%	76.2	85%
130424-80-1	2015, Q2	7H	36%	48	79%
130424-80-2	2015, Q2	BD	36%	48	88%
130424-81-1	2015, Q2	2H	24%	48	85%
130424-81-2	2015, Q2	2H	24%	48	81%
130424-82-1	2015, Q3	7H	36%	48	78%
130424-83-1	2015, Q3	BD	36%	76.2	84%
130424-84-1	2015, Q3	BD	36%	48	81%
130424-85-1	2015, Q3	BD	48%	48	81%
130424-86-1	2015, Q3	BD	36%	48	87%
130424-86-2	2015, Q3	BD	48%	48	86%
130424-87-1	2015, Q3	7H	48%	48	82%
130424-88-1	2015, Q3	BD	48%	48	89%
130424-89-1	2015, Q3	BD	48%	48	84%
130424-90-1	2015, Q3	BD	36%	48	86%
130424-90-2	2015, Q3	BD	48%	48	89%
130424-91-1	2015, Q3	2H	48%	48	87%
130424-91-2	2015, Q3	2H	48%	48	85%
130424-92-1	2015, Q3	2H	36%	48	87%
130424-92-2	2015, Q3	2H	36%	48	86%
13420-3-1	2015, Q3	2H	36%	48	83%
13420-3-2	2015, Q3	2H	48%	48	82%
13420-4-1	2015, Q3	BD	48%	76.2	81%
13420-5-1	2015, Q3	2H	36%	48	80%
13420-5-2	2015, Q3	2H	36%	48	83%
13420-5-3	2015, Q3	2H	48%	48	82%
13420-6-1	2015, Q3	7H	36%	48	77%
13420-7-1	2015, Q3	2H	48%	48	81%
13420-8-1	2015, Q3	BD	48%	76.2	83%
13420-9-1	2015, Q3	7H	48%	48	86%
13420-10-1	2015, Q3	BD	48%	76.2	86%
13420-10-2	2015, Q3	BD	48%	76.2	85%
13420-11-1	2015, Q3	7H	48%	48	85%

Specimen	Year/Quarter	Specimen Type	Fiber Vol. Fraction (%)	Dimensions (mm)	Rel. Density (%)
13420-12-1	2015, Q3	2H	36%	48	83%
13420-12-2	2015, Q3	BD	36%	48	87%
13420-13-1	2015, Q3	2H	36%	48	84%
13420-13-2	2015, Q3	BD	36%	48	84%
13420-14-1	2015, Q3	2H	36%	48	82%
13420-14-2	2015, Q3	BD	36%	48	85%
13420-15-1	2015, Q3	2H	36%	48	94%
13420-16-1	2015, Q3	BD	36%	76.2	78%
13420-16-2	2015, Q3	BD	36%	76.2	82%
13420-17-1	2015, Q3	7H	48%	48	85%
13420-17-2	2015, Q3	7H	48%	48	85%
13420-18-1	2015, Q3	BD	36%	76.2	89%
13420-19-1	2015, Q3	BD	36%	48	82%
13420-20-1	2015, Q3	7H	48%	48	86%
13420-20-2	2015, Q3	7H	48%	48	87%
13420-21-1	2015, Q3	BD	36%	48	82%
13420-22-1	2015, Q3	BD	36%	48	82%
13420-23-1	2015, Q3	7H	48%	48	91%
13420-24-1	2015, Q3	7H	48%	48	88%
13420-25-1	2015, Q3	7H	48%	48	86%
13420-25-2	2015, Q3	7H	48%	48	84%
13420-26-1	2015, Q3	TC	44%	48	96%
13420-27-1	2015, Q3	BD	36%	48	89%
13420-27-2	2015, Q3	BD	36%	48	89%
13420-28-1	2015, Q3	BD	36%	48	81%
13420-28-2	2015, Q3	BD	36%	48	82%
13420-29-1	2015, Q3	BD	36%	48	82%
13420-29-2	2015, Q3	BD	36%	48	84%
13420-30-1	2015, Q3	BD	36%	48	75%
13420-30-2	2015, Q3	BD	36%	48	76%
13420-31-1	2015, Q3	BD	36%	48	81%
13420-31-2	2015, Q3	BD	36%	48	81%
13420-32-1	2015, Q3	BD	60%	48	77%

Specimen	Year/Quarter	Specimen Type	Fiber Vol. Fraction (%)	Dimensions (mm)	Rel. Density (%)
130423-76-1	2015, Q3	PC	36%	a = 25.4 b = 29	61%
130423-81-1	2015, Q3	PC	36%	a = 25.4 b = 29	61%
130423-87-1	2015, Q3	PC	0%	a = 25.4 b = 29	76%
130423-88-1	2015, Q3	BD	36%	48	85%
130423-88-2	2015, Q3	BD	36%	48	84%
130423-92-1	2015, Q3	BD	36%	48	N/A
130423-92-2	2015, Q3	BD	36%	48	N/A
13420-33-1	2015, Q3	BD	36%	48	77%
13420-34-1	2015, Q4	BD	36%	48	86%
13420-35-1	2015, Q4	19H	36%	76.2	92%
13420-36-1	2015, Q4	7H	36%	76.2	85%
13420-37-1	2015, Q4	2H	48%	48	79%
13420-37-2	2015, Q4	2H	48%	48	78%
13420-37-3	2015, Q4	2H	48%	48	80%
13420-38-1	2015, Q4	2H	48%	48	80%
13420-38-2	2015, Q4	2H	48%	48	81%
13420-38-3	2015, Q4	2H	48%	48	80%
13420-39-1	2015, Q4	2H	48%	48	78%
13420-39-2	2015, Q4	2H	48%	48	79%
13420-39-3	2015, Q4	2H	48%	48	81%
13418-18-1	2015, Q4	SW	36%	a = 37 b = 39	56%
13420-40-1	2015, Q4	7H	36%	76.2	85%
13420-41-1	2015, Q4	BD	36%	48	84%
13420-42-1	2015, Q4	BD	36%	48	82%
13418-21-1	2015, Q4	SW	36%	a = 37 b = 39	77%
13418-25-1	2015, Q4	BD	0%	48	N/A
13418-25-2	2015, Q4	BD	0%	48	84%
13418-25-3	2015, Q4	BD	0%	48	89%
13420-45-1	2015, Q4	19H	36%	76.2	90%
13420-49-1	2015, Q4	19H	25%	76.2	96%
13420-50-1	2015, Q4	19H	36%	76.2	96%
13418-35-1	2015, Q4	PC	0%	a = 25.4 b = 29	63%
13418-36-1	2015, Q4	PC	0%	a = 25.4 b = 29	77%

Specimen	Year/Quarter	Specimen Type	Fiber Vol. Fraction (%)	Dimensions (mm)	Rel. Density (%)
13418-37-1	2015, Q4	PC	0%	a = 25.4 b = 29	90%
13418-51-1	2015, Q4	PC	36%	a = 25.4 b = 29	77%
13420-52-1	2015, Q4	BD	36%	48	86%
13420-52-2	2015, Q4	BD	36%	48	85%
13420-52-3	2015, Q4	BD	36%	48	86%
13420-53-1	2015, Q4	2H	48%	48	81%
13420-53-2	2015, Q4	2H	36%	48	83%
13418-41-1	2015, Q4	PC	0%	a = 25.4 b = 29	91%
13418-45-1	2015, Q4	PC	0%	a = 25.4 b = 29	79%
13418-49-1	2015, Q4	PC	0%	a = 25.4 b = 29	68%
13418-49-2	2015, Q4	PC	36%	a = 25.4 b = 29	83%
13420-54-1	2015, Q4	BD	36%	48	85%
13424-26-1	2015, Q4	BD	0%	48	N/A
13424-26-2	2015, Q4	BD	36%	48	82%
13420-55-1	2015, Q4	PC	0%	a = 25.4 b = 29	N/A
13420-56-1	2015, Q4	PC	0%	a = 25.4 b = 29	74%
13420-57-1	2015, Q4	PC	36%	a = 25.4 b = 29	82%
13420-58-1	2015, Q4	PC	0%	a = 25.4 b = 29	N/A
13420-59-1	2015, Q4	BD	36%	48	84%
13420-60-1	2016, Q1	PC	0%	a = 25.4 b = 29	86%
13420-61-1	2016, Q1	PC	36%	a = 25.4 b = 29	94%
13420-62-1	2016, Q1	PC	0%	a = 25.4 b = 29	92%
13420-63-1	2016, Q1	PC	0%	a = 25.4 b = 29	81%
13420-64-1	2016, Q1	BD	0%	101.6	N/A
13420-65-1	2016, Q1	SW	36%	a = 37 b = 39	94%
13420-66-1	2016, Q1	7H	0%	101.6	93%
13420-67-1	2016, Q1	SW	36%	a = 37 b = 39	N/A
13418-68-1	2016, Q1	SW	36%	a = 25.4 b = 29	N/A
13420-69-1	2016, Q1	BD	36%	48	80%
13420-70-1	2016, Q1	7H	0%	101.6	93%
13420-71-1	2016, Q1	BD	48%	48	75%
13420-72-1	2016, Q1	BD	0%	101.6	95%
13420-73-1	2016, Q1	SW	36%	a = 37 b = 39	N/A

Specimen	Year/Quarter	Specimen Type	Fiber Vol. Fraction (%)	Dimensions (mm)	Rel. Density (%)
13420-74-1	2016, Q1	7H	36%	101.6	N/A
13420-75-1	2016, Q1	BD	36%	48	87%
13420-75-2	2016, Q1	BD	36%	48	N/A
13420-76-1	2016, Q1	BD	48%	48	N/A
13420-77-1	2016, Q1	7HwCC	0%	101.6	97%
13420-78-1	2016, Q1	7D	0%	101.6	96%
13420-79-1	2016, Q1	BD	36%	48	N/A
13420-80-1	2016, Q1	BD	48%	48	87%
13420-81-1	2016, Q1	7H	36%	101.6	N/A
13420-82-1	2016, Q1	PC	36%	a = 25.4 b = 29	81%
13420-83-1	2016, Q1	PC	36%	a = 25.4 b = 29	87%
13420-84-1	2016, Q1	BD	48%	48	N/A
13420-85-1	2016, Q1	HX	36%	150 x 25	N/A
13420-86-1	2016, Q1	SW	36%	a = 25.4 b = 29	82%
13420-87-1	2016, Q1	HX	36%	150 x 25	N/A
13420-88-1	2016, Q1	SW	36%	a = 25.4 b = 29	N/A
13420-89-1	2016, Q1	HX	36%	150 x 25	N/A
13420-90-1	2016, Q1	HX	36%	150 x 25	N/A
13420-91-1	2016, Q1	BD	48%	48	N/A
13420-91-2	2016, Q1	BD	48%	48	N/A
13420-92-1	2016, Q1	7H HX	0%	48	N/A
13451-2-1	2016, Q1	BD	48%	76.2	N/A
13451-2-2	2016, Q1	BD	48%	76.2	N/A
13451-3-1	2016, Q1	7H HX	0%	48	N/A
13451-4-1	2016, Q1	HX	36%	150 x 25	94%
13451-5-1	2016, Q1	7H HX	0%	48	N/A
13451-6-1	2016, Q1	BD	48%	48	85%
13451-7-1	2016, Q1	HX	36%	150 x 25	93%
13451-8-1	2016, Q1	BD	0%	101.6	N/A
13451-9-1	2016, Q1	HX	36%	150 x 25	89%
13451-10-1	2016, Q1	HX	36%	150 x 25	N/A
13451-11-1	2016, Q1	HX	36%	150 x 25	90%
13451-12-1	2016, Q1	BD	48%	48	79%

Specimen	Year/Quarter	Specimen Type	Fiber Vol. Fraction (%)	Dimensions (mm)	Rel. Density (%)
13451-12-2	2016, Q1	BD	48%	48	80%
13451-12-3	2016, Q1	BD	48%	48	80%
13451-13-1	2016, Q1	HX	36%	150 x 25	N/A
13451-14-1	2016, Q2	7H	48%	101.6	91%
13451-15-1	2016, Q2	7D	48%	101.6	N/A
13451-16-1	2016, Q2	7DwCC	48%	101.6	N/A
13451-17-1	2016, Q2	7DwCC	48%	101.6	N/A
13451-18-1	2016, Q2	7DwCC	48%	101.6	N/A
13451-19-1	2016, Q2	BD	48%	48	82%
13451-19-2	2016, Q2	BD	48%	48	83%
13451-19-3	2016, Q2	BD	48%	48	N/A
13451-20-1	2016, Q2	BD	48%	48	84%
13451-20-2	2016, Q2	BD	48%	48	81%
13451-20-3	2016, Q2	BD	48%	48	83%
13451-21-1	2016, Q2	PC	48%	a = 25.4 b = 29	73%
13451-21-2	2016, Q2	PC	48%	a = 25.4 b = 29	75%
13451-22-1	2016, Q2	PC	48%	a = 25.4 b = 29	78%
13451-23-1	2016, Q2	PC	48%	a = 25.4 b = 29	74%
13451-23-2	2016, Q2	PC	48%	a = 25.4 b = 29	70%
13451-24-1	2016, Q2	HX	36%	150 x 25	N/A
13451-25-1	2016, Q2	BDwCC	48%	101.6	N/A
13451-26-1	2016, Q2	BDwCC	48%	101.6	87%
13451-26-2	2016, Q2	BD	0%	101.6	92%
13451-27-1	2016, Q2	BD	48%	48	85%
13451-27-2	2016, Q2	BD	48%	48	85%
13451-27-3	2016, Q2	BD	48%	48	85%
13451-28-1	2016, Q2	HX	36%	150 x 25	83%
13451-29-1	2016, Q2	BD	48%	48	89%
13451-29-2	2016, Q2	BD	48%	48	85%
13451-29-3	2016, Q2	BD	48%	48	86%
13451-30-1	2016, Q2	4H	48%	50.8	N/A
13451-30-2	2016, Q2	4H	48%	50.8	N/A
13451-31-1	2016, Q2	5H	48%	50.8	87%

Specimen	Year/Quarter	Specimen Type	Fiber Vol. Fraction (%)	Dimensions (mm)	Rel. Density (%)
13451-31-2	2016, Q2	5H	48%	50.8	88%
13451-32-1	2016, Q2	4H	48%	50.8	N/A
13451-32-2	2016, Q2	4H	48%	50.8	N/A
13451-33-1	2016, Q2	BD	48%	48	91%
13451-33-2	2016, Q2	BD	48%	48	92%
13451-34-1	2016, Q2	MM	N/A	50.8	N/A
13451-35-1	2016, Q2	BD	N/A	48	93%
13451-35-2	2016, Q2	BD	N/A	48	90%
13451-36-1	2016, Q2	BD	N/A	50.8	84%
13451-36-2	2016, Q2	BD	N/A	50.8	83%
13451-36-3	2016, Q2	BD	N/A	50.8	86%
13451-37-1	2016, Q2	BD	N/A	50.8	N/A
13451-37-2	2016, Q2	BD	N/A	50.8	N/A
13451-37-3	2016, Q2	BD	N/A	50.8	N/A
13451-38-1	2016, Q2	MM	N/A	50.8	N/A
13451-39-1	2016, Q2	BD	0%	50.8	N/A
13451-39-2	2016, Q2	BD	0%	50.8	N/A
13451-39-3	2016, Q2	BD	0%	50.8	N/A
13451-40-1	2016, Q3	BD	48%	48	N/A
13451-40-2	2016, Q3	BD	48%	48	N/A
13451-41-1	2016, Q3	BD	48%	48	86%
13451-41-2	2016, Q3	BD	48%	48	80%
13451-42-1	2016, Q3	BD	48%	48	N/A
13451-42-2	2016, Q3	BD	48%	48	N/A
13451-43-1	2016, Q3	BD	48%	48	N/A
13451-43-2	2016, Q3	BD	48%	48	N/A
13451-44-1	2016, Q3	BD	48%	48	N/A
13451-44-2	2016, Q3	BD	48%	48	N/A
13451-45-1	2016, Q3	BDwCC	48%	101.6	N/A
13451-46-1	2016, Q3	BDwCC	48%	101.6	87%
13451-47-1	2016, Q3	MM	N/A	101.6	N/A
13451-48-1	2016, Q3	BD	48%	101.6	N/A
13451-49-1	2016, Q3	BDwCC	48%	101.6	N/A

Specimen	Year/Quarter	Specimen Type	Fiber Vol. Fraction (%)	Dimensions (mm)	Rel. Density (%)
13451-50-1	2016, Q3	BD	0%	101.6	N/A
13451-51-1	2016, Q3	BDwCC	48%	101.6	N/A
13451-52-1	2016, Q3	BD	0%	101.6	N/A
13451-53-1	2016, Q3	7HwCC	48%	101.6	86%
13451-54-1	2016, Q3	BD	48%	48	N/A
13451-55-1	2016, Q3	7HwCC	48%	101.6	N/A
13451-56-1	2016, Q3	MM	N/A	101.6	N/A
13451-57-1	2016, Q3	BDwCC	48%	101.6	88%
13451-58-1	2016, Q3	BD	48%	48	N/A
13451-59-1	2016, Q3	BD	48%	48	80%
13451-60-1	2016, Q3	BD	48%	48	82%
13451-62-1	2016, Q3	BD	48%	48	88%
13451-62-2	2016, Q3	BD	48%	48	88%
13451-63-1	2016, Q3	BD	48%	48	88%
13451-63-2	2016, Q3	BD	48%	48	89%
13451-64-1	2016, Q3	BD	48%	48	89%
13451-64-2	2016, Q3	BD	48%	48	87%
13451-65-1	2016, Q3	BD	48%	48	86%
13451-65-2	2016, Q3	BD	48%	48	85%
13466-40-1	2016, Q3	BD	0%	50.8	92%
13466-40-2	2016, Q3	BD	0%	50.8	87%
13451-66-1	2016, Q3	BD	48%	48	88%
13451-67-1	2016, Q3	BD	48%	48	88%
13451-67-2	2016, Q3	BD	48%	48	85%
13451-68-1	2016, Q3	BD	48%	48	85%
13451-68-2	2016, Q3	BD	48%	48	83%
13451-69-1	2016, Q4	BDwCC	48%	101.6	91%
13451-70-1	2016, Q4	BD	48%	48	84%
13451-70-2	2016, Q4	BD	48%	48	84%
13451-71-1	2016, Q4	BDwCC	48%	101.6	N/A
13451-72-1	2016, Q4	5H	48%	50.8	91%
13451-72-2	2016, Q4	5H	48%	50.8	90%
13451-73-1	2016, Q4	4H	48%	50.8	89%

Specimen	Year/Quarter	Specimen Type	Fiber Vol. Fraction (%)	Dimensions (mm)	Rel. Density (%)
13451-73-2	2016, Q4	4H	48%	50.8	91%
13451-74-1	2016, Q4	4H	48%	50.8	90%
13451-74-2	2016, Q4	4H	48%	50.8	90%
13451-74-3	2016, Q4	4H	48%	50.8	90%
13451-75-1	2016, Q4	BD	48%	101.6	N/A
13451-76-1	2016, Q4	2H	36%	48	86%
13451-76-2	2016, Q4	2H	48%	48	83%
13451-77-1	2016, Q4	BD	0%	48	N/A
13451-77-2	2016, Q4	BD	0%	48	N/A
13451-77-3	2016, Q4	BD	0%	48	N/A
13451-78-1	2016, Q4	BD	0%	48	97%
13451-78-2	2016, Q4	BD	0%	48	98%
13451-78-3	2016, Q4	BD	0%	48	96%
13451-79-1	2016, Q4	4H	48%	50.8	90%
13451-80-1	2016, Q4	BJ	N/A	80 x 40	N/A
13451-81-1	2016, Q4	4H	48%	50.8	92%
13451-81-2	2016, Q4	BD	48%	50.8	N/A
13451-82-1	2016, Q4	5H	48%	50.8	93%
13451-82-2	2016, Q4	5H	48%	50.8	93%
13451-83-1	2016, Q4	4H	48%	50.8	92%
13451-83-2	2016, Q4	4H	48%	50.8	90%
13451-84-1	2016, Q4	MM	N/A	40 x 40 x 6	N/A
13451-85-1	2016, Q4	BJ	N/A	80 x 40	N/A
13451-86-1	2016, Q4	5H	48%	50.8	94%
13451-86-2	2016, Q4	5H	48%	50.8	93%
13451-87-1	2016, Q4	4H	48%	50.8	94%
13451-87-2	2016, Q4	4H	48%	50.8	93%
13451-88-1	2016, Q4	4H	48%	50.8	93%
13451-88-2	2016, Q4	4H	48%	50.8	93%
13451-89-1	2016, Q4	5H	48%	50.8	95%
13451-89-2	2016, Q4	5H	48%	50.8	94%
13451-90-1	2016, Q4	MM	N/A	40 x 40 x 6	N/A
13451-91-1	2016, Q4	T&G	N/A	80 x 40	N/A

Specimen	Year/Quarter	Specimen Type	Fiber Vol. Fraction (%)	Dimensions (mm)	Rel. Density (%)
13451-92-1	2016, Q4	BD	48%	101.6	N/A
13537-2-1	2016, Q4	4H	48%	50.8	94%
13537-2-2	2016, Q4	4H	48%	50.8	93%
13537-3-1	2016, Q4	4H	48%	50.8	N/A
13537-3-2	2016, Q4	4H	48%	50.8	N/A
13537-4-1	2016, Q4	5H	48%	50.8	N/A
13537-4-2	2016, Q4	5H	48%	50.8	N/A
13537-5-1	2016, Q4	4H	48%	50.8	N/A
13537-5-2	2016, Q4	4H	48%	50.8	N/A
13537-6-1	2016, Q4	4H	48%	50.8	N/A
13537-6-2	2016, Q4	4H	48%	50.8	N/A
13537-7-1	2016, Q4	4H	48%	50.8	N/A
13537-7-2	2016, Q4	4H	48%	50.8	N/A
13537-8-1	2016, Q4	5H	48%	50.8	N/A
13537-8-2	2016, Q4	5H	48%	50.8	N/A
13537-9-1	2016, Q4	MLJ	N/A	50.8	N/A
13537-9-2	2016, Q4	MLJ	N/A	50.8	N/A
13537-10-1	2016, Q4	4H	48%	50.8	N/A
13537-10-2	2016, Q4	4H	48%	50.8	N/A
13537-11-1	2016, Q4	4H	48%	50.8	91%
13537-11-2	2016, Q4	4H	48%	50.8	92%
13537-12-1	2016, Q4	MLJ	N/A	50.8	N/A
13537-12-2	2016, Q4	MLJ	N/A	50.8	N/A
13537-13-1	2016, Q4	MM	0%	40 x 40 x 6	N/A
13537-13-2	2016, Q4	MM	0%	40 x 40 x 6	N/A
13530-40-1	2016, Q4	BD	24%	50.8	84%
13530-40-2	2016, Q4	BD	48%	50.8	83%
13530-40-3	2016, Q4	BD	36%	50.8	86%
13537-14-1	2016, Q4	BJ	N/A	40 x 40	N/A
13537-15-1	2016, Q4	MM	N/A	40 x 40 x 6	N/A
13537-15-2	2016, Q4	MM	N/A	40 x 40 x 6	N/A
13537-16-1	2016, Q4	BJ	N/A	40 x 40	N/A
13537-17-1	2016, Q4	BJ	N/A	40 x 40	N/A

Specimen	Year/Quarter	Specimen Type	Fiber Vol. Fraction (%)	Dimensions (mm)	Rel. Density (%)
13537-19-1	2016, Q4	4X	24%	80 x 80	N/A
13537-20-1	2016, Q4	MLJ	N/A	40 x 40 x 6	N/A
13537-21-1	2016, Q4	MLJ	N/A	40 x 40 x 6	N/A
13537-22-1	2016, Q4	CG	N/A	80 x 40	N/A
13537-23-1	2016, Q4	BJ	N/A	80 x 40	N/A
13537-24-1	2016, Q4	MLJ	N/A	40 x 40 x 6	N/A
13537-25-1	2016, Q4	MLJ	N/A	40 x 40 x 6	N/A
13537-26-1	2016, Q4	CG	N/A	80 x 40	N/A
13466-45-1	2016, Q4	BD	0%	48	N/A
13466-45-2	2016, Q4	BD	0%	48	97%
13466-45-3	2016, Q4	BD	48%	48	95%
13466-46-1	2016, Q4	BD	0%	48	93%
13466-46-2	2016, Q4	BD	0%	48	94%
13466-47-1	2016, Q4	BD	0%	50.8	98%
13466-47-2	2016, Q4	BD	0%	50.8	95%
13466-50-1	2016, Q4	BD	48%	50.8	87%
13466-50-2	2016, Q4	BD	48%	50.8	89%
13466-53-1	2016, Q4	BD	0%	50.8	96%
13466-55-1	2016, Q4	BD	0%	50.8	90%
13466-57-1	2016, Q4	BD	0%	50.8	97%
13466-57-2	2016, Q4	BD	48%	50.8	97%
13466-57-3	2016, Q4	BD	48%	50.8	97%
13466-62-1	2016, Q4	BD	0%	50.8	94%
13466-62-2	2016, Q4	BD	48%	50.8	94%
13466-62-3	2016, Q4	BD	48%	50.8	95%
13466-67-1	2016, Q4	BD	48%	50.8	86%
13466-67-2	2016, Q4	BD	48%	50.8	86%
13466-70-1	2016, Q4	BD	0%	50.8	97%
13466-70-2	2016, Q4	BD	48%	50.8	93%
13466-70-3	2016, Q4	BD	48%	50.8	93%
13466-87-1	2016, Q4	BD	0%	50.8	88%
13466-87-2	2016, Q4	BD	48%	50.8	81%
13466-87-3	2016, Q4	BD	48%	50.8	79%

Specimen	Year/Quarter	Specimen Type	Fiber Vol. Fraction (%)	Dimensions (mm)	Rel. Density (%)
13537-27-1	2017, Q1	MLJ	N/A	40 x 40 x 6	N/A
13537-28-1	2017, Q1	MLJ	N/A	40 x 40 x 6	N/A
13537-29-1	2017, Q1	MLJ	N/A	40 x 40 x 6	N/A
13537-30-1	2017, Q1	MLJ	N/A	40 x 40 x 6	N/A
13537-31-1	2017, Q1	CG	N/A	80 x 40	N/A
13537-32-1	2017, Q1	BJ	N/A	80 x 40	N/A
13537-33-1	2017, Q1	BJ	N/A	80 x 40	N/A
13537-34-1	2017, Q1	BJ	N/A	80 x 40	N/A
13537-35-1	2017, Q1	T&G	N/A	80 x 40	N/A
13537-36-1	2017, Q1	BJ	N/A	80 x 40	N/A
13537-37-1	2017, Q1	BJ	N/A	80 x 40	N/A
13537-38-1	2017, Q1	BJ	N/A	80 x 40	N/A
13537-39-1	2017, Q1	BJ	N/A	80 x 40	N/A
13537-40-1	2017, Q1	BD	48%	50.8	N/A
13537-41-1	2017, Q1	BJ	N/A	80 x 40	N/A
13537-42-1	2017, Q1	BD	48%	50.8	N/A
13537-43-1	2017, Q1	MLJ	N/A	40 x 40 x 6	N/A
13537-44-1	2017, Q1	MLJ	N/A	40 x 40 x 6	N/A
13537-45-1	2017, Q1	MLJ	N/A	40 x 40 x 6	N/A
13537-46-1	2017, Q1	BD	48%	50.8	N/A
13537-47-1	2017, Q1	MLJ	N/A	40 x 40 x 6	N/A
13537-48-1	2017, Q1	BD	48%	50.8	90%
13537-48-2	2017, Q1	BD	48%	50.8	87%
13537-49-1	2017, Q1	BD	48%	50.8	87%
13537-49-2	2017, Q1	BD	48%	50.8	87%
13537-50-1	2017, Q1	BJ	N/A	80 x 40	N/A
13537-51-1	2017, Q1	BJ	N/A	80 x 40	N/A
13537-52-1	2017, Q1	BJ	N/A	80 x 40	N/A
13537-53-1	2017, Q1	BJ	N/A	80 x 40	N/A
13537-54-1	2017, Q1	MLJ	N/A	40 x 40 x 6	N/A
13537-54-2	2017, Q1	MLJ	N/A	40 x 40 x 6	N/A
13537-55-1	2017, Q1	BJ	N/A	80 x 40	N/A
13537-56-1	2017, Q1	BJ	N/A	80 x 40	N/A

Specimen	Year/Quarter	Specimen Type	Fiber Vol. Fraction (%)	Dimensions (mm)	Rel. Density (%)
13537-57-1	2017, Q1	BJ	N/A	80 x 40	N/A
13537-58-1	2017, Q2	BD	54%	50.8	90%
13537-60-1	2017, Q2	5H	48%	50.8	91%
13537-62-1	2017, Q2	MM	N/A	50.8	N/A
13537-63-1	2017, Q2	4H	54%	50.8	91%
13537-64-1	2017, Q2	7DwCC	48%	101.6	N/A

Appendix B – Large Data Set Composite Flexural Strength

Test Number	Strength (sorted) (MPa)	P_f	$\ln(\ln(1/1-P_f))$	ln(stress)
1	232.00	0.0143	-4.2413	5.4467
2	239.30	0.0429	-3.1281	5.4777
3	247.00	0.0714	-2.6022	5.5094
4	253.23	0.1000	-2.2504	5.5343
5	260.10	0.1286	-1.9832	5.5611
6	264.90	0.1571	-1.7663	5.5794
7	265.67	0.1857	-1.5826	5.5823
8	269.00	0.2143	-1.4223	5.5947
9	269.80	0.2429	-1.2794	5.5977
10	270.99	0.2714	-1.1499	5.6021
11	271.63	0.3000	-1.0309	5.6044
12	272.11	0.3286	-0.9204	5.6062
13	273.10	0.3571	-0.8168	5.6098
14	283.88	0.3857	-0.7189	5.6486
15	290.97	0.4143	-0.6256	5.6732
16	294.14	0.4429	-0.5363	5.6841
17	303.00	0.4714	-0.4501	5.7137
18	321.40	0.5000	-0.3665	5.7727
19	323.00	0.5286	-0.2850	5.7777
20	329.00	0.5571	-0.2052	5.7961
21	329.70	0.5857	-0.1265	5.7982
22	332.20	0.6143	-0.0485	5.8057
23	334.00	0.6429	0.0292	5.8111
24	353.29	0.6714	0.1071	5.8673
25	355.40	0.7000	0.1856	5.8732
26	359.56	0.7286	0.2655	5.8849
27	362.64	0.7571	0.3473	5.8934
28	369.25	0.7857	0.4321	5.9115
29	378.00	0.8143	0.5209	5.9349
30	378.15	0.8429	0.6155	5.9353
31	394.84	0.8714	0.7185	5.9785
32	421.00	0.9000	0.8340	6.0426
33	422.27	0.9286	0.9704	6.0456
34	426.00	0.9571	1.1474	6.0544
35	440.50	0.9857	1.4466	6.0879

Specimen IDs	13418-54-1, 130424-68-1, 130424-74-3, 130424-84-1
Average Strength (MPa)	320
Max Strength (MPa)	441
Min Strength (MPa	232
St. Deviation (MPa)	59
Char. Strength (MPa)	332
Weibull	6.48

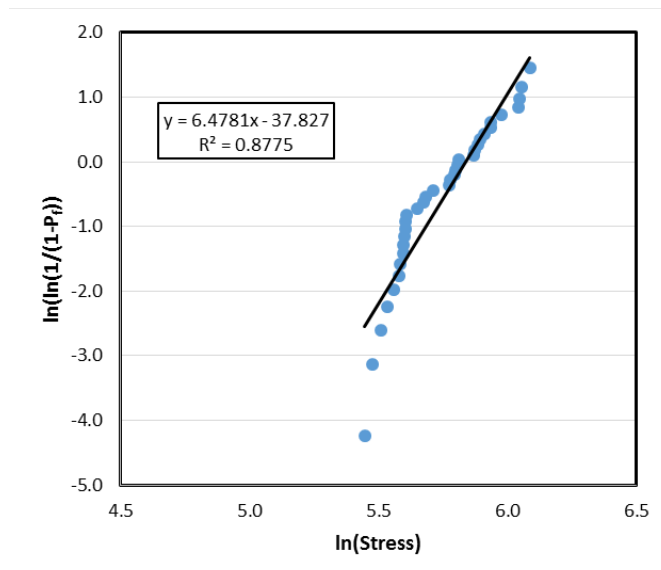

Appendix C – Large Data Set Butt Joint Strength

Specimen I.D.	Length (mm)	Width (mm)	Thickness (mm)	Strength (MPa)	Fracture Type	Valid, Y/N
BJ-LS-1	88.84	8.10	6.01	83	Substrate	Y
BJ-LS-2	88.77	7.72	6.03	105	Substrate	Y
BJ-LS-3	88.90	8.03	6.02	43	Substrate	Y
BJ-LS-4	88.27	8.25	6.03	47	Substrate	Y
BJ-LS-5	88.27	8.20	6.01	46	Substrate	Y
BJ-LS-6	88.18	8.20	6.01	50	Substrate	Y
BJ-LS-7	88.13	8.24	6.02	85	Substrate	Y
BJ-LS-8	88.37	8.28	6.01	53	Substrate	Y
BJ-LS-9	89.27	8.11	6.01	56	Substrate	N
BJ-LS-10	89.31	8.17	6.01	58	Substrate	N
BJ-LS-11	89.48	7.16	6.01	25	Substrate	N
BJ-LS-12	89.48	7.99	6.01	29	Substrate	Y
BJ-LS-13	90.01	8.15	6.34	37	Substrate	Y
BJ-LS-14	87.38	8.11	5.52	24	Cohesive	Y
BJ-LS-15	87.73	8.05	5.53	31	Cohesive	Y

GENERAL ATOMICS

EM²

UNIVERSITY OF SOUTH CAROLINA

Fabrication and Testing of Complex SiC/SiC Composite Structures

Hesham E. Khalifa, Chunghao P. Shih, George M. Jacobsen, Christian P. Deck
General Atomics Energy and Advanced Concepts Group, Nuclear Technologies and Materials Division
3550 General Atomics Ct., San Diego, CA 92121

ANS Annual Meeting NFSM June 13-16, 2016 New Orleans, LA

U.S. DEPARTMENT OF ENERGY
Advanced Reactor Concepts Grant DE-NE0008323

Summary

Silicon carbide (SiC) and silicon carbide fiber-reinforced, silicon carbide matrix composites (SiC/SiC) are leading candidates for cladding and core structures used in advanced reactor concepts such as General Atomics' (GA) Energy Multiplier Module (EM²) as well as accident tolerant fuel (ATF) in LWRs. SiC retains its strength up to very high temperatures, is stable under irradiation, and shows favorable neutronics and oxidation resistance compared to alloy alternatives.

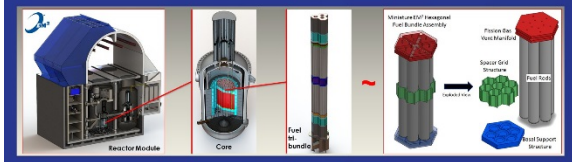

The ability to fabricate larger complex silicon carbide composites is an enabling technology for advanced reactors. This paper describes recent efforts targeting fabrication of complex SiC/SiC composites for in-core support structures. The work focused on transient eutectic phase (TEP) processing of near-net shape composites with thru-hole features to serve as fuel rod support and gas manifold structures. These geometries represent a level of complexity that has not yet been established in nuclear-grade SiC/SiC composites. The goal of this work is to employ specialized test techniques to better understand the effect of part complexity on SiC/SiC composite performance and use this data to establish limits on part complexity such as feature size and spacing which may provide important implications on fuel loading and efficiency in advanced reactor designs.

Composite Processing of Complex Structures

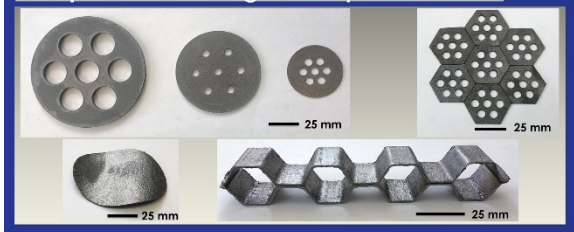

- TEP process yields high density (>2.9 g/cm³) and short processing times (60m)
- SiC purity and migration of oxides to grain boundary triple points make TEP material stable under neutron irradiation [1,2]
- Planar composites with various thru hole features were fabricated
  - Parts were fabricated in diameters of 50 - 100 mm and thickness of 0.5-25 mm
  - Features ranged in diameter from 3-20 mm with spacing varying from 3-14mm
- Non-planar curved and faceted structures were also fabricated

TEP SiC/SiC Exhibits High PLS and Modulus

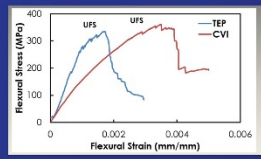

Fabrication type	ρ_{rel} (%)	PLS (MPa)	UFS (MPa)	E (GPa)	m_{PLS}	m_{UFS}	m_E
TEP, 4 ply	90	181	292	347	6.4	7.1	3.6
CVI, 4 ply	84	113	324	234	3.8	4.3	3.9

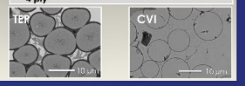

- Higher density of TEP SiC/SiC increases matrix cracking stress, stiffness, and Weibull modulus
- Reduced strain to failure compared with CVI SiC/SiC

Microstructural Variations Identified with X-Ray Computed Tomography (XCT)

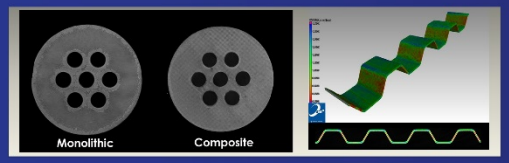

- Affected region observed around thru-hole features and specimen edge in monolithic specimens but not in composite
- Thickness variation observed in hexagonal corrugated structure may result in differential densification and performance

Unique Thermo-mechanical Phenomena Arise Near Features During TEP Process

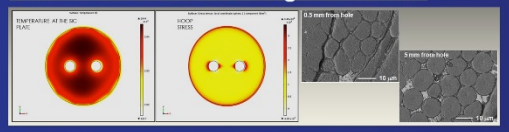

- TEP consolidation modeled in COMSOL
- Localized regions of lower temperature are observed near specimen edges due to axial and radial thermal gradients
  - These regions match well with affected zones observed in XCT
- Differential CTE between SiC and graphite tooling gives rise to anomalous stress distribution near thru-hole features
- Fiber deformation observed within 500 µm of feature edge

Feature Spacing Evaluated with Microhardness Testing and Open Hole Tension

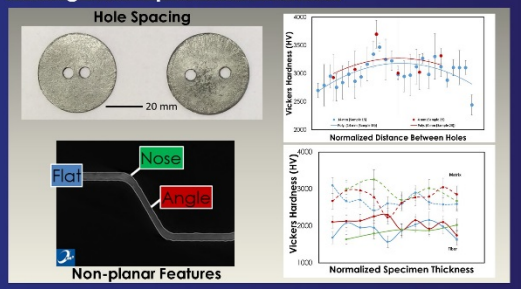

- Hardness did not change as a function of thru-hole feature spacing or specimen curvature
- Local decrease in hardness near feature edge matches anomalous strain distribution and thermal gradient from heat transfer model

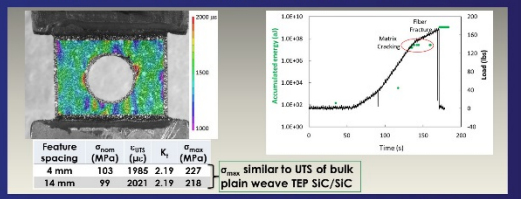

Feature spacing	σ_{nom} (MPa)	ε_{UTS} (µε)	K_t	σ_{max} (MPa)
4 mm	103	1985	2.19	227
14 mm	99	2021	2.19	218

σ_{max} similar to UTS of bulk plain weave TEP SiC/SiC

- Digital Image Correlation (DIC) and Acoustic Emission (AE) facilitate strain mapping and defect detection near hole features
- Strain evolution and strength were similar irrespective of feature spacing and strain localized to within 500 µm of feature edge
- AE data for PLS (10^7 aJ) and UTS (10^9 aJ) match well with bulk SiC/SiC
- Minimum hole spacing governed by fiber architecture which for plain weave SA3 fabric is ~2.6 mm

Conclusions

- SiC/SiC has been fabricated in complex geometries targeting in-core structural components via near-net-shape TEP processing
- SiC/SiC strength, pseudoductility, and hardness are minimally affected by processing effects in complex geometries
- Lower limits of feature spacing have implications on potential core loading limits

1. SHIMOOKA, K. **Comp. Sc. & Tech.**, v. 71, p. 439-445, 2011.
2. HAYWARD, et al. **J. of Nuc. Mat.**, v. 426, p. 268-276, 2012.

DISCLAIMER: This report was prepared as an account of work sponsored by an agency of the United States Government. Neither the United States Government nor any agency thereof, nor any of their employees, makes any warranty, express or implied, or assumes any legal liability or responsibility for the accuracy, completeness, or usefulness of any information, apparatus, product, or process disclosed, or represents that its use would not infringe privately owned rights. Reference herein to any specific commercial product, process, or service by trade name, trademark, manufacturer, or otherwise, does not necessarily constitute or imply its endorsement, recommendation, or favoring by the United States Government or any agency thereof. The views and opinions of authors expressed herein do not necessarily state or reflect those of the United States Government or any agency thereof.

ACKNOWLEDGMENTS: This work was funded by the U.S. Department of Energy (DE-NE0008323) via an Advanced Reactor Concepts (ARC) contract for reactor fabrication and characterization of complex SiC/SiC structures. The views and opinions of authors expressed herein do not necessarily state or reflect those of the US Government or any agency thereof. The authors would like to acknowledge NFM lab personnel for fabrication and coupon preparation as well as the Navy at Dahlgren and Dr. Jim Stokes at Naval Research Laboratory for assistance with AE and DIC testing and discussion.

Appendix E – ICACC 2017 Presentation

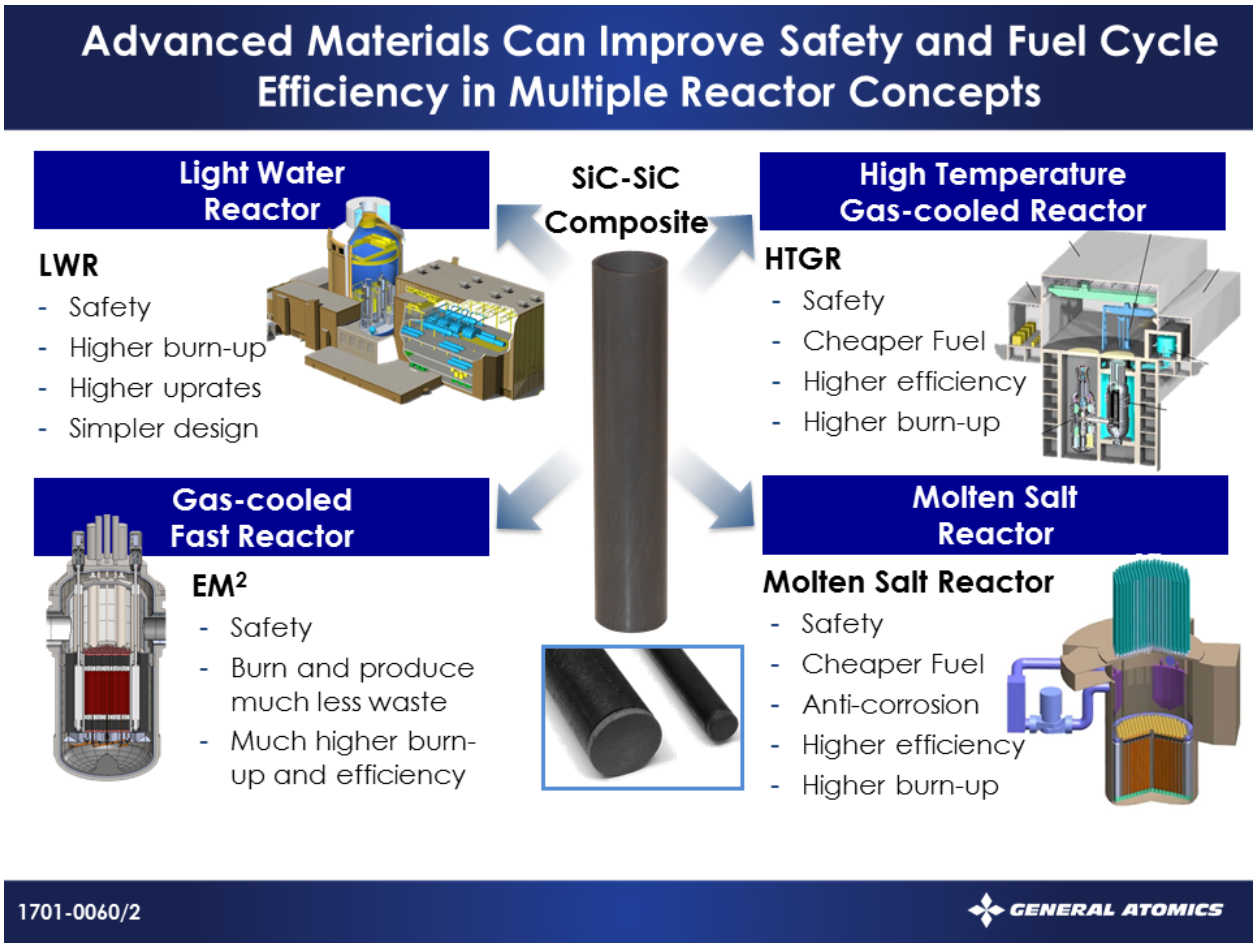
Advanced Materials Can Improve Safety and Fuel Cycle Efficiency in Multiple Reactor Concepts
Light Water Reactor
LWR
- Safety
- Higher burn-up
- Higher uprates
- Simpler design
SiC-SiC Composite
High Temperature Gas-cooled Reactor
HTGR
- Safety
- Cheaper Fuel
- Higher efficiency
- Higher burn-up
Gas-cooled Fast Reactor
EM2
- Safety
- Burn and produce much less waste
- Much higher burn-up and efficiency
Molten Salt Reactor
Molten Salt Reactor
- Safety
- Cheaper Fuel
- Anti-corrosion
- Higher efficiency
- Higher burn-up
1701-0060/2
GENERAL ATOMICS

EM²'s Innovative Fuel System Is the Key to High Efficiency and Increased Burn-up

- **Uranium Carbide (UC) Fuel**
  - Favorable melting point and thermal conductivity
  - High uranium density
- **Silicon Carbide Fiber Reinforced Composite (SiC-SiC) Cladding and Core Structural Components**
  - Retains strength at elevated temperature
  - Stable under irradiation

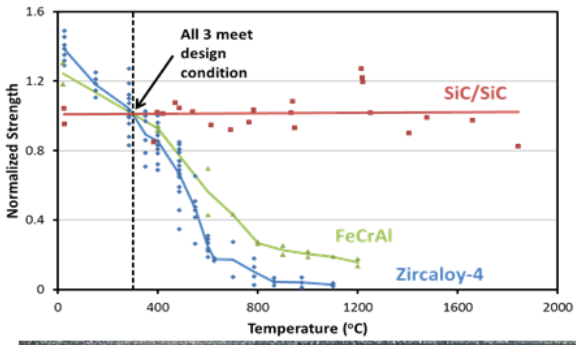

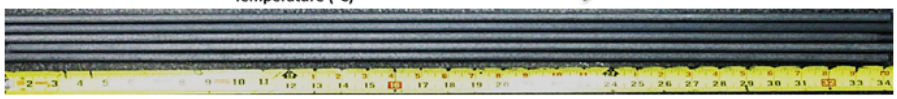

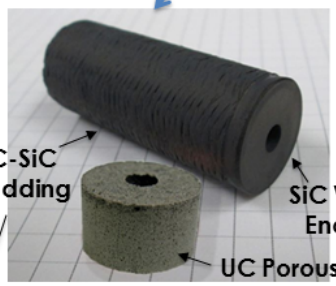

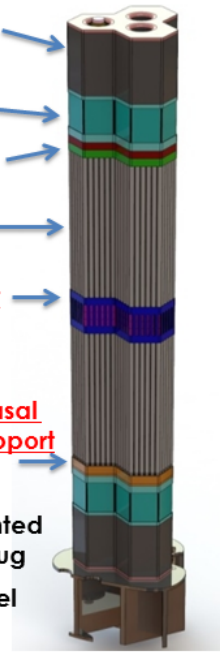

EM² Tri-Bundle Fuel Assembly

1701-0060/3

GENERAL ATOMICS

GA's DOE-ART Project Leverages Modular Fabrication Techniques to Produce Complex SiC-SiC Components

1. **Planar SiC-SiC Structures with Internal Features**

   Investigate near-net shape processing to make composites with thru-holes. Characterize bulk and local property variation to assess limits on feature spacing

2. **Fuel Rod Support Structures**

   Expand near-net shape processing to create non-planar SiC-SiC composite components targeting fuel rod support structures and examine local property variation

3. **Joined Multi-layer Vent Manifold Structure**

   Modular multi-layer bonding. Combine complex bulk processing and new joining techniques for enhanced complexity

4. **Edge-to-Edge Joining of Multi-Layer Structures**

   Demonstrate scalability of complex structure fabrication by joining multiple multi-layer structures to create larger assemblies

1701-0060/4 GENERAL ATOMICS

Task 1:Planar Structures - Transient Eutectic Phase Processing Enables Rapid Densification of Thick SiC-SiC Components

- **Chemical Vapor Infiltration is the favored technique for fabricating thin-walled tubes for cladding**
  - High purity but slow process with limited max thickness
- **Hot Press SiC Fabrication (TEP) of SiC-SiC is preferred route for large, complex structures**
  - Higher density (>2.9 g/cm^3) increases matrix cracking stress,
  - Thicker part capability, >25 mm thickness
  - Rapid densification, >60m at high temperature and pressure
  - Near-net-shape processing – limits machining $$

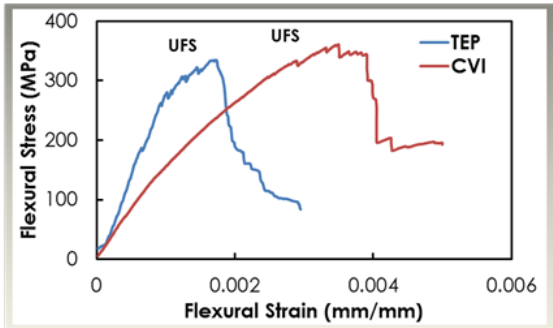

Fabrication type	ρ_{rel} (%)	PLS (MPa)	UFS (MPa)	E (GPa)	m_{PLS}	m_{UFS}	m_E
TEP, 4 ply	90	181	292	347	6.4	7.1	3.6
CVI, 4 ply	84	113	324	234	3.8	4.3	3.9

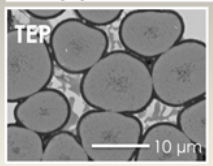

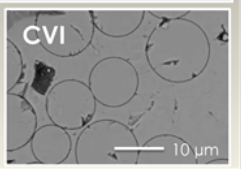

1701-0060/5 1- T. Koyanagi, JNM, 448 (2014) p. 478-786 GENERAL ATOMICS

Task 1:TEP Route Was Used to Fabricate Composite Plates with Thru-hole Features

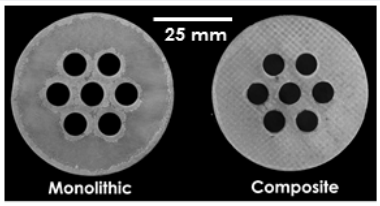

- **Microstructural variations ID'd with X-ray Computed Tomography (XCT)**
  - Affected region observed around thru-hole features and specimen edge in monolithic specimens but not in composite

Heat Transfer Modeling of Consolidation in COMSOL

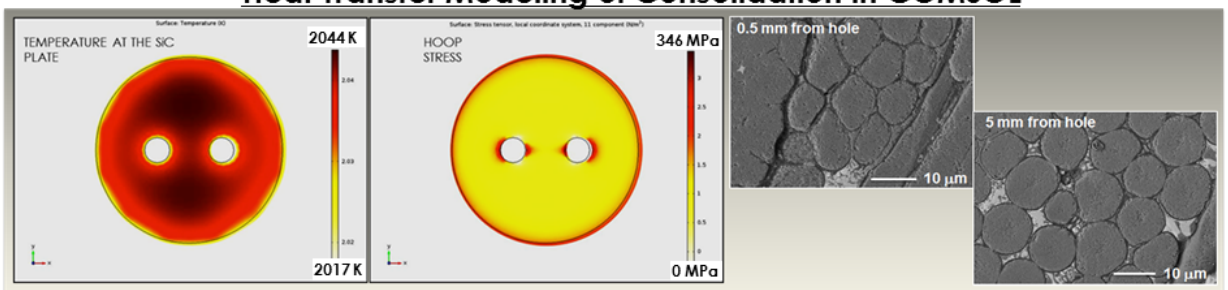

- **Localized regions of lower temperature near specimen edges due to axial and radial thermal gradients**
  - These regions match well with affected zones observed in XCT
- **Differential CTE between SiC and graphite tooling gives rise to anomalous stress distribution near thru-hole features**
- **Fiber deformation observed within 500 µm of feature edge**

1701-0060/6 GENERAL ATOMICS

Task 1: Effect of Hole Spacing Was Assessed Using Micro- and Macro-scale Characterization Techniques

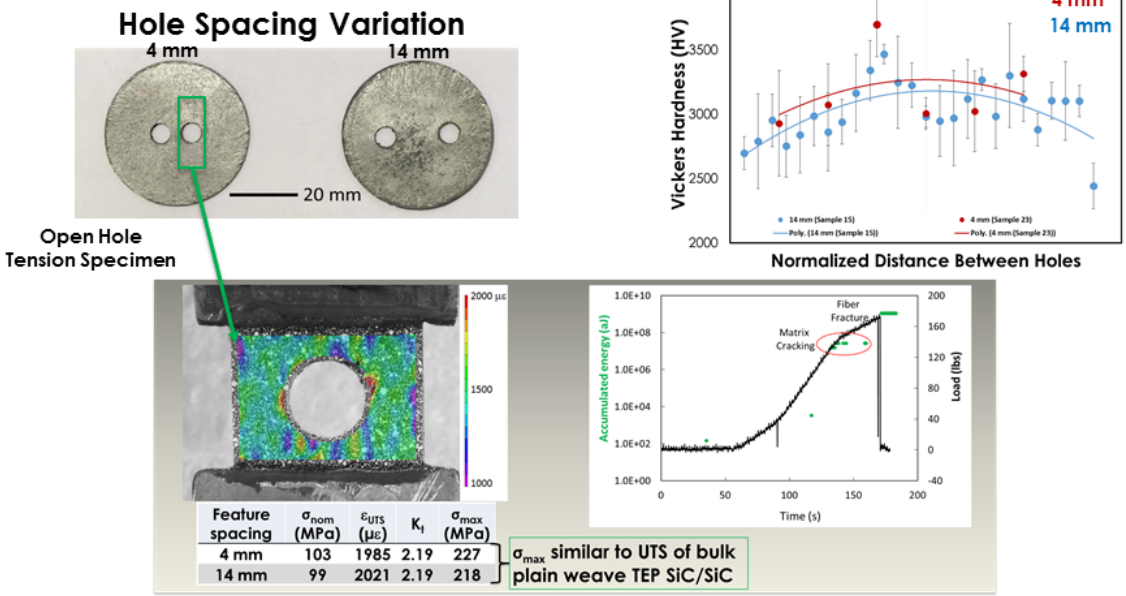

Feature spacing	σ_{nom} (MPa)	ε_{UTS} (με)	K_t	σ_{max} (MPa)
4 mm	103	1985	2.19	227
14 mm	99	2021	2.19	218

- **Open Hole Tension coupled to DIC shows retention of composite behavior and uniform strain distribution as hole spacing decreases**

1701-0060/7 GENERAL ATOMICS

Task 1 Work Established Minimum Hole Spacing in SiC-SiC

- **Planar composite structures with thru-holes have been fabricated using TEP process**
- **Microstructural anomalies arise very close to features**
  - Heat transfer modeling shows thermal gradients are responsible
- **Hole spacing as small as 4mm does not impact strength, hardness, strain**
  - Confirmed independently by open hole tension and microhardness tests
- **Smaller feature spacing has implications on core loading efficiency**

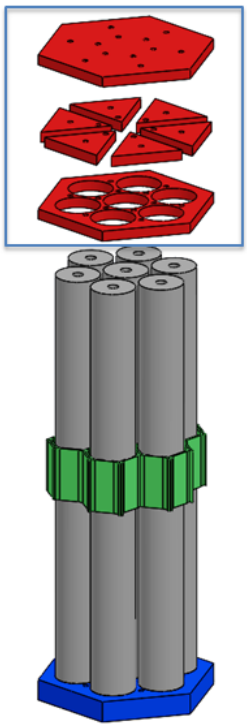

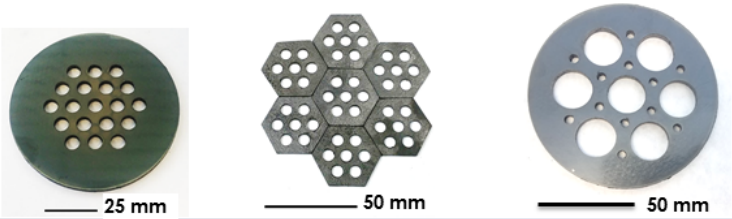

1701-0060/8

GENERAL ATOMICS

Task 2: Non-Planar Features Enable Additional Complexity

- **Basal fuel rod support structure combines curved blind hole features with thru-hole features**
  - Curved blind holes align and support individual fuel rods
  - Thru-holes permit coolant flow through core
- **Composite density, hardness and microstructure unaffected in regions beneath fuel rod reservoirs**
- **Thickness variation less than 1.5% across all reservoirs in each part**

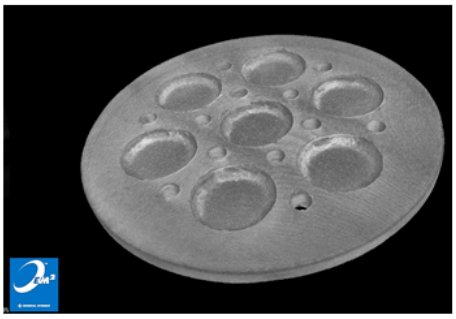

XCT volume

2D XCT slice

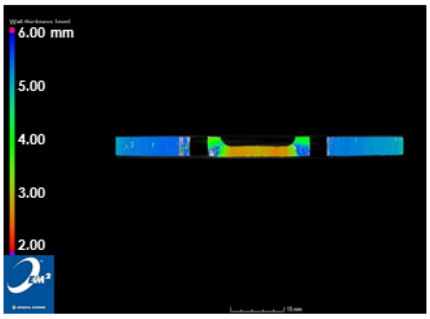

XCT-based thickness analysis

1701-0060/9 GENERAL ATOMICS

Task 2: Hexagonal Strips of SiC-SiC Were Fabricated as a Base Unit for Hexagonal Spacer Grid Structure

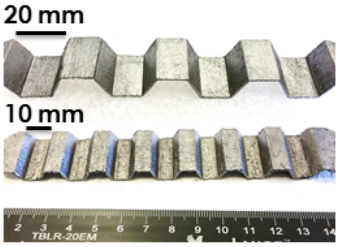

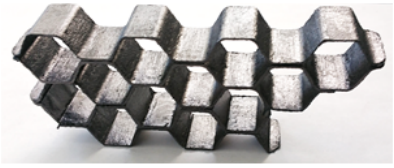

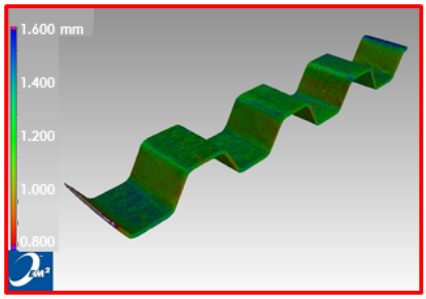

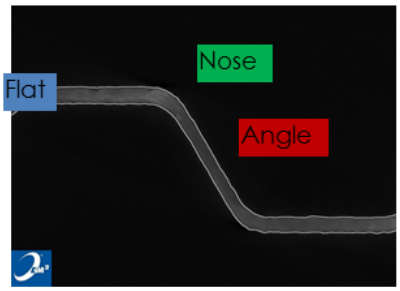

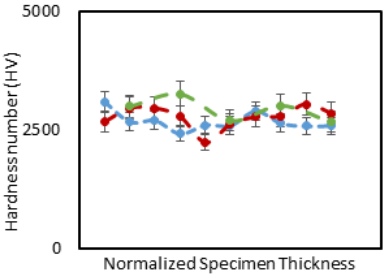

- Radius of curvature was varied (0,1,3 mm) to eliminate consolidation defects
- 3 mm radius of curvature does not impact densification or hardness

1701-0060/10 GENERAL ATOMICS

Task 2: Instrumented Drop Test and Post-impact Analysis Show Impact Resistance and Strength Retention of SiC-SiC

- Impact conditions taken from LWR industry practice for Zircaloly spacer grid *
- >90% strength retention after 2 cm, 3 kg, 0.5 m/s impact (industry std)

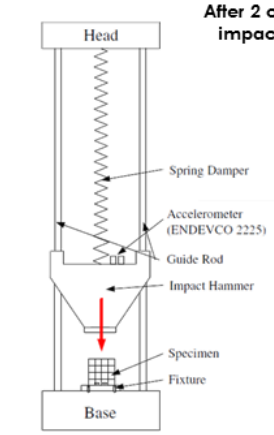

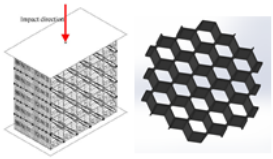

Spacer grid lateral impact*

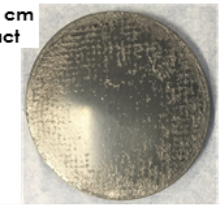

After 2 cm impact

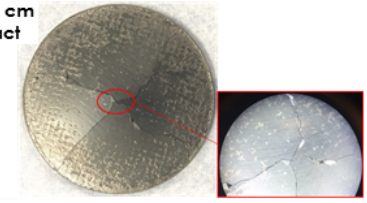

After 4 cm impact

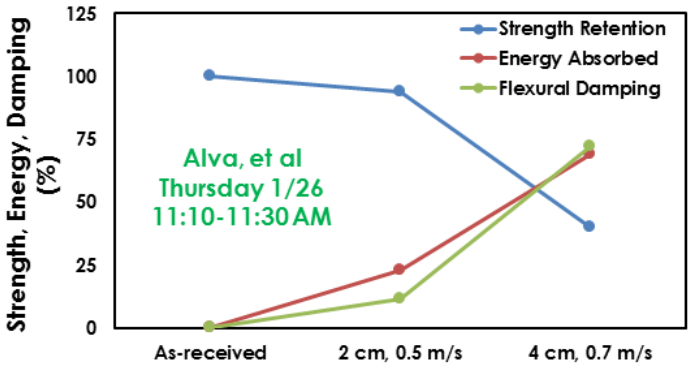

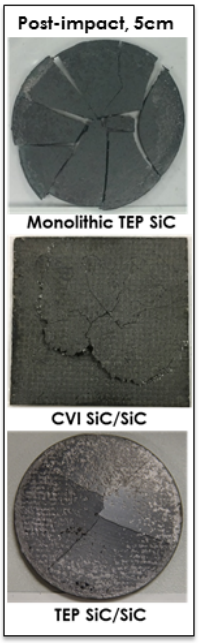

1701-0060/11

*Test configuration details taken from - Zhao et al, "LS-DYNA Applications in Simulating Impact test of nuclear fuel spacer grids and drop tests of fuel shipping packages," 12th Int'l LS-DYNA users conf.

GENERAL ATOMICS

Task 2 Work Produced Non-Planar Fuel Support Structures

- **Techniques to produce non-planar structures were established**
  - Basal fuel rod support structures with blind and thru-holes
  - Hexagonal arrays for spacer grid structures were demonstrated
- **Blind hole features and small radius of curvature do not induce local property variation**

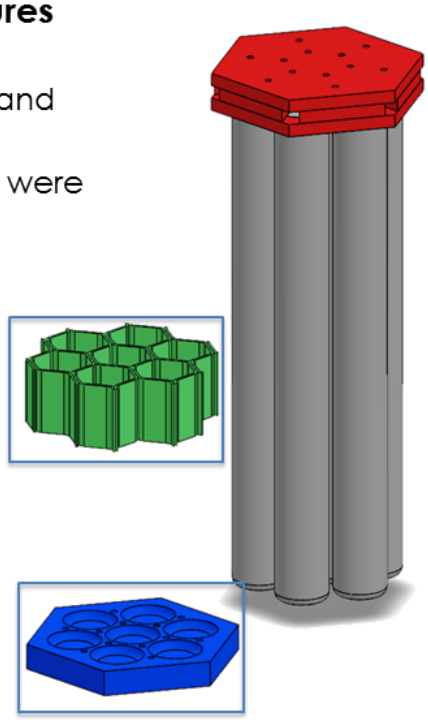

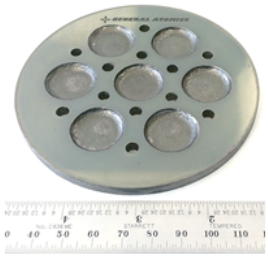

1701-0060/12

GENERAL ATOMICS

Task 3: Modular Fabrication – Joining of Planar Structures to Attain Greater Part Complexity

- **Process conditions tailored to reduce temperature and pressure**
  - Existing TEP joint technology uses high temp and pressure
- **Excellent strength and permeability performance were attained when $T_{process}$= 1600°C**

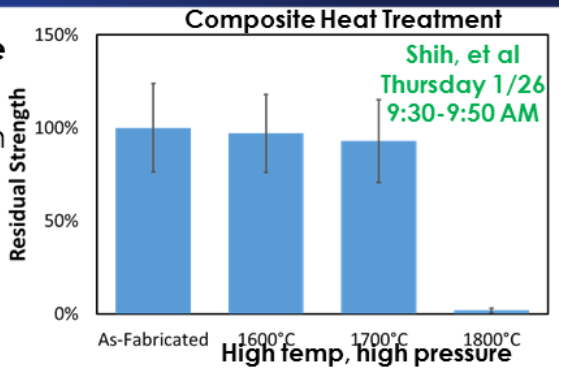

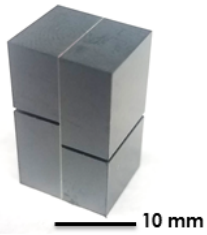

Double Notch Shear Joint Specimen

Processing	DNS Shear Strength	Helium Leak Rate
-	MPa	atm-cc/sec
High Temp, High Pressure	114 ± 12	2.1 E -10
Low Temp, Low Pressure	79 ± 19	3.4 E -10
Low Temp, No Pressure	6 ± 3	>1.0 E -04

High temp, high pressure

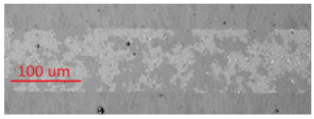

Low temp, low pressure

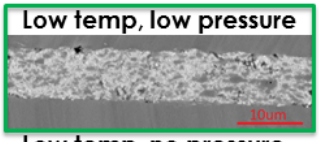

Low temp, no pressure

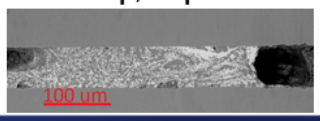

1701-0060/13

GENERAL ATOMICS

Task 3: Joint Processing and Thickness Have Been Tailored to Improve Joint Strength, Permeability and Reproducibility

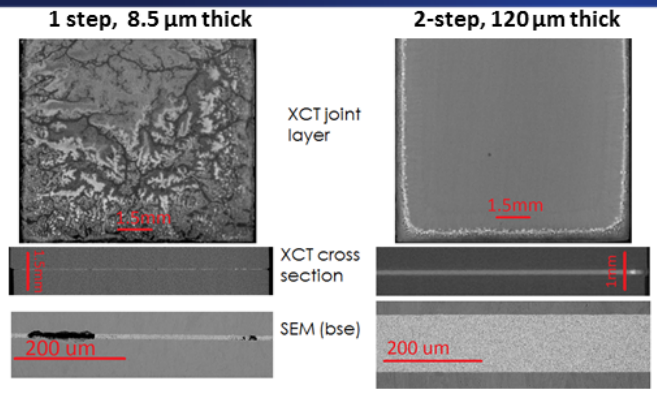

XCT of joint layer with one-step and two-step sintering profiles

- **Low temperature binder burnout reduces formation of voids**
  - Enhances permeability performance
  - Joint uniformity
- **Reduction in joint thickness minimizes CTE effects**
  - Reduces crack formation
  - Enhances strength

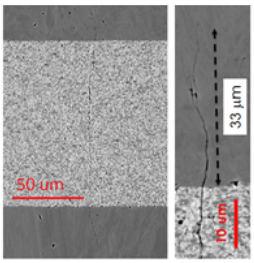

t_{joint} = 120 µm

τ = 16 MPa

Q_{leak} = 9.6 E -6 atm-cc/sec

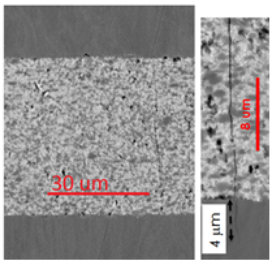

t_{joint} = 45 µm

τ = 90 MPa

Q_{leak} = 7.5 E -7 atm-cc/sec

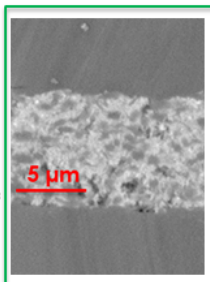

t_{joint} = 10 µm

τ = 102 MPa

Q_{leak} = 1.0 E -11 atm-cc/sec

Impermeable

1701-0060/14 GENERAL ATOMICS

Task 3 Work Established Joining Methodologies to Produce Complex Multi-layered Components

- TEP-based joints were tailored for reduced process temperature and pressure to maximize versatility
- High strength, hermetic joints were produced without compromising composite performance
- A multilayer vent manifold structure was produced that contains isolated fluid flow networks

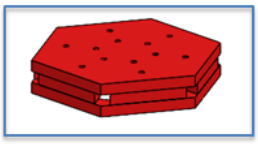

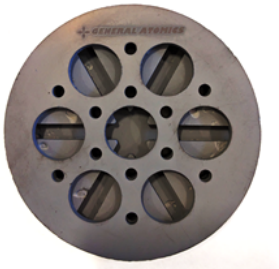

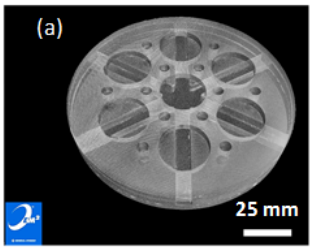

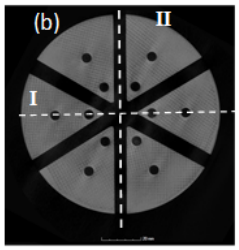

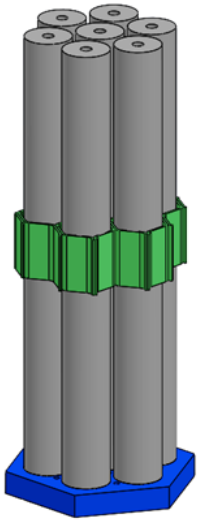

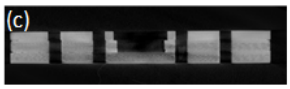

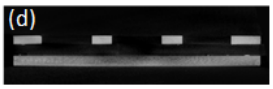

1701-0060/15

GENERAL ATOMICS

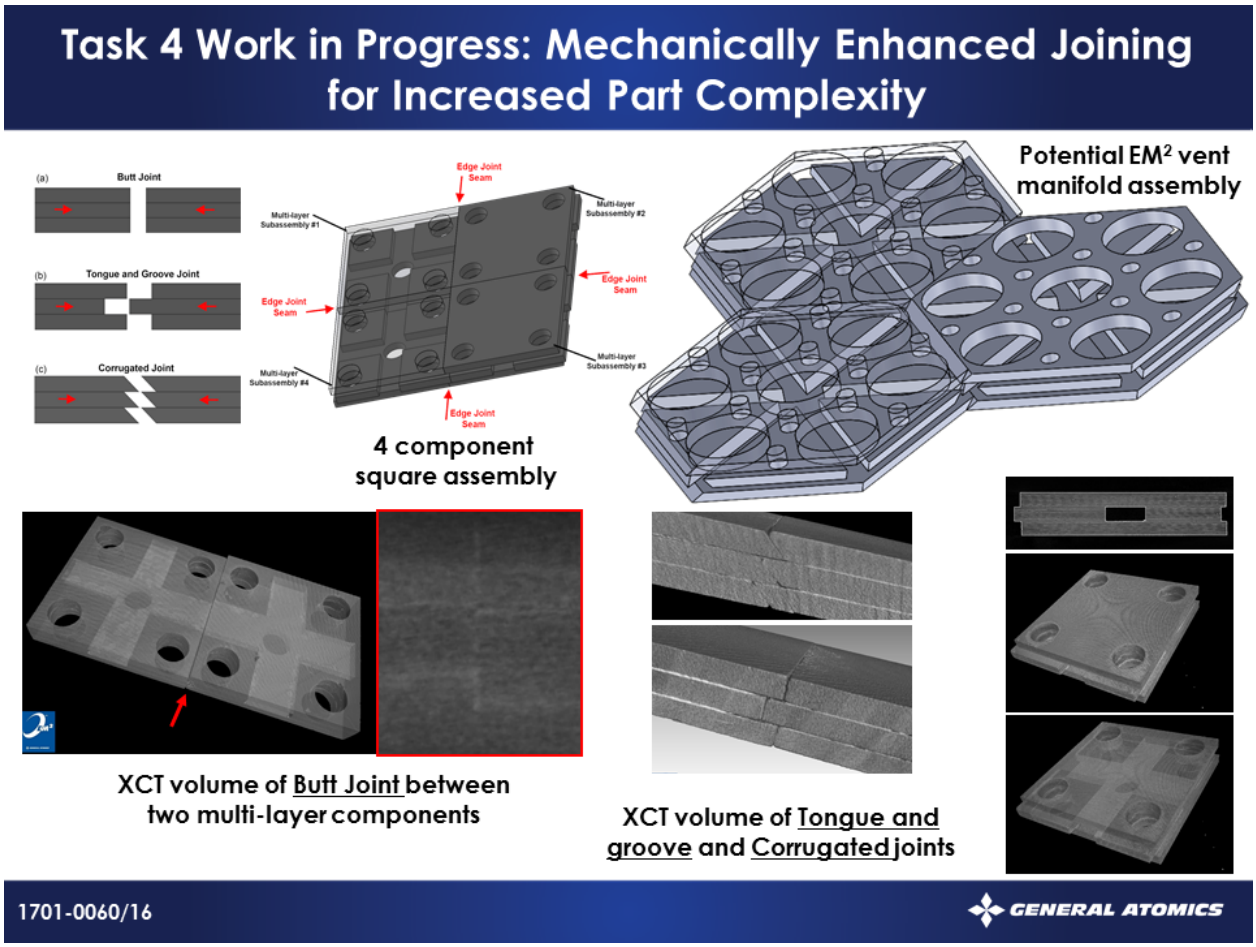
Task 4 Work in Progress: Mechanically Enhanced Joining for Increased Part Complexity
(a) Butt Joint
(b) Tongue and Groove Joint
(c) Corrugated Joint
Edge Joint Seam
Multi-layer Subassembly #1
Multi-layer Subassembly #2
Multi-layer Subassembly #3
Multi-layer Subassembly #4
4 component square assembly
Potential EM² vent manifold assembly
XCT volume of Butt Joint between two multi-layer components
XCT volume of Tongue and groove and Corrugated joints
1701-0060/16
GENERAL ATOMICS

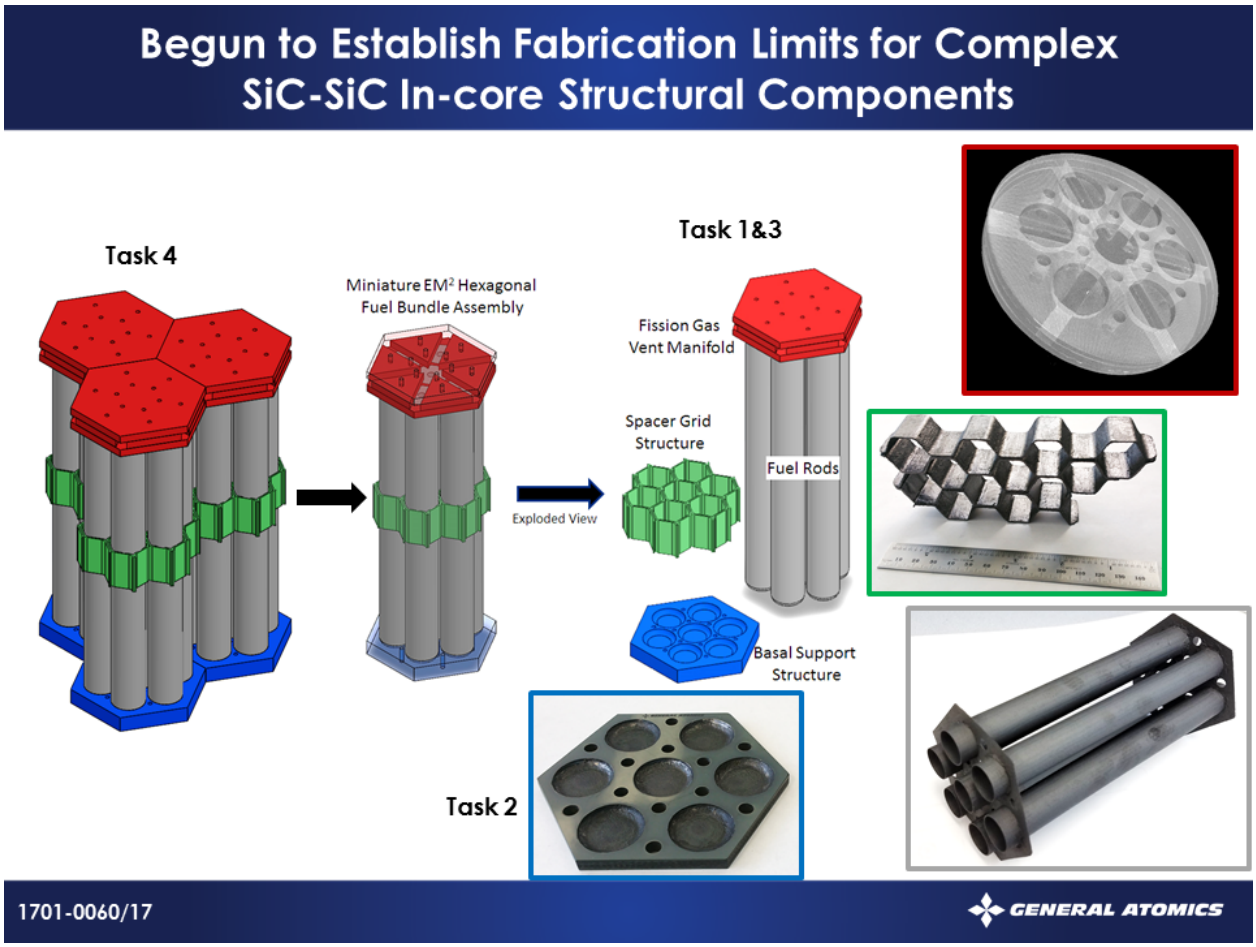
Begun to Establish Fabrication Limits for Complex SiC-SiC In-core Structural Components
Task 4
Miniature EM² Hexagonal Fuel Bundle Assembly
Exploded View
Task 1&3
Fission Gas Vent Manifold
Spacer Grid Structure
Fuel Rods
Basal Support Structure
Task 2
1701-0060/17
GENERAL ATOMICS

GA is Advancing the State of Complex SiC-SiC Composite Fabrication for Nuclear Components

- SiC-SiC has been fabricated in complex geometries targeting in-core structural components via near-net-shape TEP processing
- SiC-SiC strength, pseudoductility, and hardness are minimally affected by processing effects in complex geometries
- Lower limits of feature spacing have implications on core loading efficiency
- Tailoring of joint processing facilitates enhanced size and complexity
- Future work will include instrumented impact of joined assemblies and mechanical testing of different edge joint configurations

1701-0060/18 GENERAL ATOMICS

Appendix F – ICACC 2017 Composite Heat Treatment Effects

Strength Retention and Microstructure Evolution of SiC/SiC Composites Following Heat Treatment in Argon up to 1800°C

Chunghao Phillip Shih
Hesham Khalifa
George Jacobsen
Christian Deck

Presented Jan. 26th, 2017 In ICACC meeting

This work is supported in part by U.S.-DOE under DE-NE00008323, ART 2014 and General Atomics internal funding

SiC and SiC/SiC Are Appealing for Nuclear Applications

- **SiC and SiC/SiC composites have huge potential in advanced nuclear systems.**
  - ATF cladding
  - Next generation nuclear reactors (e.g. GA EM^2 concept)
  - Fusion reactors
- **High temperature strength retention needs to be understood**
  - Accident conditions
  - For design purposes
  - For joining purposes

GA SiC/SiC ATF cladding

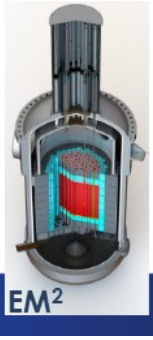

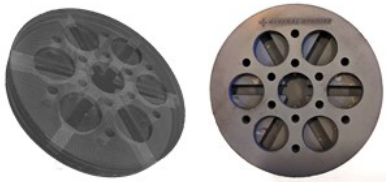

2 GENERAL ATOMICS

What Happens to SiC/SiC at High Temp?

- **What happens to SiC/SiC composites after high temperature heat treatment in argon?**

3 GENERAL ATOMICS

Two Different Nuclear Grade Composites Were Evaluated

Material	CVI SiC/SiC	TEP SiC/SiC
Fiber/Fabric	Tyranno SA3 / 2D P/W	Tyranno SA3 / 2D P/W
Interphase	PyC	PyC
Matrix	**High purity CVI β-SiC**	**1800°C hot pressed TEP SiC**
V_{fiber}	33%	33%

- **Heat treatment condition (all in argon atmosphere)**
  - (1) 1600°C, 1 hour
  - (2) 1700°C, 1 hour
  - (3) 1800°C, 1 hour
- **Characterization:**
  - Room temperature 4 point bend test
  - Microstructure by SEM
  - Weight change

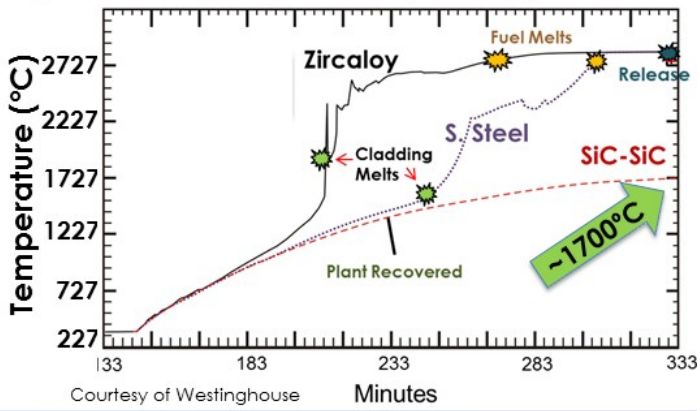

Courtesy of Westinghouse

CVI Flexural Strength Shows 72% Retention After 1700°C

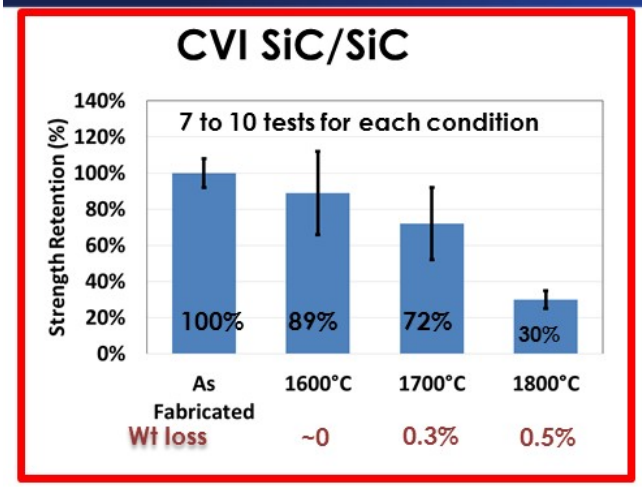

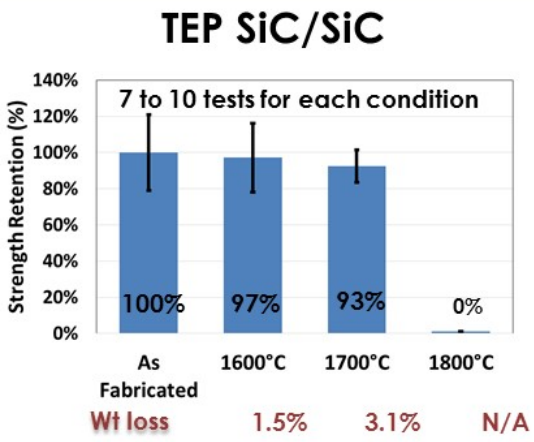

- **Minor strength degradation at 1600°C**
- **Strength retention of 72% at 1700°C**
- **Large strength degradation at 1800°C**

Stress Displacement Curves of Heat Treated CVI SiC/SiC Showed Change in Fracture Strain and Slope

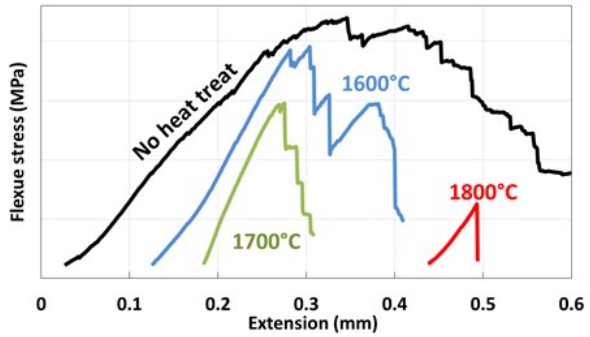

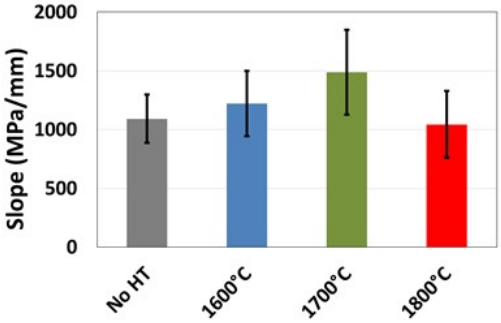

- Decrease in strength
- Decrease in fracture extension
- Brittle behavior after 1800°C

- Slope increase at 1600 & 1700°C
- Bonding between F/M interphase likely increased following heat treatment

CVI SiC/SiC Surface SEM Showed α-SiC Formation at 1700°C

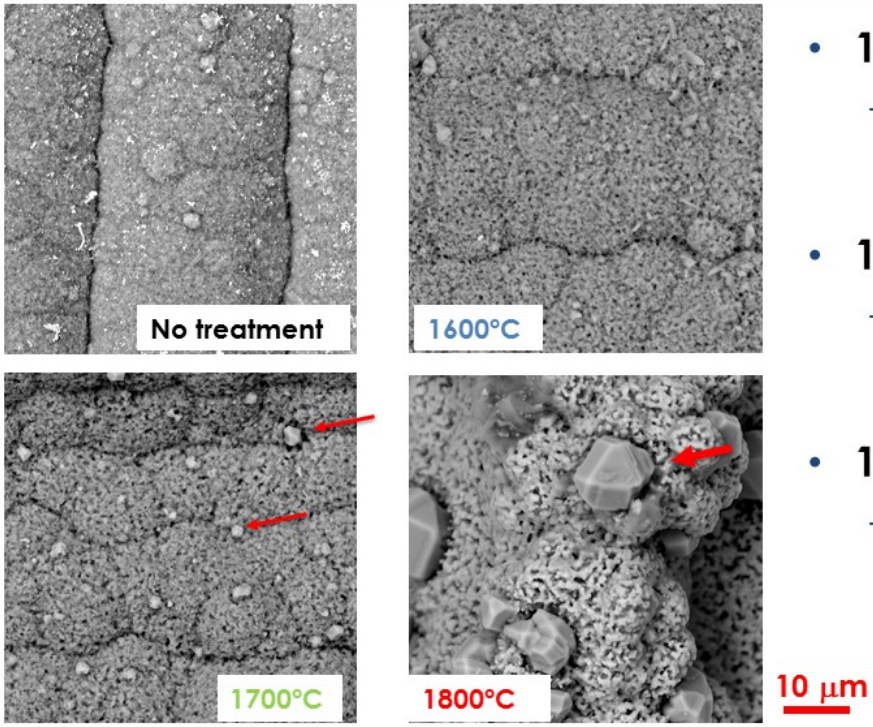

- **1600°C**
  - Mild surface morphology change
- **1700°C**
  - Nucleation and growth of α-SiC
- **1800°C**
  - Coarsening of α-SiC on matrix surface

CVI SiC/SiC Fracture Surface SEM Showed Morphology Change Is a Surface Phenomena

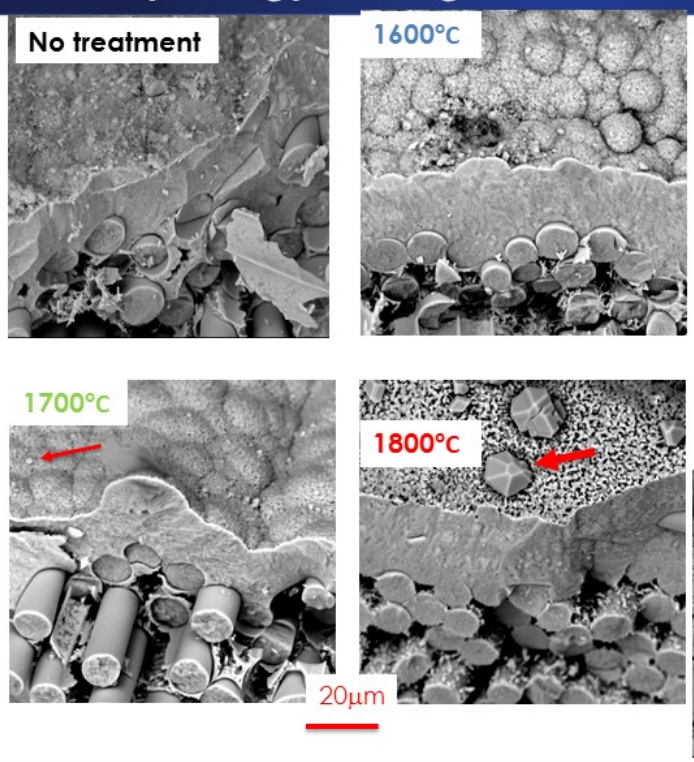

- Morphology change appears to be a surface phenomena
- This β to α transformation was reported for CVI C/SiC at 1900°C CARBON 54 (2013) 42–47

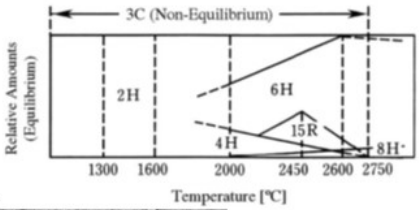

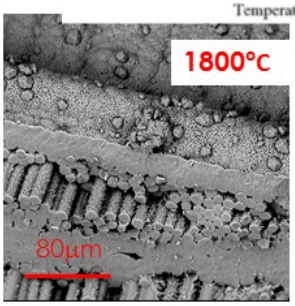

8 Journal of Nuclear Materials 371 (2007) 329–377 GENERAL ATOMICS

CVI SiC/SiC Fiber SEM Showed Evidence of Change at 1700°C

No HT

1700°C

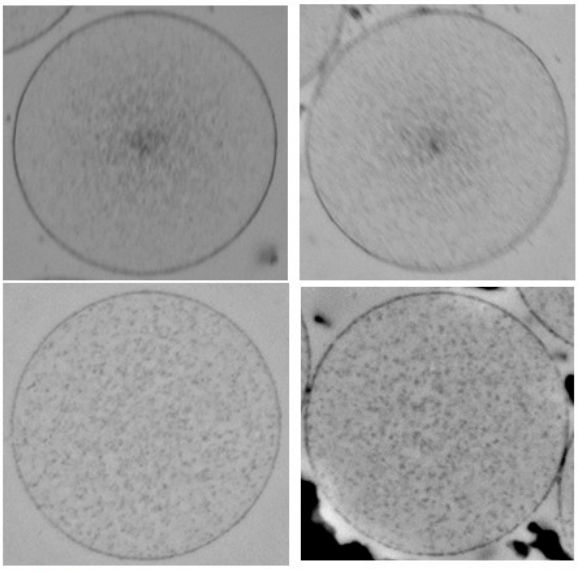

5μm

- Results agree with fracture strain well

1600°C

- No signs of fiber damage at 1600°C

1800°C

- Signs of fiber evolution (change in microstructure) at 1700°C
- Fiber evolution intensified at 1800°C

10 GENERAL ATOMICS

CVI SiC/SiC Heat Treatment Literature Suggests Material Performance Is Process Sensitive

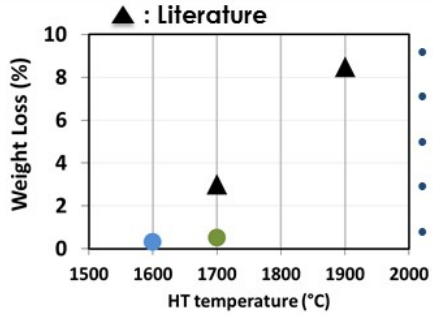

- CVI SiC/SiC (UD)
- Unknown interphase
- Hi-Nicalon Type S fiber
- Heat treat in vacuum
- Observable weight loss

Journal of Nuclear Materials 258-263 (1998) 1540-1545

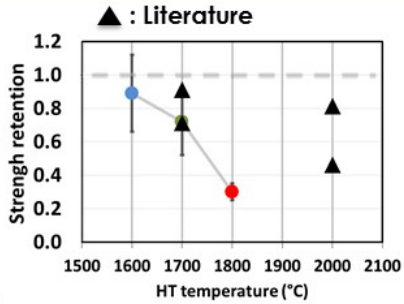

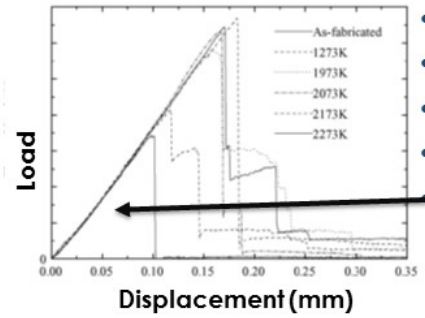

- CVI SiC/SiC (2D P/W)
- 20nm PyC interphase
- Tyranno SA fiber
- Heat treat in vacuum
- No change in modulus up to 2000°C

Ceramics International 33 (2007) 141–146

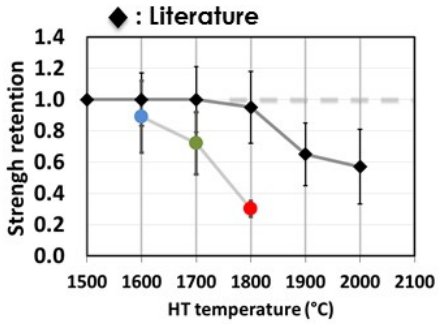

- **Material performance is process sensitive**

11 GENERAL ATOMICS

TEP Flexural Strength Showed 93% Retention After 1700°C

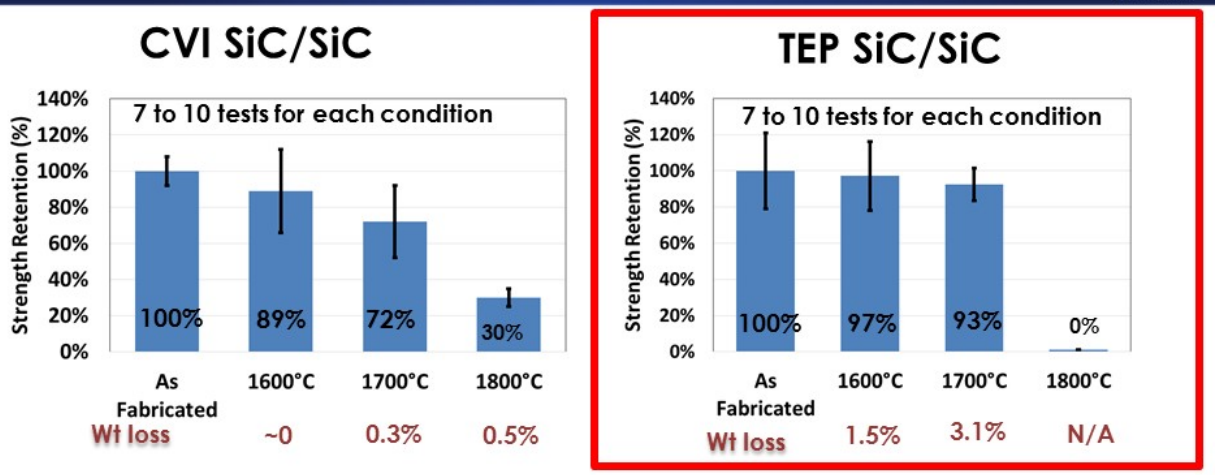

- No strength degradation, some weight loss at 1600°C
- Strength retention of 93% at 1700°C with more weight loss
- Complete degradation at 1800°C (processing temperature)

Stress Displacement Curves of Heat Treated TEP SiC/SiC Showed Change in Fracture Strain and Slope

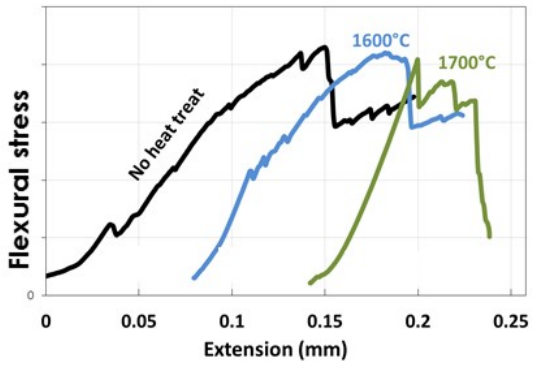

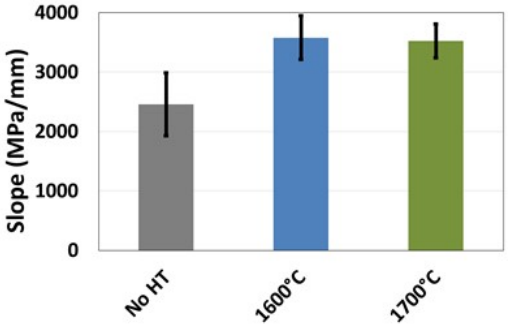

- Minor/No decrease in strength up to 1700°C
- Minor decrease in fracture extension

- Increase in slope from virgin to 1600°C samples
- Same slope for 1600°C and 1700°C samples
- Bonding between F/M interphase likely increased following heat treatment at 1600°C and 1700°C

TEP SiC/SiC Surface SEM Showed Grain Growth at 1600°C

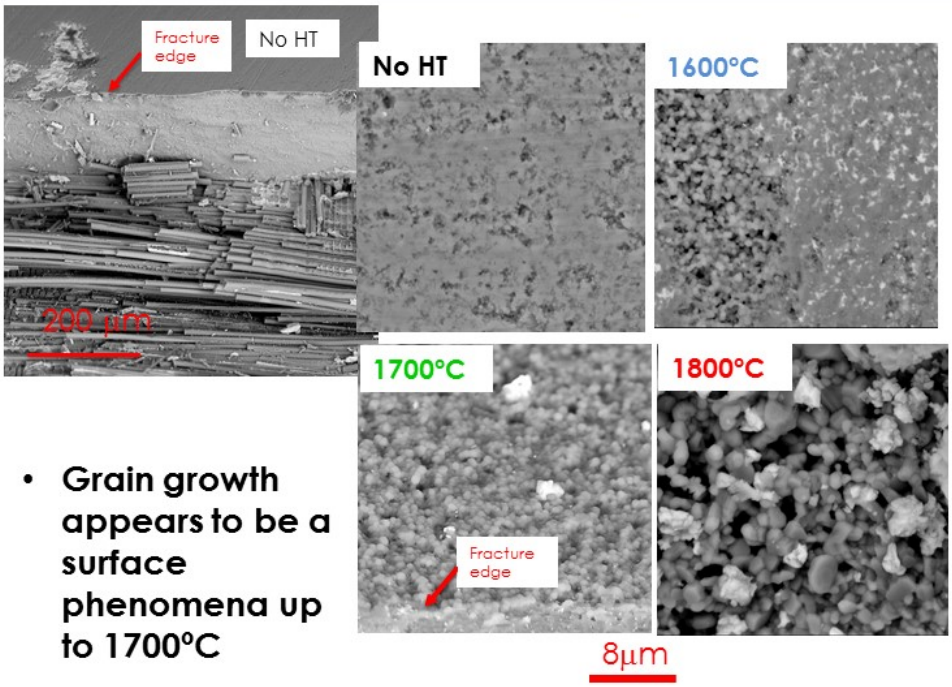

- Grain growth for 1600 and 1700°C HT samples
- Severe grain growth for 1800°C sample
- Grain growth appears to be a surface phenomena up to 1700°C

TEP SiC/SiC Fiber SEM: Minor Structure Change at 1700°C

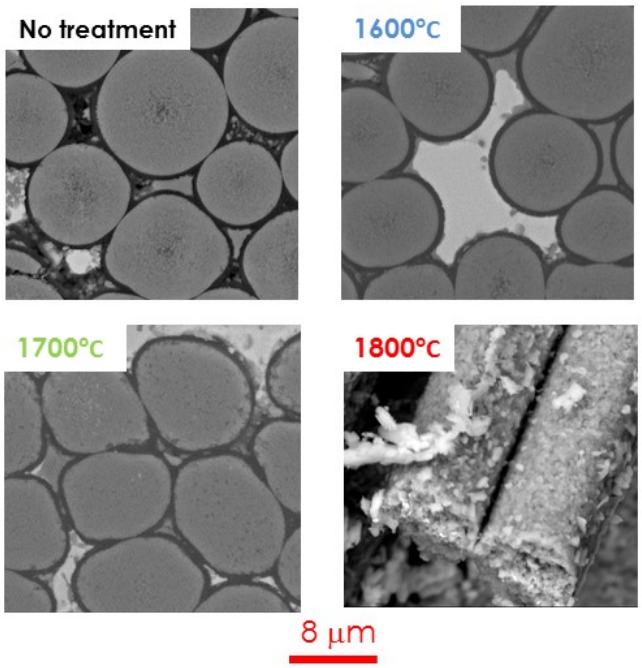

- Fiber appears intact at 1600°C
- Signs of fiber microstructure change by SEM at 1700°C
- Intra-tow oxide agglomerate and PyC interphase appear to be stable up to 1700°C
- Fiber damage, grain growth at 1800°C

TEP SiC/SiC Polished X-section SEM Showed Missing Oxide Band

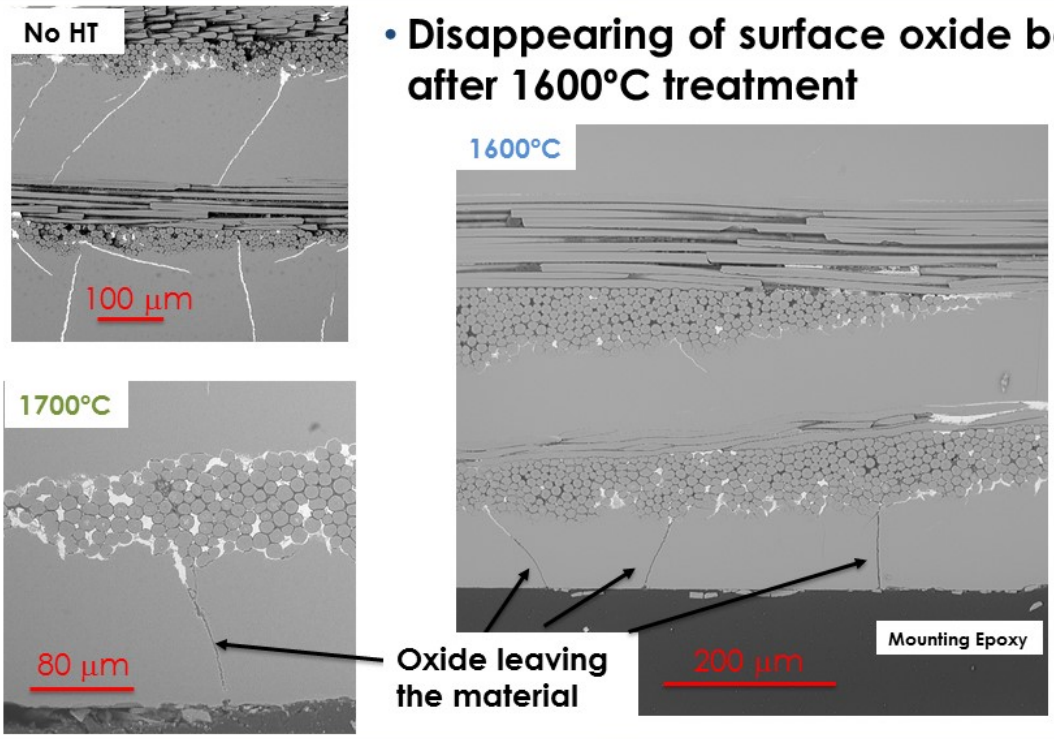

- Disappearing of surface oxide band after 1600°C treatment

Conclusion: 70%+ Strength Retention After 1700°C

HT temp	CVI SiC/SiC	TEP SiC/SiC
1600°C	High strength retention, fracture strain decrease	High strength retention, oxide band disappearing through surface
1700°C	Nucleation and growth of α-SiC on surface, minor fiber damage	Minor fiber damage
1800°C	Matrix damage and fiber damage.	Sample destroyed. Fiber and matrix grain growth

- **Both TEP and CVI SiC/SiC maintained over 70% strength following 1700°C 1 hour heat treatment in argon (severe accident conditions)**
- **Joining temperature at or below 1600°C desired for substrate strength retention**

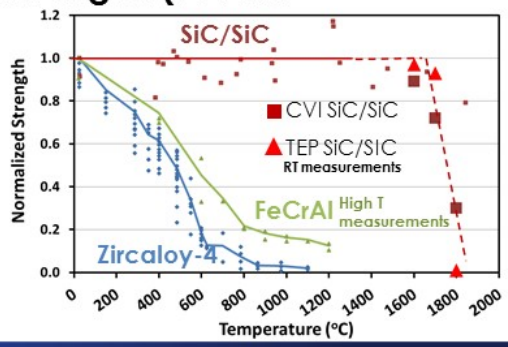

18 Gulden, J. Amer. Ceram. Soc. (1969)
Geelhood, et al., PNNL Report-17700 (2008) K.A. Terrani et al. / Journal of Nuclear Materials 448 (2014) 420–435

GENERAL ATOMICS

Appendix G – ICACC 2017 Impact Testing

Damage tolerance of SiC_f-SiC_m composite plates under low velocity impact

D. McCleeary[1]

X. Huang[1]

H. Khalifa[2]

H. Zhao[1]

L. Alva[1]

J. Clifford[1]

P. Majumdar[1]

[(1)]University of South Carolina,

[(2)]General Atomics, Nuclear Technologies and Materials Division

huangxin@mailbox.sc.edu

Mechanical Engineering Department
Address: 541 Main St., Columbia, SC 29208
Phone: 803-777-1329; 803-777-4185

This work supported in part by U.S.-DOE under DE-NE00008323, ART 2014

Objective

- To study the damage tolerance of SiC_f-SiC_m composite plates to low-velocity impact. The composite plates are fabricated by TEP method. Monolithic SiC plates were tested under similar conditions and compared to the composite samples.
- To use the impulse excitation method to quantify the evolution of damage in the composite samples after repeated impact. Frequency and damping of the samples are calculated after each impact.
- Use a custom-made burst test to quantify the residual strength of the SiC composite plates that survived impact. During the burst test the sample is loaded under an equal biaxial state of stresses.

Samples (manufactured by GA)

Samples were fabricated by hot pressing (TEP) of SiC, Al_2O_3, Y_2O_3 and SiC fibers at temperatures of about 1800 C.

SiC Composite

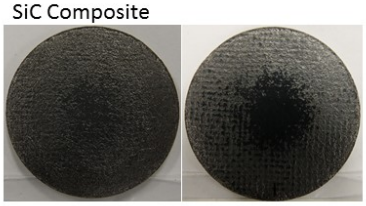

Thickness: 3 mm
Diam.: 50.8 mm

Monolithic SiC

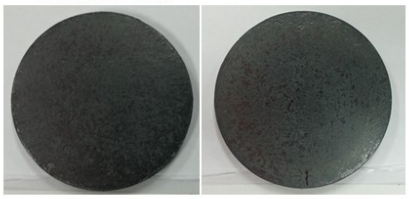

Cross section

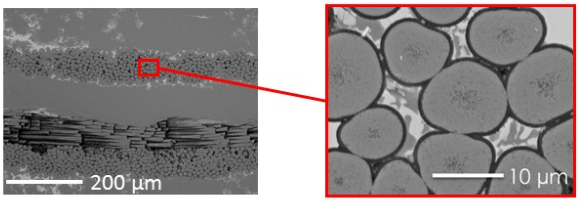

Impact Scenarios

1. Drop of a fuel assembly
   1. During loading/unloading
2. Lateral impact on the fuel assembly: between assemblies and/or assembly and core wall
   1. Earthquake (lateral seismic acceleration)
   2. LOCA (lateral blowdown forces)
3. Impact vibration between fuel rod (cladding) and springs/dimples of the space grid
   1. Flow-induced vibration in the presence of a gap
4. RIA: impact of the fuel pellet against the cladding

DYNAMIC IMPACT ANALYSIS OF THE GRID STRUCTURE USING MULTI-POINT COSTRAING (MPC) EQUATION UNDER LATERAL IMPACT LOAD
Yoon et al., Computers and Structures 82 (2004) 2221-2228

Impact Evaluation

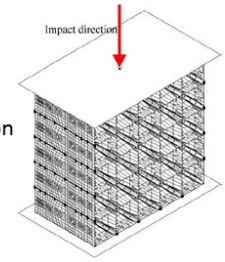

Fig. 5. Finite element model of 5×5 cell Doublet grid for impact analysis.

Instron Dynatup 8200 HE Drop Tower

Energy Capacity, J (ft-lbs)	390 (290)
Max. Impact Velocity, m/s (ft/s)	7.5 (24.5)
Max. Rail Cart Weight, kg (lbs)	16 (35)
Max. Drop Height, m (in.)	2.3 (91)

Instrumentation:
- Oscilloscope: $2x10^6$ samples/s
- Velocity Sensor
- Weight: 2.76 kg

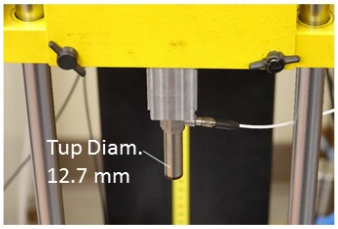

Impulse Excitation

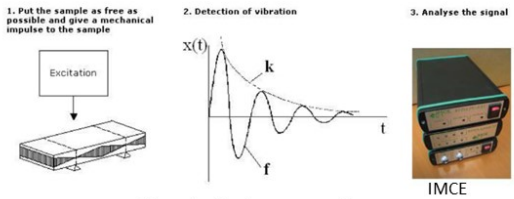

RFDA Working Principle (IMCE Manual)

IMCE Modules

- When an object has a force applied to it, the energy is dissipated by the material as a vibration.
- The vibration has a frequency spectrum according to its resonant frequencies that depend on: elastic properties, geometry, density.
- This test can yield information about the properties of a material, and how those properties change after destructive testing.

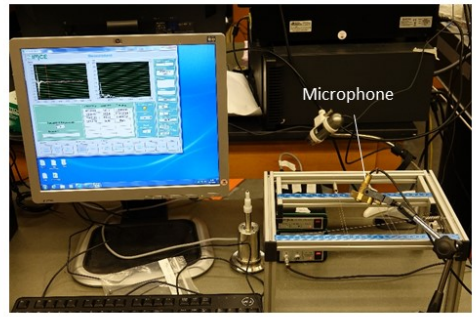

$$x(t) = Ae^{-kt}sin(wt + \emptyset)$$

Frequency $f = \omega/2\pi$

Damping $Q^{-1} = \frac{k}{\pi f}$

(IMCE Manual)

Burst Test of Flat Bladder Test

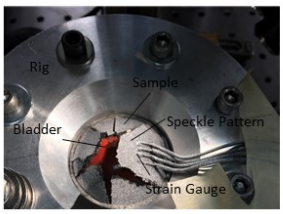

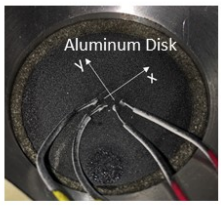

Maximum stress at the center of the disk:

$$\sigma_m = \frac{3(3+\nu)pr^2}{8t^2}$$

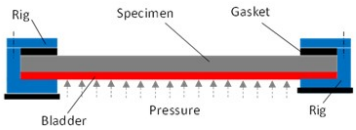

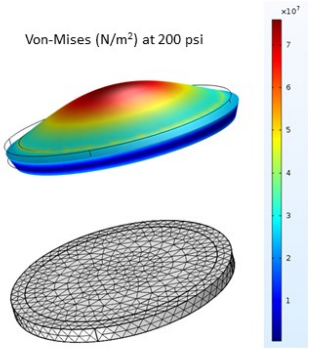

An aluminum disk was used to calibrate the burst rig.

Pressure (psi)	Measured strain ε_{xx} (με)	Measured strain ε_{yy} (με)	Model Strains $\varepsilon_{xx} = \varepsilon_{yy}$ (με)	Model Stress (Mpa)	Analytical stress (Mpa)	Strain error %	Stress error %
45	187.57	184.64	176	18.1	18.94	6.17	4.44
100	459.55	471.37	391	40.2	42.09	14.92	4.49
200	901.57	941.37	782	80.5	84.19	13.26	4.38

Increased Impact - DWIT

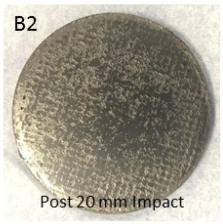

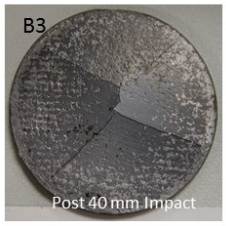

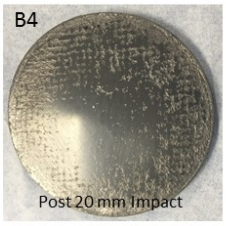

Sample	DWIT Height mm	Burst Press. MPa	Absorbed Energy J
B1	----	2.69	----
B2	20	2.59	0.072
B3	40	0.83	0.586
B4	20 & 40	0.81	0.59 / 0.54

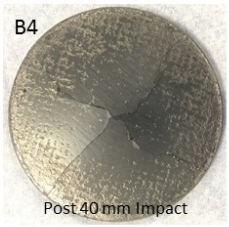

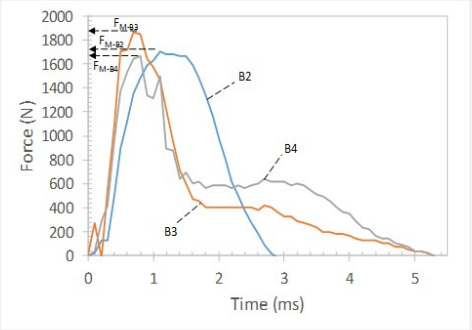

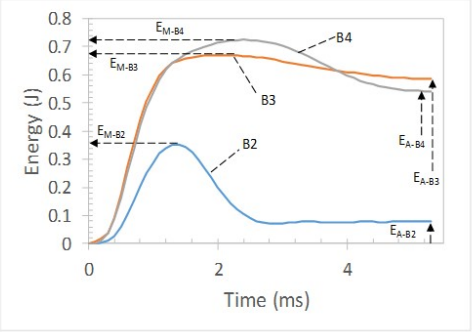

Sample B5 (repeated 20-mm DWIT and IE)

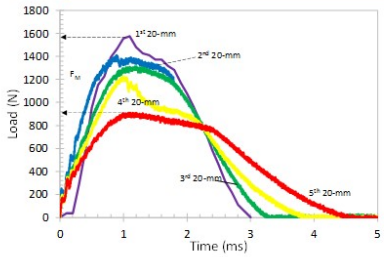

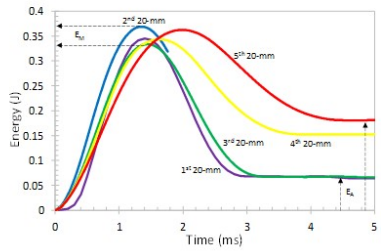

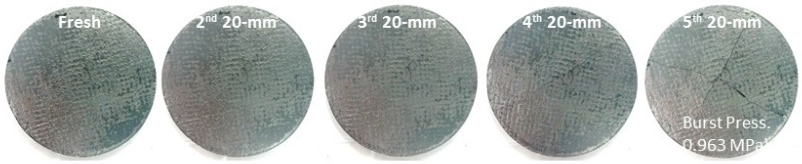

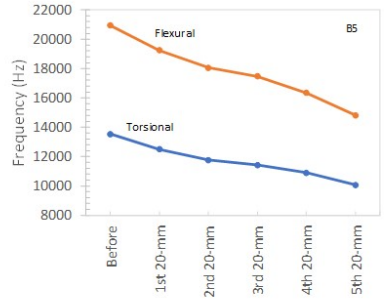

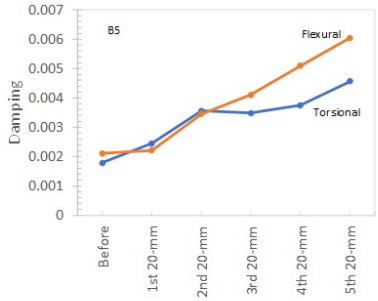

Sample B6 – 100-mm DWIT and IE

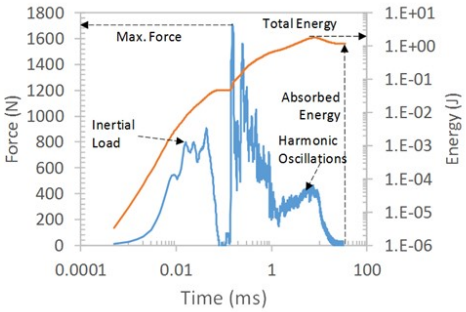

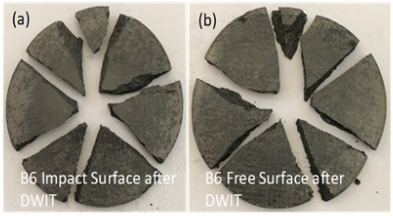

Status	Torsional Frequency (Hz)	Damping (Torsion)	Flexural Frequency (Hz)	Damping (Flexural)
Before Impact	13821.75	0.001277	21238.16	0.001661
After Impact	NA	NA	NA	NA

Monolithic Samples

40-mm DWIT

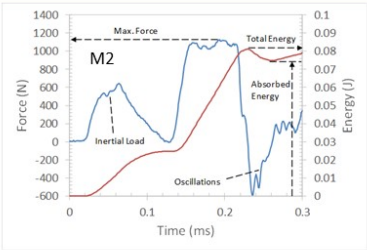

100-mm DWIT

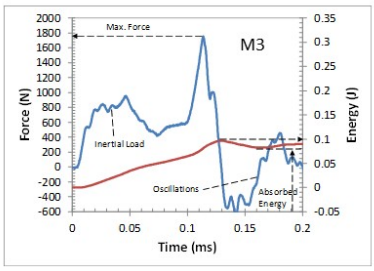

Sample	Burst Press. fresh (Mpa)	40-mm DWIT	100-mm DWIT
Composite (2 mm)	1.39	Survived	-----
Composite (3 mm)	2.69	Survived	Do not survived, E_A = 1.154 J
Monolithic (3 mm)	2.22	Do not survived	Do not survived, E_A = 0.081 J

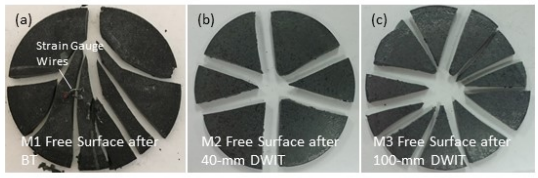

CVI Sample – 20-mm then 40-mm DWIT

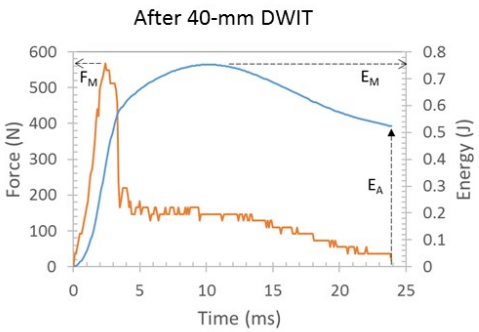

Size (mm)	50.8 x 50.8
Thickness	1.15 mm
E_A (J)	0.483

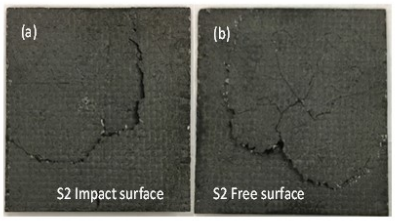

Microscopic Images (close to the center and to the free surface)

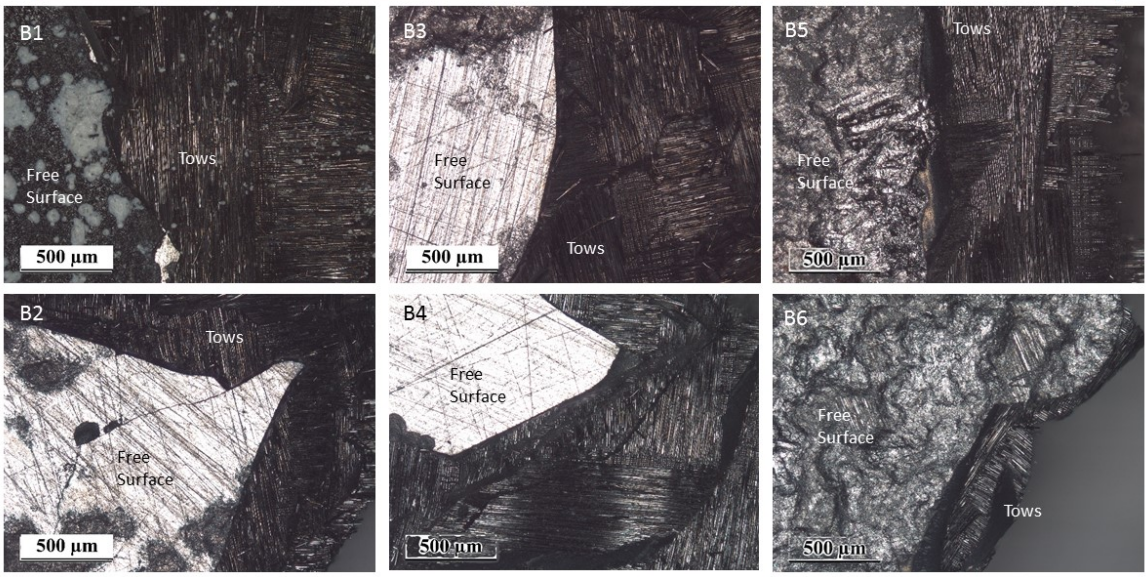

Remarks

- SiC_f-SiC_m composite plates fabricated by TEP method were tested using a low impact velocity method.
- The SiC composite plates shows an improved damage tolerance to impact than monolithic SiC plates.
- The IE method was used to find the frequency and damping of the samples before and after the tests. It was found that the frequency and the damping of the SiC_f-SiC_m composite plates decreases and increases respectively as the damage increases.
- The burst test is an effective method to quantify the remaining toughness of the samples that survive the impact test.